Strategic Space Monitoring

Surveillance Strategies for LEO Catalogue Generation using Ground-based Optical Sensors

J.T. Barens Romero

Delft University of Technology

Strategic Space Monitoring

Surveillance Strategies for LEO Catalogue Generation using Ground-based Optical Sensors

by

J.T. Barens Romero

to obtain the degree of Master of Science
at the Delft University of Technology,
to be defended publicly on December 15 at 13:00.

Student number:	5268400	
Project duration:	April 16, 2025 – November 26, 2025	
Chair:	Dr. J. G. De Teixeira da Encarnação,	TU Delft
Examiner:	Dr. P. Piron,	TU Delft
Supervisor:	Dr. S. Gehly,	TU Delft
External Supervisor:	B. Kieboom,	Airbus Defence and Space

Cover: Yang via Unsplash
Style: TU Delft Report Style, with modifications by Daan Zwaneveld

Preface

After five years at Delft University of Technology, this thesis represents the culmination of my studies. I have grown tremendously since arriving as an eager 17-year-old during COVID, ready to dive into aerospace engineering. Through TU Delft, I have lived, worked, and studied across four countries, meeting countless interesting people and making many friends along the way.

For this thesis, I had the great opportunity to work at Airbus Defence and Space in Immenstaad, Germany. This experience showed me what life is like at a major aerospace company, and I had the chance to work with many intelligent and insightful colleagues. To my supervisor at Airbus, Bart, I extend particular gratitude. Your insights into the domain of tracklet correlation were extremely valuable, and your consistent guidance kept me on track and excited about the work. To my supervisor at TU Delft, Steve, I am equally grateful. Your kind and professional attitude, and commitment to helping me improve, have been immensely helpful. Thank you both.

Beyond technical skills, these five years taught me invaluable lessons about life, resilience, and friendship. To all the friends I've made, at TU Delft and beyond, thank you for making this journey so enjoyable. You made these years special, and I will look back on them fondly forever. Aroha, gracias por todo.

Finally, to my family: thank you for your unwavering support. I left home early, but you have always been there for me. I know I can always count on having a wonderful home to return to. To Mum, Dad, Sebastian, and Sofia, thank you.

J.T. Barens Romero
Delft, November 2025

Abstract

The growing population of objects in Low Earth Orbit (LEO) presents challenges for space situational awareness and catalogue maintenance. With proliferation of small satellites and debris, maintaining accurate orbital data is essential for collision avoidance and space traffic management. This thesis evaluates ground-based optical surveillance strategies for LEO catalogue generation, comparing three fixed-pattern scanning methods (declination stripe, right ascension stripe, grid) as baseline, against a two-phase Probabilistic Admissible Region (PAR) approach that incorporates initial detection information into follow-up observation planning.

Simulations were performed using the SPOOK (Special Perturbations Orbit determination and Orbit analysis toolKit) framework developed by Airbus Defence and Space, covering 1,562 sun-synchronous LEO satellites and validated against observations made by the Airbus Robotic Telescope (ART) from September 2025. Additional validation examined Medium Earth Orbit (MEO) satellites to assess surveillance difficulty dependence on orbital regime.

For LEO targets, baseline scanning patterns achieved 0.0116% detection rates and zero redetections. The PAR pipeline achieved 23.71% redetection rate across 194 follow-up attempts, providing the multiple observation epochs required for initial orbit determination. MEO results revealed strong regime-dependence. Baseline methods achieved 49–62% MEO redetection rates compared to 0% for LEO, while PAR achieved 91.94% for MEO versus 23.71% for LEO. MEO baseline detection rates exceeded LEO rates by three orders of magnitude, reflecting differences in satellite angular motion and observation arc duration between regimes.

Parameter sensitivity analysis demonstrated PAR robustness, with performance largely insensitive to configuration choices within tested ranges. Observation duration emerged as the primary factor influencing success, while exposure time, orbital constraints, and sampling density showed minimal systematic effects. Validation against ART observations confirmed 63.6% pipeline accuracy with mean angular separation of 40.53 arcseconds, consistent with SGP4 propagation accuracy.

The results establish that surveillance strategy effectiveness depends on orbital regime. For LEO surveillance, where rapid motion and brief observation windows prevent fixed-pattern redetections, PAR-based approaches provide a viable solution for catalogue generation. For MEO surveillance, both fixed-pattern and adaptive strategies achieve high success rates, though PAR maintains superior performance.

Contents

List of Figures

List of Tables

Nomenclature

Abbreviations

Abbreviation	Definition
AR	Admissible Region
ART	Airbus Robotic Telescope
CAR	Constrained Admissible Region
CMOS	Complementary Metal-Oxide-Semiconductor
ECI	Earth-Centred Inertial
EM	Expectation-Maximisation
FoV	Field of View
GEO	Geostationary Earth Orbit
GMM	Gaussian Mixture Model
IOD	Initial Orbit Determination
J2	Second Zonal Harmonic of Earth's Gravity
LEO	Low Earth Orbit
MEO	Medium Earth Orbit
OD	Orbit Determination
PAR	Probabilistic Admissible Region
pdf	Probability Density Function
QE	Quantum Efficiency
RSO	Resident Space Object
SGP4	Simplified General Perturbations 4
SNR	Signal-to-Noise Ratio
SPOOK	Special Perturbations Orbit determination and Orbit analysis toolKit
SSA	Space Situational Awareness
T2O	Tracklet-to-Object
T2T	Tracklet-to-Tracklet
TDM	Tracking Data Message
TEME	True Equator Mean Equinox
TLE	Two-Line Element
TOD	True of Date
TSA	Too Short Arc
UKF	Unscented Kalman Filter

Symbols

Symbol	Definition	Unit
Latin Symbols		
a	Semi-major axis	[km]
A	Cross-sectional area	[m^2]
C_D	Drag coefficient	[-]
e	Eccentricity	[-]
E	Specific orbital energy	[km^2/s^2]
El	Elevation angle	[rad]
f_{overlap}	Overlap factor	[-]

Symbol	Definition	Unit
$\boldsymbol{h}$	Specific angular momentum vector	[km^2/s]
$h_\odot$	Sun altitude angle	[rad]
i	Inclination	[rad]
I_{dark}	Dark current rate	[e-/pixel/s]
$\mathcal{J}$	Optimisation objective function	[-]
K	Number of GMM components	[-]
m	Mass	[kg]
N_{samples}	Number of Monte Carlo samples	[-]
n_{pix}	Number of pixels	[-]
N_*, N_S, N_D	Source, Sky, Dark signal components	[e-]
r	Magnitude of position vector	[km]
$\boldsymbol{r}$	Position vector	[km]
r_a, r_p	Apogee, Perigee radius	[km]
R_e	Earth's equatorial radius	[km]
$\boldsymbol{R}_s$	Observer position vector	[km]
$S(t)$	Search set in state space at time t	
t_{dwell}	Dwell time	[s]
t_{exp}	Exposure time	[s]
$t_{\text{read}}, t_{\text{slew}}$	Readout time, Slew time	[s]
v_δ	Declination velocity	[rad/s]
$\boldsymbol{v}_{rel}$	Velocity relative to atmosphere	[km/s]
w_α	Right Ascension width	[rad]
$\boldsymbol{x}$	State vector (Position and Velocity)	
Greek Symbols		
α	Right Ascension	[rad]
$\mathcal{A}$	Attributable vector	
$\mathcal{C}$	Constraint set	
δ	Declination	[rad]
$\Delta\theta_{\text{moon}}$	Moon separation angle	[rad]
ϵ_E	Geocentric two-body energy	
$\mathcal{H}, S_{\mathcal{H}}$	Measurement space, Search set in measurement space	
μ	Earth's gravitational parameter	[km^3/s^2]
$\boldsymbol{\mu}_k$	Mean vector of GMM component k	
$\mathcal{N}$	Gaussian distribution	
ν	True anomaly	[rad]
ϕ	Geodetic Latitude	[rad]
Φ	Flow function in dynamics	
π_k	Mixing weight of GMM component k	[-]
Ψ	Sensor field of view	[rad]
ρ	Range	[km]
ρ_{atm}	Atmospheric density (Drag)	[kg/m^3]
$\rho_{\text{MIN}}, \rho_{\text{MAX}}$	Minimum, Maximum range constraints	[km]
σ	Standard deviation	
σ_{read}	Read noise standard deviation	[e-]
$\boldsymbol{\Sigma}_k$	Covariance matrix of GMM component k	
τ	Integration time	[s]
θ	Phase angle	[rad]
Ω	Right Ascension of Ascending Node (RAAN)	[rad]
ω	Argument of Perigee	[rad]
ω_{max}	Maximum angular rate	[rad/s]
$\mathcal{X}$	State space	
Time Derivatives		
$\dot{\alpha}$	Right Ascension rate	[rad/s]

Symbol	Definition	Unit
$\dot{\delta}$	Declination rate	[rad/s]
$\dot{\rho}$	Range rate	[km/s]

1

Introduction

The expanding population of objects in Low Earth Orbit (LEO) presents significant challenges for Space Situational Awareness (SSA), which concerns the tracking and characterisation of space objects [45]. The proliferation of small satellites, debris, and other objects (see Figure 1.1 & Figure 1.2) has made maintaining an accurate catalogue of objects in orbit increasingly critical for collision avoidance, national security, and space traffic management. However, the strategies used for accurate surveillance of the night sky remain an active field of research, with room for innovation and improvement.

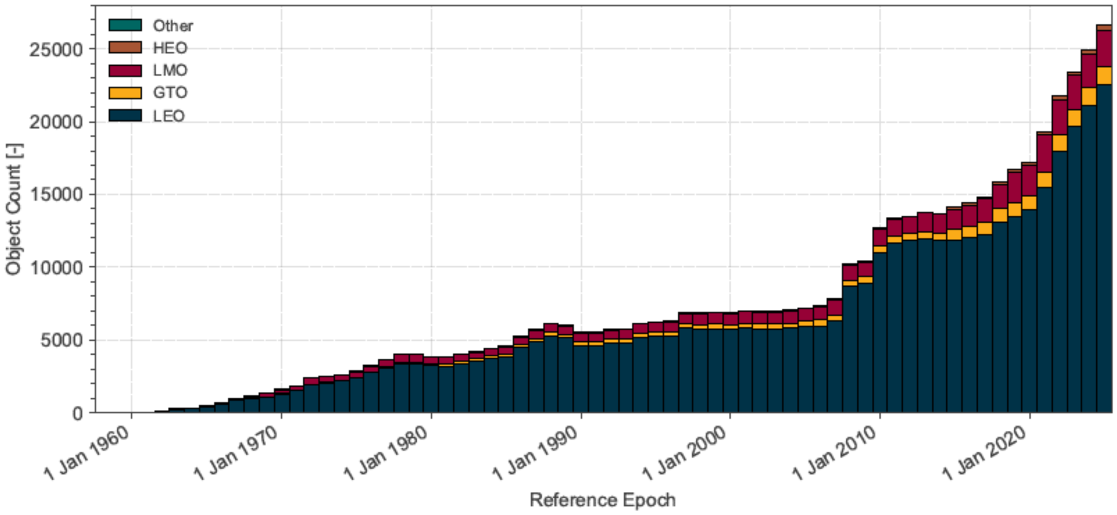

Figure 1.1: Evolution of absolute number of objects penetrating LEO. Image from: [35].

The task of efficiently detecting LEO objects using optical sensors faces unique complications. These objects have brief visibility windows from any single observation point, typically lasting only minutes per pass. Observations are further constrained by local weather conditions, atmospheric visibility, and the limitations of the tracking sensors' field of view. The high orbital velocities of LEO objects, combined with various perturbation forces, lead to rapid uncertainty growth in their predicted positions when observations are sparse [9].

A fundamental challenge in LEO object tracking is that these measurements, collected during short passes of often just a few minutes or less, cover only a small portion of the complete orbit. This limited observation window makes determining an accurate orbit from a single pass difficult, creating what is known as the Too Short Arc (TSA) problem [25].

Passive optical sensors play a crucial role in catalogue maintenance and generation due to their

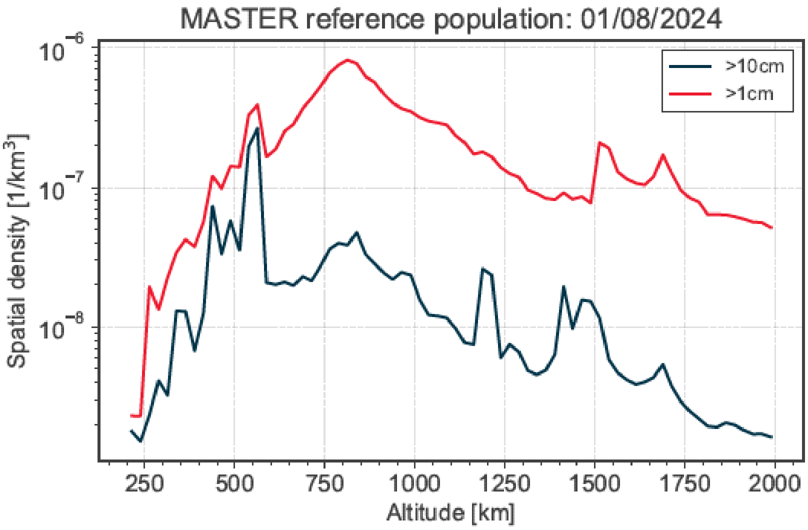

Figure 1.2: Density profiles in LEO for different space object size ranges. Image from: [35].

widespread use and relatively low operational costs compared to radar systems [9]. However, in the case of LEO, these sensors yield angular measurements only (in the form of TSAs, i.e. tracklets), which presents challenges in determining an object's complete orbital state. Because tracklets represent only a small section of the object's orbital path, they provide insufficient information for robust Initial Orbit Determination (IOD). This limitation requires techniques for generating and correlating multiple tracklets separated in time, such that a representative sample of the complete orbit is obtained.

This research specifically focuses on comparing different surveillance strategies for LEO catalogue generation using ground-based optical telescopes. The investigation encompasses both fixed-pattern surveillance strategies and adaptive approaches that leverage initial detection information to optimise subsequent observations. By implementing various strategies through simulation software and analysing their performance metrics, this study aims to identify optimal approaches for maximising catalogue generation efficiency under realistic operational constraints.

Key to this investigation is the development of a surveillance strategy for tracklet correlation, for which Admissible Region (AR) techniques play key roles. AR methods address the challenge of extracting maximum information from sparse optical observations by constraining the possible state space of detected objects by setting bounds on the range and range-rates, values that are missing from a simple tracklet. The Constrained Admissible Region (CAR) extends this approach by setting additional constraints on orbital parameters and maximum energy. Building upon the CAR, the Probabilistic Admissible Region (PAR) technique introduces uncertainty in both the observations and the orbital parameters. The goal of PAR-based algorithms is to develop probability distributions of state uncertainties using knowledge about measurement process statistics and orbital parameter distributions. These probability distributions can then be propagated forward in time to predict where follow-up observations are most likely to yield successful detections, thereby enhancing the efficiency of the overall surveillance strategy.

By leveraging these AR techniques, it becomes possible to generate orbit hypotheses from short arc optical observations, addressing the challenge of insufficient information. These hypotheses are then utilised in subsequent steps to design an effective multi-step surveillance strategy [18, 14] that maximises the probability of redetection and ultimately leads to more complete and accurate orbit determinations.

This work aims to implement, test, and validate these strategies for creating follow-up observation plans. By successfully re-observing LEO objects after initial detections, this thesis will demonstrate the effectiveness of AR methods for catalogue generation. The proposed strategies will be evaluated both through simulation and experimentally using the Airbus Robotic Telescope (ART) to verify real-world applicability.

1.1. Thesis Structure

This thesis is structured as follows: Chapter 2 provides a review of the literature, establishing the context for SSA, the challenges of catalogue generation, and the theoretical development of AR methods. Chapter 3 builds upon this review to identify specific research gaps in LEO surveillance and formulates the primary research objective and questions that guide this investigation. Chapter 4 establishes the theoretical background, covering the principles of astrodynamics, reference frames, and optical detection. Chapter 5 details the various surveillance strategies under investigation, including their operational constraints, and discusses the mechanics of stripe scanning, grid patterns, and leakproof searches. Chapter 6 presents the mathematical framework for the AR methodology, detailing the formulation of the AR and its various forms. Chapter 7 describes the software implementation and methodology, detailing the two-pipeline approach (Baseline and PAR) and the integration of the SPOOK simulation tool. Chapter 8 validates the simulation framework by comparing simulation predictions against real-world observations from ART. Chapter 9 presents and analyses the results from the simulation campaign, comparing the performance of the different strategies and evaluating the efficacy of the pipeline under various parameter settings. Finally, Chapter 10 concludes the thesis by summarising the key findings, addressing the research questions, and providing recommendations for future work.

2

Literature Summary

This chapter describes the literature used to conduct the research in this thesis. In Section 2.1, the fundamentals of space object catalogues are presented to provide context. Section 2.2 examines various surveillance strategies for observing objects in orbits. Section 2.3 discusses the TSA problem and ARs.

2.1. Space Object Catalogue

In order for space to stay economically and technologically available for future generations, it is vital to have a continuously updated catalogue of all objects in Earth orbit. Without comprehensive tracking, the growing population of orbital debris poses collision risks that could trigger cascading destruction (known as Kessler Syndrome) [26], potentially rendering entire orbital bands unusable for decades or centuries and jeopardising trillions in space infrastructure investments. Moreover, the applications relying on space systems are essential to today's everyday life. Telecommunication and navigation services, as well as Earth observation for environmental and disaster control are some examples. The U.S. Space Surveillance Network has catalogued around 45,000 artificial objects in space as of June 2024 [41]. The vast majority of artificial objects remain in orbit, of which about 94% are non-functional objects, commonly known as space debris [9]. It is therefore pivotal to catalogue as many new objects as possible for space to remain safely accessible and to enable responsible traffic management in an increasingly congested orbital environment.

2.1.1. Space Situational Awareness

SSA consists of three major components: space weather, knowledge of the current artificial orbital space object population and the tools to propagate the states of these objects into the future [7], see Figure 2.1.

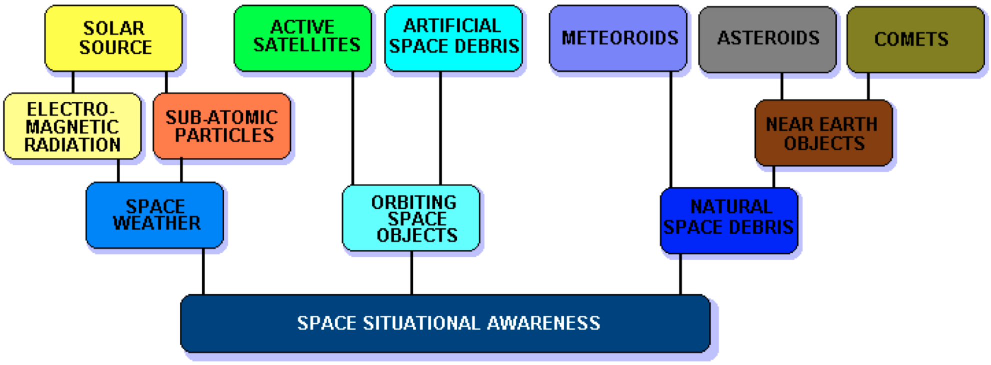

Figure 2.1: Three components of SSA. Image from: [22].

A large part of SSA is made up of creating a catalogue of orbiting space objects with the aim of protecting active assets from collision, minimising the future risk of space debris production. Moreover, SSA extends to gathering knowledge of the space capabilities of each object. Through manoeuvre analysis, spacecraft functionality can be determined. This is useful for applications such as the overpass time of certain spacecraft at a certain point on Earth [22].

Weeden and Samson [54] highlights that a new generation of SSA sensors, along with a growing number of actors seeking to conduct independent SSA analysis, is expected to produce a vast and varied set of measurements and analytical methods. Effectively utilising this wealth of information will require advanced data fusion techniques to create practical tools for planning and operations. To achieve a comprehensive approach to SSA, coordination among these diverse measurements and analytical methods is essential [22]. Consequently, this research is dedicated to the comparison of various surveillance strategies for maximising catalogue generation of LEO objects, as well as investigating different scheduling methods for an increase in successful observations.

2.1.2. Catalogue Generation

As stated previously, in order to achieve efficient SSA it is crucial to build up a space object catalogue, this consists of two parts, generation and maintenance. The entire catalogue generation and maintenance sequence is as follows [9, 36]:

1. Initial detection of objects through systematic surveillance strategies which generates a tracklet
2. Collection of tracklets (sequences of closely-spaced observations) of sufficient quality
3. Initial orbit determination (from correlated tracklets in the case of TSAs)
4. Orbit determination through subsequent observations
5. Orbit refinement and maintenance through additional observations

In catalogue maintenance, tracking observations are performed, leveraging prior knowledge of an object's position to obtain multiple measurements. The object appears as a point source in the Field of View (FoV), while stars appear as streaks. For catalogue generation, without prior information, sidereal observations are conducted, compensating for Earth's rotation. Stars appear as point sources, while satellites appear as streaks due to their angular velocity.

The processing pipeline involves multiple steps: image processing, measurement linking, IOD, and orbit determination. The first step is to process images to extract sky coordinates and/or magnitudes. Software is used for astrometry, identifying objects as points (stars) or streaks (satellites). Stars are matched to a star catalogue to plate solve the images, associating sky coordinates with each pixel [36].

The next step involves linking measurements that plausibly originate from the same object to form tracklets. Due to the close temporal proximity of the measurements, those originating from the same object exhibit well-behaved behaviour (linear movement across the focal plane), applicable to both sidereal and tracking observations [17].

IOD, which can require tracklet correlation in the case of TSAs, is the process of determining a preliminary orbit from a limited set of observations. Vallado [52] describes how techniques such as Gauss's or Gooding's method are typically used to estimate the orbital elements from angular measurements assuming simple two-body dynamics. These initial orbit solutions serve as a starting point for more refined orbit determination processes.

The final step, Orbit Determination (OD), refines the initial orbit estimate by incorporating additional measurements, better quality measurements and better dynamical models. This process typically employs statistical estimation techniques such as batch least squares or Kalman filtering to minimise the difference between observed and predicted measurements [32]. Tapley, Schutz, and Born [47] explain how OD accounts for perturbations from Earth's non-spherical gravity field, atmospheric drag, solar radiation pressure, and third-body gravitational effects to produce accurate orbital solutions. The quality of the orbit determination directly impacts the effectiveness of SSA operations [8].

2.2. Surveillance Strategies

This section examines different approaches to observe and track objects in Earth orbit. The goal is to optimise optical surveillance strategies to increase the number of meaningful observations in as small of a time window as possible.

Xue et al. [56] mentions various strategies of sensor tasking with this goal in mind. One such strategy is the stripe strategy (see Figure 2.2). This strategy uses fixed declination or right ascension values and varies the other. The aim is to allow the maximum number of objects to pass through the stripe(s). In GEO, where the motion is well-known, a leakproof strategy (meaning guaranteed detection opportunities of certain objects) can be easily designed by positioning stripes such that bins are revisited faster than objects are expected to move through them, capturing all objects if bright enough. However, this becomes more challenging when the motion of objects is less predictable or when sensor resources are limited.

Flohrer, Schildknecht, and Musci [10] used such a stripe strategy. The observation campaign employed specialised scanning techniques for different orbital regimes: in GEO, Resident Space Objects (RSO) were monitored through systematic declination stripe scanning, while for Medium Earth Orbit (MEO), RSOs were observed by focusing on right ascension stripes situated at low declination values. This strategy can be implemented using a single stripe [39, 15], pairs of stripes [16], or in multiples, as described by Manresa Ortiz [28]. For multiple stripes, the time interval between consecutive exposures is efficiently utilised, broadening the search area [56]. However, the selection of these strategies depends on the needs of the operator. For example, a single stripe strategy can be effectively used for observations for GEO objects, as the location of the objects is fairly well known and their orbits well-behaved [39]. Multiple pairs can be utilised for situations were the sensors resources must be allocated more delicately or when an object must be observed multiple times in a shorter time span, such as in the case of MEO and LEO objects, as described by Herzog [15].

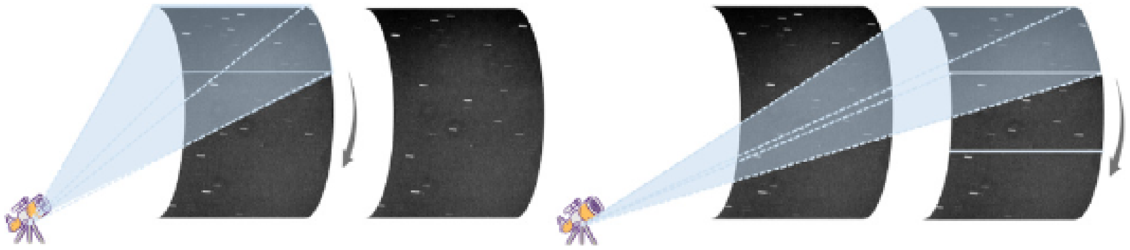

Figure 2.2: Pair of declination stripes. The arrows indicate the repositioning actions. Image from: [56].

This research is primarily interested in strategies dedicated to LEO objects. Mulligan and Stephens [33], describe a so-called bullseye strategy that guarantees an opportunity for detection within a certain area (leakproof). This can be employed to rule out a region of space with certainty, but does not cover the same region of space as quickly as the aforementioned more conventional scans.

Frueh, Fiedler, and Herzog [12] formulate a new strategy by formulating surveillance as an optimisation problem. Weights were assigned to different viewing directions by how many objects were defined in that space in the space objects catalogue. The strategy was then compared to conventional single and two stripe strategies. For the conventional strategy, 63% of the visible objects were observed once within the FoV on a single summer night using the single stripe strategy and 40% twice with the two stripe strategy. For the optimised strategy, 100% of the objects were observed at least once and 80% twice. Although this was applied to GEO objects, this research shows promising results, also for applications in multi-step strategies. This research shows that the use of prior knowledge helps observation efficiency.

Similar work was done by Murphy and Holzinger [34]. They discuss a multi-step search strategy, creating a general framework for searching for unknown space objects with prior knowledge of the region of state space or an uncorrelated track. They use this information to create a follow-up tasking strategy which can occur at a variable location and time. This allowed for optimised follow-up search strategies for GEO short arc observations. This demonstrates the benefits of using known object locations in surveillance strategies.

2.3. Observation Principles

This section examines principles related to making observations for catalogue generation.

2.3.1. Too Short Arcs

Optical measurements from a single short observation arc cannot determine an orbit on their own. The angular position data lacks the range and range-rate information needed to determine the object's precise location in space. This is known as the TSA-problem. Maruskin, Scheeres, and Alfriend [29] address this limitation by fitting the measurements to extract an attributable. An attributable is a partial state the represents the mean angular position and velocity of the object during the observation window. While this reduces noise in the individual measurements, it does not solve the missing range and range-rate problem.

To fill in the missing orbital information, observations from multiple passes are required. When the same object is observed at different points along its orbit, the changing perspective allows the range to be inferred through orbit determination. The difficulty is that before this can be done, the observations must be linked across different passes. Without a known orbit, there is no way to predict where an object will appear next, making it unclear which tracklets correspond to the same object. This represents the problem of tracklet correlation [36, 42]. The steps involved in building a catalogue from observations are outlined in Figure 2.3.

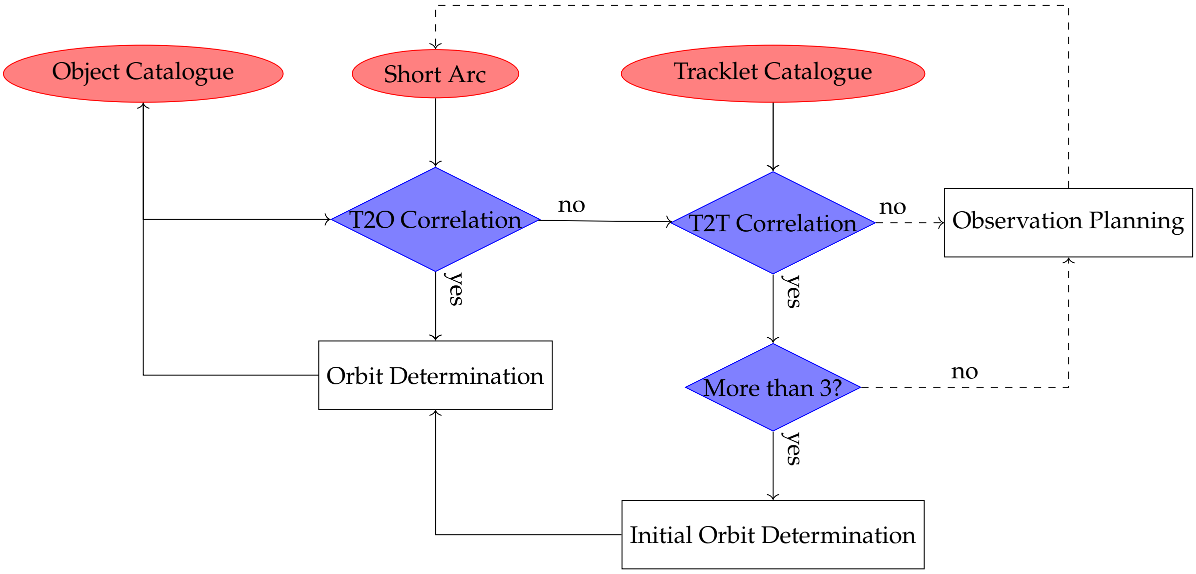

Figure 2.3: Object Catalogue Generation Diagram. T2O stands for Tracklet-to-Object and T2T for Tracklet-to-Tracklet. Image from: [36].

2.3.2. Admissible Region

The AR, first described by Milani et al. [30] and Tommei, Milani, and Rossi [48], describes constrained regions of possible solutions for the unobservable part of the complete state, which would mean the range and range-rate in the case of a tracklets using optical measurements, to create a complete 6D orbit state. The way the admissible part of the AR is defined is through orbits that physically can exist (negative orbital energies) [20]. A complete state in topocentric coordinates is defined as follows:

$$\boldsymbol{x} = [\alpha, \delta, \rho, \dot{\alpha}, \dot{\delta}, \dot{\rho}] \tag{2.1}$$

here, α is the right ascension of the object, δ is the declination of the object, and ρ is the range (distance to the observer). An optical tracklet will retrieve an observable equal to $\mathcal{A} = [\alpha, \delta, \dot{\alpha}, \dot{\delta}]$, this is called the attributable (as mentioned in Subsection 2.3.1). Evidently, the range and range-rate are missing. This is the basis of which the AR approach is built, building a solution space for physically feasible orbits that fit the measured $\mathcal{A}$ by filling in the missing ρ and $\dot{\rho}$ values.

In Keplerian elements, the state can be defined as:

$$\boldsymbol{x} = [a, e, i, \Omega, \omega, \nu] \tag{2.2}$$

where, a is the semi-major axis, e the eccentricity, i the inclination, Ω the right-ascension of the ascending node (RAAN), ω the argument of perigee, and ν the true anomaly. Constraining the semi-major axis and eccentricity values can further constrain the AR and allow for a narrower solution space for possible complete state solutions. The Constrained Admissible Region (CAR) is built around these principles with constraints on the perigee [20] and inclination [18] also being possible. These constraints are then translated to range and range-rate [21]. The CAR has been used by Milani et al. [30] to deal with the problem of identifying asteroids using TSA observations. The same can be done for objects for which only TSA measurements are available. An example CAR is shown in Figure 2.4. In this work, the focus is on constraints on the semi-major axis and eccentricity. These two values are user-defined, aiming to define most likely orbital parameters based on the area of space in question. In the case of (circular-orbit) LEO objects, one can imagine relatively low values for the semi-major axis and eccentricity constraints.

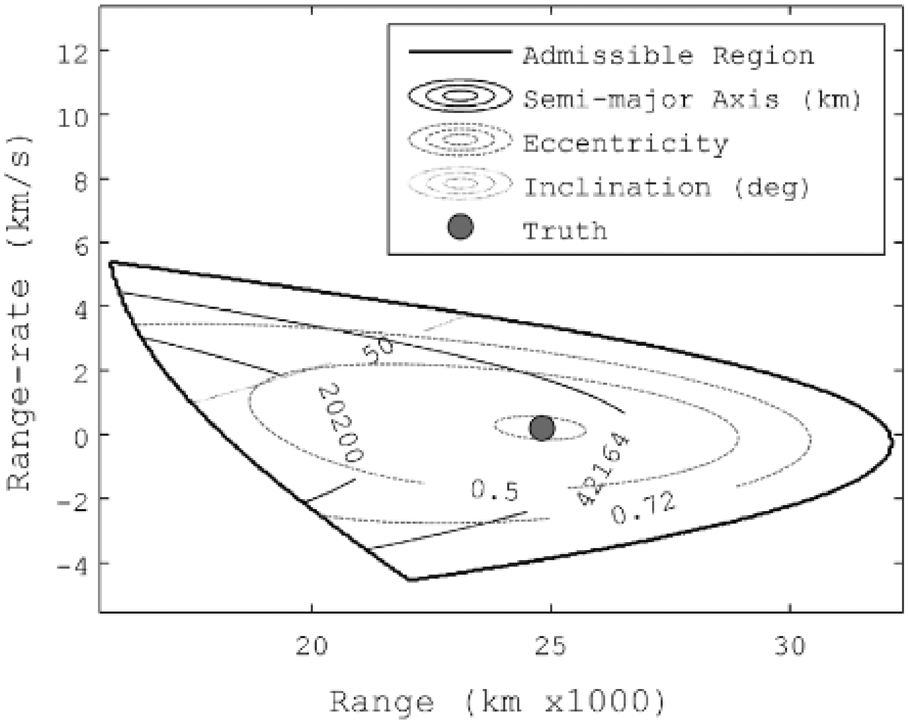

Figure 2.4: Constrained Admissible Region, showing semi-major axis, eccentricity, and inclination limits, which are translated to range and range-rate. Image from: [18].

DeMars, Jah, and Schumacher [5] compared the use of CARs with semi-major axis constraints for near-geosynchronous orbits against angles-only approaches for tracking three closely-spaced RSOs. The CAR method converged to smaller uncertainties in both position and velocity. The primary advantage is its ability to capture the entire region of possible range and range-rate pairs. This research shows the use of CARs, to reduce the uncertainty while still capturing all possible solutions (granted the constraints are selected appropriately).

Sampling the CAR can be done in various ways. Given the lack of statistics on the measurements and orbital elements in the CAR method alone, in most cases, uniform sampling of the CAR is done [20].

However, Hobson et al. [17] showed, using a catalogue based CAR sampling strategy, that sampling uniformly from the CAR may lead to inferior results if more than just the bounds are known about an IOD target's orbital constraints, highlighting the need for an optimised method to sample points within the CAR.

This problem of how to best sample the CAR to perform data association remains a challenge within the field of SSA. For example, DeMars and Jah [6] used a Gaussian Mixture Model (GMM) to approximate the uniform distribution and propagate this for subsequent tracking using an Unscented Kalman Filter (UKF). This showed promising results, tracking every set of data applied to it over a Monte Carlo sampling in a set of synthetic data.

Siminski et al. [44] and Siminski, Fiedler, and Schildknecht [43] used an ISO-energy-grid method to optimise the search pattern within the AR. The search method was shown to reduce computational burden compared to complete sampling. It found feasible orbit solutions in a few iterations, unlike sampling the entire AR, which requires propagating and comparing many possible state solutions to a common epoch.

The aforementioned research demonstrates the superiority of the CAR over the simpler not-constrained AR approach. When prior knowledge of the semi-major axis and eccentricity solution space is available, as is the case for LEO objects (the focus of this work) incorporating these constraints narrows the set of possible states to sample. However, care must be taken in determining how to best sample the CAR.

One way of sampling the CAR aims to achieve a representation of the uncertainty in the variables $(\rho, \dot{\rho})$ given the statistical properties of the angles-only measurement process. Essentially, the goal is to derive a probability density function (pdf) $p(\rho, \dot{\rho})$ that characterises the probability of the range and range-rate space used for the CAR. This Probabilistic Admissible Region (PAR), as described in Hussein et al. [20, 21], improves CAR sampling efficiency by concentrating samples in high-probability regions. Since the range and range-rate probability distribution is typically sparse rather than uniformly distributed across the entire CAR, sampling according to $p(\rho, \dot{\rho})$ rather than uniformly leads to more robust state estimation with fewer samples.

The use of the PAR is to generate possible states based only on incomplete state information derived from single sensor detections. It can also be used for a priori IOD for subsequent observations for tracklet correlation and orbit refinement. Hypotheses can be formed to enable sensor operators to define multiple decision criteria with which one can prioritise sensor tasking [18].

Pedone, Utzmann, and Forstner [36] show the use of a CAR in LEO observations, where most of the aforementioned work looked at GEO data. They describe the limiting factor to be the high angular rates of the objects at LEO, leaving short passages on a sidereal pointing FoV. Real-time stare-and-chase is highlighted to be a possible solution in future developments of this problem. This research shows the usage of CAR approaches in LEO, serving as an initial proof-of-concept of the feasibility of this work.

2.4. Conclusion

Looking at the work mentioned in this chapter, it is clear that in the field of SSA, the problem of TSAs remains relevant, especially for LEO. Several surveillance strategies have been developed and serve as a baseline against which subsequent approaches can be compared. The use of admissible regions has shown promising results in past works, with probabilistic principles (PAR) enhancing the method's effectiveness.

From this literature review on catalogue generation, several research gaps emerge: the collection of tracklets for LEO objects remains challenging, and the practical application of AR methods (specifically PAR) for LEO surveillance is not broadly established. Furthermore, a direct comparison between AR methods and stripe-based approaches is lacking for the LEO regime. This work aims to provide such a comparison. Given the extensive use of these surveillance strategies and admissible region approaches for GEO and MEO documented in this literature review, they serve as an initial validation baseline before analysing the LEO regime.

3

Research Gaps and Questions

Based on the literature review presented in Chapter 2, several key research gaps emerge in the domain of LEO catalogue generation using ground-based optical sensors. This chapter identifies these gaps and formulates the research objectives and questions that will guide this investigation.

The literature reveals that while considerable progress has been made in space object cataloguing techniques, significant challenges remain in optimising surveillance strategies, specifically for LEO objects. The high angular velocities of LEO objects, their brief visibility windows, and the large population density in these orbits create unique challenges that current surveillance methodologies do not fully address.

Several critical gaps have been identified. First, while various surveillance strategies such as stripe scanning have been applied effectively to GEO objects, their application and comparative effectiveness for LEO catalogue generation remains understudied. Studies by Frueh, Fiedler, and Herzog [12] demonstrated significant improvements in GEO object detection rates using optimised strategies compared to conventional approaches, but similar comprehensive comparisons for LEO are lacking. Second, the integration of advanced correlation techniques such as CAR and PAR with specific surveillance strategies for LEO objects is an underdeveloped area. Holzinger et al. [18] showed promising results in IOD using PAR for LEO polar objects, but the application of these techniques in designing optimal multi-step surveillance strategies for LEO catalogue generation requires further investigation. Third, multi-step approaches that leverage initial detection information to optimise subsequent observations have shown potential in studies by Murphy and Holzinger [34] for GEO objects, but their effectiveness for LEO catalogue generation has not been thoroughly explored. The rapid orbital dynamics of LEO objects may present both unique challenges and opportunities for multi-step strategies that differ significantly from those encountered in GEO applications. Finally, while performance comparisons for surveillance strategies have been conducted for GEO objects such as the work by Frueh, Fiedler, and Herzog [12] which shows significant improvement in detection rates, comprehensive comparative analysis of different strategies optimised specifically for LEO catalogue generation remains limited. These identified gaps form the foundation for the research objective and questions presented below.

Research Objective

To evaluate and compare the effectiveness of different surveillance strategies for LEO catalogue generation using ground-based optical sensors under realistic operational constraints.

The research questions below have been formulated to address the identified gaps in the literature:

Research Questions

Which surveillance strategies most effectively contribute to LEO catalogue generation using ground-based optical sensors?

- How do different scanning patterns compare in terms of catalogue generation efficiency?
- How do different surveillance strategies compare for use in a follow-up observation in the case of a multi-step observation?
- How do different parameter settings influence the efficacy of the admissible region approach?

This research will implement various surveillance strategies in simulation and validate findings using ART. By addressing these questions, this study aims to contribute to the development of more efficient approaches for LEO space object cataloguing using passive optical sensors. The investigation will build upon existing methodologies in the field while addressing the specific challenges posed by LEO objects. Both conventional fixed-pattern surveillance strategies and adaptive approaches will be evaluated to determine optimal methods for maximising catalogue generation efficiency under realistic operational constraints.

4

Observation Fundamentals and Astrodynamics

This chapter presents the theoretical foundation underlying the use of optical ground-based telescopes for tracking Earth-orbiting objects and modelling their orbital propagation over time. The following sections describe the theory on reference frames, optical detection, measurement processing, coordinate transformations, and orbital dynamics.

4.1. Reference Frames

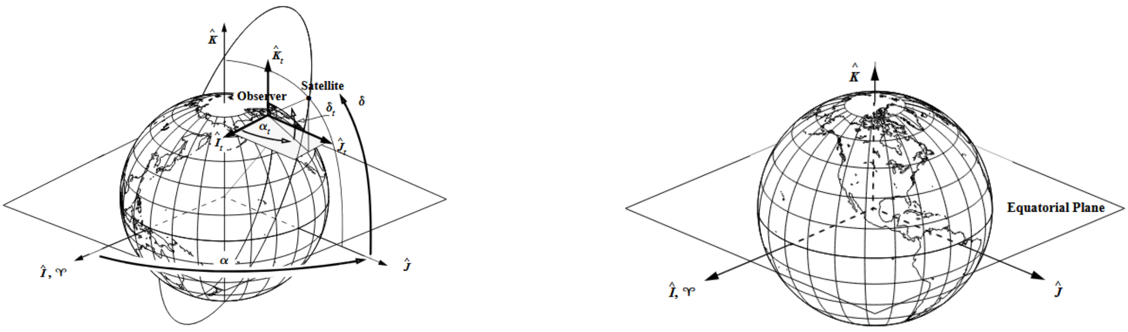

(a) Topocentric Equatorial Coordinate System. Origin at a specific site, typical for optical observations.

(b) ECI Coordinate System. Origin at Earth's centre, commonly used for orbital mechanics.

Figure 4.1: Comparison of Topocentric and ECI Coordinate Systems. Image from [52].

Reference frames provide the necessary coordinate systems to describe the position and motion of objects in orbit. Two primary reference frames are essential for optical tracking of Earth-orbiting objects in this thesis: Earth-Centred Inertial (ECI) frames and the Topocentric Equatorial Coordinate System.

ECI frames have their origin at the centre of the Earth with the z-axis aligned with the Earth's rotation axis pointing toward the north pole. The x-axis points toward the vernal equinox, and the y-axis completes the right-handed system 90° east along the equatorial plane. The fundamental plane is the Earth's equator. These frames are quasi-inertial, meaning they do not rotate with the Earth [52]. In this work, satellite orbital elements from Two-Line Elements (TLEs) are provided in the TEME (True Equator Mean Equinox) frame, while telescope pointing coordinates are computed in the TOD (True of Date) frame. Both are ECI-type coordinate systems that account for precession effects at the observation epoch. The key difference is that TEME uses the mean equinox (averaged over short-period variations) [50], while TOD uses the true equinox that includes nutation corrections. This distinction is important for high-precision pointing: TEME provides efficient orbital propagation from TLE data, while TOD coordinates account for Earth's short-term wobbles, ensuring accurate telescope positioning for observations.

The Topocentric Equatorial Coordinate System is centred at the observation site (topocentre) rather than Earth's centre, with axes parallel to the corresponding ECI frame at the observation epoch. Its fundamental directions are: the z-axis points toward the celestial pole (parallel to the ECI z-axis), the x-axis points toward the vernal equinox (parallel to the ECI x-axis), and the y-axis completes the right-handed system. This system is used for observability computations, as it directly relates to the angular measurements made by telescopes. In this system, objects are located by their right ascension (α, measured eastward from the vernal equinox) and declination (δ, measured north or south from the celestial equator), which are analogous to longitude and latitude on the celestial sphere. Elevation and azimuth angles derived from the topocentric frame are used to determine whether a satellite meets minimum elevation and Sun/Moon separation constraints. These coordinate systems can be found in Figure 4.1. The geometric relationship between the observer's position, satellite position in the ECI frame, and the line-of-sight range is illustrated in Figure 4.2.

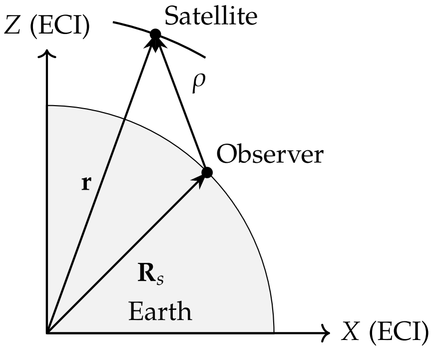

Figure 4.2: Geometric relationship between observer position ($\mathbf{R}_S$), satellite position in ECI frame ($\mathbf{r}$), and line-of-sight range (ρ) used for computing topocentric observability constraints.

4.2. Optical Detection

Ground-based optical systems represent an important infrastructure component for space surveillance activities. To detect sunlight reflected from objects in Earth orbit, optical sensors are needed to capture these light waves using lenses and store the resulting images. In this thesis, the telescope used for experimental validation is ART (see Appendix A), a remotely operated telescope in Spain equipped with a Complementary Metal-Oxide-Semiconductor (CMOS) camera, which captures and stores images of sunlight reflected from objects in Earth orbit.

CMOS detectors are characterised by three key parameters. Quantum efficiency (QE) measures the fraction of incident photons converted to electronic signal. Modern scientific CMOS sensors achieve 60–90% efficiency. Read noise (σ_{read}) represents electronic noise during pixel readout, typically 1–5 electrons per pixel. Dark current (I_{dark}) captures thermally generated noise accumulated during exposure, usually 0.001–0.05 electrons/pixel/second [49, 19].

The relations between these parameters determine the signal-to-noise ratio (SNR) achievable for a given observation, which Howell [19] expresses as:

$$\mathrm{SNR} = \frac{N_*}{\sqrt{N_* + n_{\mathrm{pix}}(N_S + N_D + \sigma^2_{\mathrm{read}})}} \tag{4.1}$$

where N_* is the total source signal in electrons from the target object, n_{pix} is the number of pixels in the measuring aperture, N_S is the sky background contribution per pixel in electrons, N_D is the dark current contribution per pixel in electrons, and σ^2_{read} is the total number of electrons per pixle from the read noise.

Detection of orbital objects requires specialised exposure techniques. Three primary methodologies are employed [39, 53]:

1. **Sidereal tracking**: The telescope tracks at the sidereal rate matching Earth's rotation (15.041 arcsec/s), causing stars to appear as point sources while orbital objects manifest as streaks. This technique provides excellent SNR for stars (used as astrometric reference points) while allowing velocity vector estimation for detected objects.
2. **Rate tracking**: The telescope tracks at the expected angular rate of the target object, causing it to appear as a point source while stars appear as streaks. This method maximises SNR for known objects but complicates astrometric reduction (see Section 4.3) due to streaked reference stars.
3. **Streak detection**: Employing fixed-pointing or very short exposures to capture instantaneous positions of objects as they transit the field of view. This approach is particularly useful for wide-field survey operations but imposes greater requirements on detector sensitivity.

An example of each exposure technique can be found in Figure 4.3.

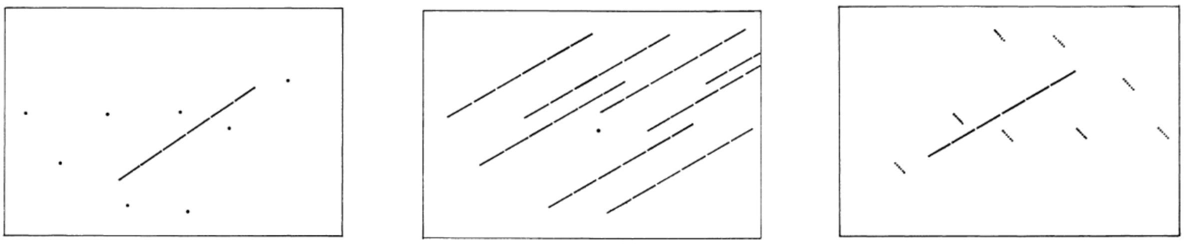

(a) Sidereal tracking **(b)** Rate tracking **(c)** Streak detection

Figure 4.3: Various tracking methods. In (a), the stars appear as dots, and the satellite as a streak. In (b), the satellite appears as the dot while the stars as streaks. Lastly, in (c), the long streak shows the satellite and the shorter streaks the stars. The direction of the star streaks in this image is due to the short rotation of the Earth and the direction of the satellite streak is associated with its direction of movement. The satellite streak remains straight due to the images being taken at a fixed point. Image from: [53].

4.3. Coordinate Transformations

The transformation of raw pixel measurements to astronomical coordinates is a necessary step to make sense of sensor readings. This section describes the steps required to convert pixel coordinates to topocentric celestial coordinates.

The detection of an object in an optical image initially yields pixel coordinates (x_p, y_p) within the detector reference frame. Because optical observations typically provide angles-only measurements, the transformation process yields topocentric right ascension and declination (α, δ) without direct range information. These angular measurements must be transformed through multiple stages to obtain the celestial coordinates required for subsequent orbital analysis. The astrometric plate solution typically employs a polynomial model relating pixel positions to standard coordinates as described by Veis [53]. This process is known as astrometric reduction or plate solving [9].

The resultant observation consists of a time-stamped pair of angular measurements expressed as topocentric right ascension and declination (α, δ, t) referenced to the J2000.0 epoch. For orbit determination and propagation, the angular rates $\dot{\alpha}$ and $\dot{\delta}$ are also required. In practical optical observations, a series of consecutive measurements are typically collected and grouped into tracklets. From these sequential observations, an attributable vector can be derived, which consists of four parameters representing the angular position and angular velocity at a reference epoch (as described previously):

$$\mathcal{A} = [\alpha, \delta, \dot{\alpha}, \dot{\delta}] \tag{4.2}$$

The attributable encapsulates the observational information available from a short-arc optical observation sequence. Several methods exist to determine the attributable from a set of angular measurements in a tracklet. A common approach involves polynomial fitting of the angular motion, typically using a second-order model to account for the slightly non-linear motion of objects over the observation period.

The fitting process generally employs least squares techniques that minimise the residuals between measured angles and the polynomial model, weighted by the measurement uncertainty [29].

The precision of the derived angular rates depends on several factors including the number of measurements in the tracklet, the temporal spacing between observations, and the inherent measurement precision of the optical system. Generally, wider temporal spacing improves angular rate determination but risks complications from non-linear motion, especially for LEO objects. With sufficient temporal spacing, the tracklet is no longer a TSA and IOD can be performed.

For optical observations, the complete measured attributable also consists of the observation time t: $(\alpha, \delta, \dot{\alpha}, \dot{\delta}, t)$. When multiple observations are available, statistical orbit determination techniques can be applied to refine the estimate of the orbital state, see Chapter 6.

4.4. Orbital Dynamics

The transformation of optical measurements into orbital elements and the subsequent propagation of the object state are the final steps of catalogue generation. This section establishes the mathematical foundation for orbit determination and propagation.

4.4.1. Two-Body Problem

The fundamentals of orbital motion follow from the two-body problem, where the satellite motion is described by Newton's law of gravitation:

$$\ddot{\mathbf{r}} = -\frac{\mu}{r^3}\mathbf{r} \tag{4.3}$$

where $\mathbf{r}$ is the position vector, $\mu = GM_E = 398600.4418\ \text{km}^3/\text{s}^2$ is Earth's gravitational parameter, and $r = |\mathbf{r}|$.

The resulting orbit can be expressed either as a Cartesian state vector $\mathbf{X} = [x, y, z, \dot{x}, \dot{y}, \dot{z}]^T$ in the ECI frame, or as a set of classical Keplerian orbital elements $(a, e, i, \Omega, \omega, \nu)$ [52, 4]:

- a: Semi-major axis (km), defining the orbit's size
- e: Eccentricity (dimensionless), defining the orbit's shape ($e = 0$ for circular, $0 < e < 1$ for elliptical)
- i: Inclination (degrees or radians), the angle between the orbital plane and the equatorial plane
- Ω: Right ascension of ascending node (RAAN, degrees or radians), defining the longitude where the satellite crosses the equatorial plane from south to north
- ω: Argument of perigee (degrees or radians), the angle from the right ascension to the perigee point within the orbital plane
- ν: True anomaly (degrees or radians), the angle from perigee to the satellite's current position

A visualisation of these elements can be found in Figure 4.4.

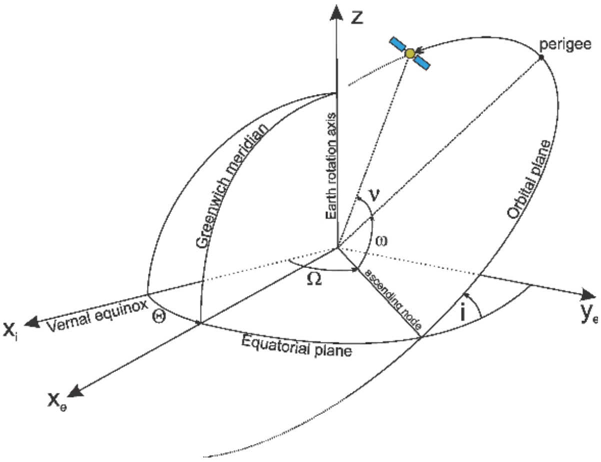

Figure 4.4: Keplerian orbital elements. Image from: [57].

4.4.2. Perturbation Forces

Real orbital motion deviates from the ideal two-body problem due to various perturbing forces. Orbit propagation requires modelling of these perturbations acting on the orbiting object. The equations of motion with perturbations can be expressed as [52, 4]:

$$\ddot{\mathbf{r}} = -\frac{\mu}{r^3}\mathbf{r} + \mathbf{a}_{J_2} + \mathbf{a}_{\text{drag}} + \mathbf{a}_{\text{3-body}} + \mathbf{a}_{\text{SRP}} + \ldots \tag{4.4}$$

where the additional acceleration terms represent perturbations due to:

- $\mathbf{a}_{J_2}$: Earth's oblateness (dominant perturbation for most orbits), given by:

$$\mathbf{a}_{J_2} = \frac{3}{2}\frac{J_2 \mu R_e^2}{r^5}\begin{bmatrix} x\left(5\frac{z^2}{r^2} - 1\right) \\ y\left(5\frac{z^2}{r^2} - 1\right) \\ z\left(5\frac{z^2}{r^2} - 3\right) \end{bmatrix} \tag{4.5}$$

  where $J_2 = 1.08263 \times 10^{-3}$ is Earth's second zonal harmonic coefficient and $R_e = 6378.137$ km is Earth's equatorial radius.

- $\mathbf{a}_{\text{drag}}$: Atmospheric drag:

$$\mathbf{a}_{\text{drag}} = -\frac{1}{2}\rho_{atm}\frac{C_D A}{m}|\mathbf{v}_{\text{rel}}|\mathbf{v}_{\text{rel}} \tag{4.6}$$

  where ρ_{atm} is atmospheric density (altitude-dependent), C_D is the drag coefficient (typically 2.0–2.5), A is the effective cross-sectional area, m is the object's mass, and $\mathbf{v}_{\text{rel}}$ is the velocity relative to the rotating atmosphere.

- $\mathbf{a}_{\text{3-body}}$: Third-body gravitational effects, primarily from the Sun and Moon
- $\mathbf{a}_{\text{SRP}}$: Solar radiation pressure

4.5. Chapter Summary

This chapter presented the theoretical foundation for the optical tracking of Earth-orbiting objects. It began by defining the required coordinate systems, the ECI frame for orbital propagation and the Topocentric Equatorial Coordinate System for ground-based observations. The principles of optical detection were described, including sensor characteristics and the primary tracking methods (sidereal, rate, and streak). The process of coordinate transformation was then described, showing how raw image data is converted via astrometric reduction into an attributable vector (α, δ, $\dot{\alpha}$, $\dot{\delta}$). Finally, the chapter reviewed the principles of orbital dynamics, progressing from the ideal two-body problem to the inclusion of perturbation forces, such as Earth's oblateness (J2) and atmospheric drag, which are required for LEO propagation. This astrodynamic framework serves as the basis for the propagation and observation models used in this research.

5

Surveillance Strategies

This chapter examines space surveillance strategies applied to LEO catalogue generation. The formulation builds upon established methodologies in the literature.

5.1. Constraint Formulation

Optical observations of orbiting objects require three primary visibility constraints to be satisfied. These constraints ensure the object is illuminated, the observer is in darkness, and interference from celestial bodies is minimised.

Constraint 1: Phase Angle

The phase angle θ is the angle between the observer, the object, and the Sun (observer-object-Sun). For the object to be visible, it must be illuminated by the Sun while the ground-based observer is in Earth's shadow [9]. This requires:

$$0^\circ \leq \theta \leq \theta_{\max} \tag{5.1}$$

where $\theta_{\max}$ depends on instrumental and operational constraints, ensuring the Sun does not appear in the FoV.

Constraint 2: Sun and Object Elevation Angles

Two elevation angle constraints need to be satisfied simultaneously. First, the Sun must be sufficiently below the horizon to ensure dark sky conditions. A minimum Sun elevation angle of -9° (nautical twilight) is typically used, as shown in Figure 5.1. Although the Sun is technically below the horizon at 0°, the -9° threshold prevents stray light when the Sun is close to the horizon, which would otherwise interfere with detection of dim objects

Second, the target object must be above the horizon with sufficient elevation to minimise atmospheric effects. A minimum object elevation angle of $+20^\circ$ is enforced to ensure the object is accessible and to minimise atmospheric refraction and signal attenuation. At low elevation angles, reflected light must travel through significantly more atmosphere, which attenuates the signal and degrades observation quality.

Constraint 3: Moon Separation Angle

To prevent the Moon from interfering with observations of dim orbital objects, a minimum angular separation between the Moon and the target object must be maintained. For this thesis, a minimum Moon separation angle of 5° is implemented.

5.2. Surveillance Strategies

In order to survey the areas of space, surveillance strategies must be employed. The selection of an appropriate surveillance strategy directly impacts the efficiency of search operations and the probability of successful object detection.

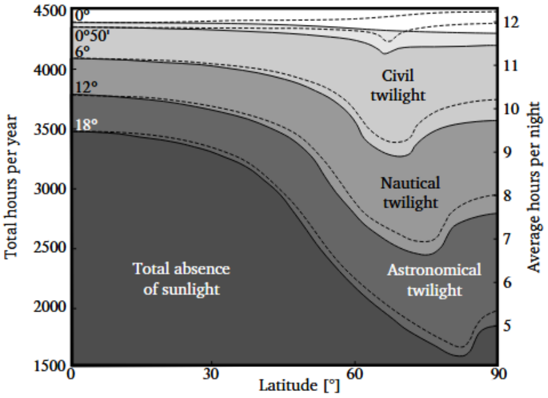

Figure 5.1: Average night time for different twilight conditions, with Northern Hemisphere shown as solid lines and Southern Hemisphere as dashed lines, with minimum elevation angles indicated above them. Image from [9].

5.2.1. Declination & Right ascension Stripe Scanning

One approach for systematic sky surveys involves scanning along declination stripes. The method involves fixing the telescope at a constant right ascension and scanning up and down in declination while following the stars. This creates a vertical "fence" in the sky through which satellites drift due to their orbital motion. This technique is typically used for GEO surveillance [39].

For declination stripe scanning, the scanning trajectory follows:

$$\alpha(t) = \alpha_c \tag{5.2}$$

$$\delta(t) = \delta_0 + v_\delta \cdot t \tag{5.3}$$

where α_c is the fixed right ascension coordinate of the stripe, v_δ is the scanning velocity in declination, and δ_0 defines the starting declination. In practice, this continuous motion is implemented as discrete pointings: the telescope dwells at fixed (α_c, δ_i) positions for exposure time, then repositions to the next declination step. The spacing between pointings is determined by the FoV and overlap requirements.

This approach is particularly effective for GEO surveillance because GEO satellites appear nearly stationary relative to Earth but exhibit slow drift relative to the fixed stars. By maintaining a fixed right ascension and repeatedly scanning in declination, the telescope creates a observational fence that captures objects as they drift through the stripe. An illustration can be found in Figure 5.2.

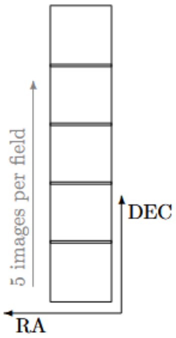

Figure 5.2: Observation sequence for a declination stripe. Image from: [15].

Right ascension stripe scanning is an alternative approach where the telescope scans along fixed right ascension coordinates while varying declination. This strategy proves particularly effective for certain orbital regimes and observational geometries, such as MEO [56].

For right ascension stripe scanning, the stripe is defined by a central right ascension value α_c and spans a width w_α typically measured in hours of right ascension. The relationship between angular width and time is:

$$w_{\alpha,\text{deg}} = w_{\alpha,\text{hours}} \cdot 15^\circ/\text{hour} \tag{5.4}$$

The scanning trajectory follows:

$$\alpha(t) = \alpha_0 + v_\alpha \cdot t \tag{5.5}$$

$$\delta(t) = \delta_c \tag{5.6}$$

where v_α is the scanning velocity in right ascension and α_0 defines the starting declination position. As for the declination stripe, in reality, the continuous motion is implemented as discrete pointings at fixed (α_c, δ_i) positions for exposure time before moving on. Flohrer, Schildknecht, and Musci [10] demonstrated its utility for MEO by focusing on right ascension stripes situated at low declination values. This effectiveness stems from MEO orbital geometry. Objects in this regime cross the celestial equator approximately twice per 6-hour orbital period, ensuring that right ascension scanning along low declinations intercepts the majority of the MEO population during a single observation night.

The number of pointing positions required within a right ascension stripe depends on the FoV and desired overlap factor. For a stripe of width $w_{\alpha,\text{hours}}$ hours in right ascension:

$$N_{\text{positions}} = \left\lceil \frac{w_{\alpha,\text{hours}} \cdot 15}{w_{\text{FoV,eff}}} \right\rceil \tag{5.7}$$

where the effective FoV accounts for overlap:

$$w_{\text{FoV,eff}} = w_{\text{FoV}} \cdot (1 - f_{\text{overlap}}) \tag{5.8}$$

The time required to scan a complete stripe depends on the number of images and the total observation time per position:

$$T_{\text{stripe}} = N_{\text{images}} \cdot (t_{\text{exposure}} + t_{\text{readout}} + t_{\text{slew}}) \tag{5.9}$$

5.2.2. Multi-Stripe Strategy

The single-stripe strategy is the simplest implementation of stripe scanning. A single continuous sweep covers the search region. The multi-stripe approach extends single-stripe scanning by implementing parallel tracks across the search region. If the combined exposure and detector readout time is less than the time interval required for desired overlapping coverage, multiple declination stripes may be observed simultaneously [39]. See Figure 5.3. The number of required stripes N_s depends on the search region dimensions:

$$N_s = \left\lceil \frac{L_\delta}{w_{FoV}} \right\rceil \tag{5.10}$$

where L_δ is the characteristic dimensions in declination of the search region (L_α in the case of right ascension stripes). Each stripe i follows the trajectory:

$$\delta_i(t) = \delta_0 + v_\delta \cdot t \tag{5.11}$$

$$\alpha_i = \alpha_0 + i \cdot w_{FoV} \tag{5.12}$$

The strategy includes transition periods between stripes, introducing dead time where no observations occur. For N stripes with desired overlap factor f, the available time per exposure becomes:

$$t_{\text{exp}} = \frac{t_{\text{field}}}{N \cdot f} \tag{5.13}$$

where t_{field} is the time for a field to transit the FoV.

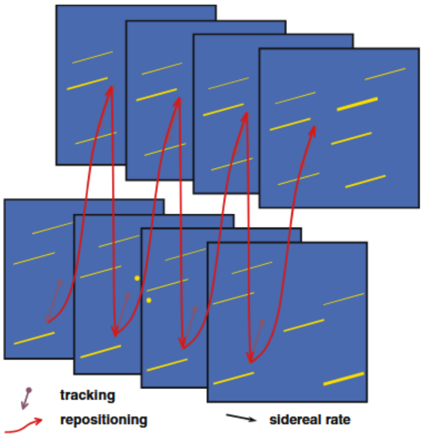

Figure 5.3: Simultaneous scanning of two declination stripes. Image from: [39].

5.2.3. Grid Strategy

A simple strategy is the to descritise the search region into a grid. The grid is made up of cells corresponding to individual pointing positions. For a grid with $N_\alpha \times N_\delta$ cells, pointing positions are:

$$\alpha_{i,j} = \alpha_{\text{min}} + \left(i + \frac{1}{2}\right) \cdot \frac{L_\alpha}{N_\alpha} \tag{5.14}$$

$$\delta_{i,j} = \delta_{\text{min}} + \left(j + \frac{1}{2}\right) \cdot \frac{L_\delta}{N_\delta} \tag{5.15}$$

The grid strategy requires determining an optimal sequencing pattern to minimise telescope slewing time while maintaining coverage.

5.2.4. Leakproof Search Strategies

Non-leakproof survey patterns cannot guarantee detection even when objects are within the searched area, as moving objects may transition from unsearched to previously searched regions. Stripe strategies can be made leakproof for desired areas of interest such as GEO in the case of declination stripes. Mulligan and Stephens [33] introduce a leakproof search pattern that kinematically guarantees detection opportunities for objects within specified constraints.

The so-called bullseye pattern consists of overlapping concentric rings of discrete dwells, as illustrated in Figure 5.4. A leakproof search pattern ensures that any object moving slower than maximum angular rate ω_{max} within the search area will be detected.

The pattern must satisfy leakproof constraints ensuring ring boundaries account for object motion during observation. However, the bullseye approach becomes ineffective when object angular rates exceed sensor capabilities. Mulligan and Stephens [33] define the "point of futility" as:

$$\frac{\omega_{max}(\tau + t_s)}{\Psi} \gtrsim 0.05 \tag{5.16}$$

where τ is the integration time, t_s is the slew time, and Ψ is the sensor FoV. Beyond this threshold, bullseye patterns cannot establish leakproof areas larger than a single FoV.

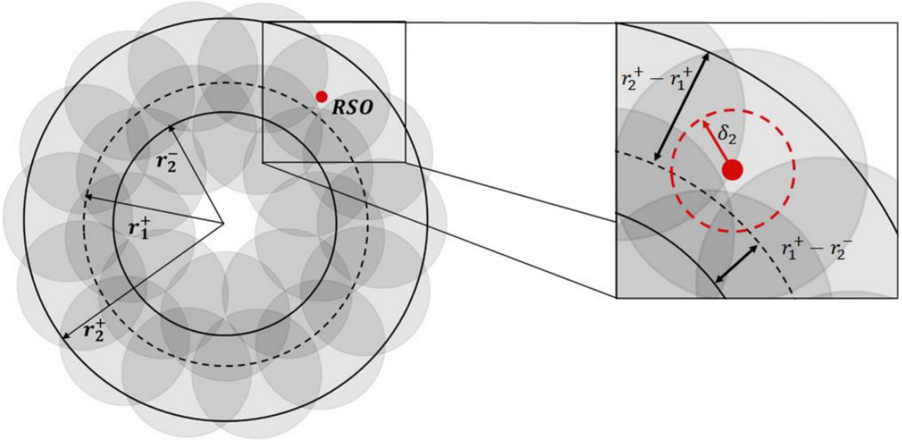

Figure 5.4: Bullseye search pattern showing concentric rings of overlapping dwells. Image from: [33].

The bullseye pattern is interesting as it introduces a leakproof strategy that can be applied for different sensors and orbital regimes, unlike stripe strategies that are not leakproof if used for LEO if only one sensor is used.

LEO Applicability Limitations

In this thesis, LEO is the regime of interest. The bullseye strategies is analysed in order to serve as way to compare against AR approaches. The following subsection explains why the bullseye strategy was declared not feasible for the purpose of this work.

For LEO objects, typical angular velocities range from 0.1-1.0 deg/s, significantly higher than GEO objects at 0.001-0.01 deg/s. Table 5.1 presents a representative LEO scenario for evaluating the futility criterion. The futility criterion becomes:

Table 5.1: Representative LEO scenario parameters for bullseye pattern feasibility assessment.

Parameter	Value	Description
ω_{max}	0.5 deg/s (1800 arcsec/s)	Maximum angular velocity
τ	2.0 s	Exposure + Read-out Time
t_s	5 s	Telescope slew time
Ψ	3.18 deg (11448 arcsec)	ART sensor field of view (Appendix A)

$$\frac{1800 \times (2.0 + 5)}{11448} = \frac{9900}{11448} \approx 1.10 \gg 0.05 \tag{5.17}$$

This greatly exceeds the futility threshold, indicating that leakproof bullseye patterns are impractical for LEO surveillance when using a telescope similar to ART due to the high angular velocities involved.

5.3. Chapter Summary

This chapter provided an examination of space surveillance strategies relevant to LEO catalogue generation. It first established the three visibility constraints, phase angle, Sun and object elevation, and Moon separation, that govern ground-based optical observations. Following this, the chapter described the formulation and operational mechanics of several survey patterns. These included "fence" approaches like declination and right ascension stripe scanning, multi-stripe strategies, and grid strategy. Leakproof search strategies, specifically the "bullseye" pattern, were also analysed. A finding of this chapter was the demonstration of the bullseye pattern's infeasibility for LEO surveillance with ART. The high angular velocity of LEO objects causes the "point of futility" criterion to be exceeded, making the strategy impractical. The remaining strategies described here form the basis for the "Baseline Pipeline" (see Chapter 7) that will be implemented and tested. While these strategies provide coverage of the observable sky, they treat all regions equivalently without incorporating prior knowledge of detected objects. Chapter 6 introduces the mathematical framework for an alternative approach that leverages initial detection information through AR techniques to guide subsequent observations.

6

Mathematical Background and Admissible Regions

This chapter establishes the mathematical foundation for the analysis methods employed in this research. The techniques presented here enable the characterisation of orbital populations through Gaussian Mixture Models (GMMs). The problem formulation for follow-up observations is presented, and the search region discussion is extended to ARs. The frameworks described form the basis for the methodology and analysis presented in subsequent chapters.

6.1. Gaussian Mixture Models for Orbital Populations

GMMs are used to approximate an arbitrary distribution as a weighted sum of Gaussian pdfs, which are easier to work with mathematically. This can be applied to characterise orbital element distributions within satellite populations and to subsequently synthetic populations for simulation purposes. In this work, this is used to identify high-value sky regions for targeted surveillance strategies.

The primary data source for orbital population analysis consists of TLE sets [51], which are standardised orbital parameter descriptions maintained by the U.S. Space Force. Each TLE provides data of a satellite's Keplerian orbital elements at a specific epoch [3]. For a catalogue containing N tracked objects, the orbital elements are extracted to construct a dataset $\{\mathbf{x}_n\}_{n=1}^{N}$, where each observation is a single satellite's orbital state.

The GMM fitting process transforms this satellite distribution into a parametric probabilistic model. This learned model serves multiple purposes: (1) identifying distinct orbital families or constellations within the population, (2) generating synthetic satellite populations for Monte Carlo simulations, (3) predicting high-density orbital regions for effective surveillance, and (4) detecting orbits that deviate from established patterns. In this thesis, the GMM is used for generation of synthetic populations for surveillance strategies.

A GMM describes a probability density function (pdf) as a weighted sum of K Gaussian components [2]:

$$p(\mathbf{x}) = \sum_{k=1}^{K} \pi_k \mathcal{N}(\mathbf{x}|\boldsymbol{\mu}_k, \boldsymbol{\Sigma}_k) \tag{6.1}$$

The mixing weights π_k satisfy $\sum_{k=1}^{K} \pi_k = 1$ and $\pi_k \geq 0$, while $\boldsymbol{\mu}_k$ and $\boldsymbol{\Sigma}_k$ are the component means and are covariance matrices, respectively. The multivariate Gaussian distribution is defined as [46]:

$$\mathcal{N}(\mathbf{x}|\boldsymbol{\mu}, \boldsymbol{\Sigma}) = \frac{1}{(2\pi)^{d/2}|\boldsymbol{\Sigma}|^{1/2}} \exp\left(-\frac{1}{2}(\mathbf{x} - \boldsymbol{\mu})^T \boldsymbol{\Sigma}^{-1}(\mathbf{x} - \boldsymbol{\mu})\right) \tag{6.2}$$

where d is the dimensionality of the data space. For space surveillance applications, the feature vector comprises five Keplerian orbital elements extracted from TLE data:

$$\mathbf{x} = [a, e, i, \Omega, \omega]^T \tag{6.3}$$

The GMM parameters $\{\pi_k, \boldsymbol{\mu}_k, \boldsymbol{\Sigma}_k\}_{k=1}^K$ are fit to the observed orbital element dataset $\{\mathbf{x}_n\}_{n=1}^N$ using the Expectation-Maximisation (EM) algorithm. This method iterates between two steps until convergence is reached [46]:

Expectation Step: Compute the posterior probability that observation $\mathbf{x}_n$ belongs to component k:

$$\gamma_{nk} = \frac{\pi_k \mathcal{N}(\mathbf{x}_n | \boldsymbol{\mu}_k, \boldsymbol{\Sigma}_k)}{\sum_{j=1}^K \pi_j \mathcal{N}(\mathbf{x}_n | \boldsymbol{\mu}_j, \boldsymbol{\Sigma}_j)} \tag{6.4}$$

Maximisation Step: Update the model parameters using the weighted statistics:

$$\boldsymbol{\mu}_k^{new} = \frac{1}{N_k} \sum_{n=1}^N \gamma_{nk} \mathbf{x}_n \tag{6.5}$$

$$\boldsymbol{\Sigma}_k^{new} = \frac{1}{N_k} \sum_{n=1}^N \gamma_{nk} (\mathbf{x}_n - \boldsymbol{\mu}_k^{new})(\mathbf{x}_n - \boldsymbol{\mu}_k^{new})^T \tag{6.6}$$

$$\pi_k^{new} = \frac{N_k}{N} \tag{6.7}$$

where $N_k = \sum_{n=1}^N \gamma_{nk}$ is the effective number of observations assigned to component k. The algorithm iterates between these steps until the log-likelihood converges or a maximum iteration count is reached.

Synthetic Population Generation

Once the GMM has been fitted to the data, the generation of synthetic orbital element sets through Monte Carlo sampling becomes possible:

1. Sample component index k from the distribution defined by $\{\pi_k\}$
2. Sample orbital elements $\mathbf{x}$ from $\mathcal{N}(\boldsymbol{\mu}_k, \boldsymbol{\Sigma}_k)$
3. Apply constraint validation and coordinate transformations

To complete the Keplerian state a random value for the true anomaly θ between 0 and 2π is selected. Through the generation of this synthetic population it is possible to simulate unknown space objects in orbits using similar characteristics to their catalogued counterparts. This set of synthetic elements is then propagated over time for subsequent (follow-up) strategies.

6.2. Problem Definition

Space surveillance for catalogue generation poses an optimisation challenge different from traditional tracking scenarios. Unlike conventional tracking, where objects have known approximate locations, surveillance operates without precise a priori knowledge of object positions [9]. This uncertainty requires coverage strategies that balance detection probability against resource constraints while searching through the complete set of possible orbits [56]. The challenge is particularly acute for LEO objects, where brief visibility windows and high angular velocities severely constrain observation opportunities.

Following Murphy and Holzinger [34], the surveillance problem can be written as dynamic state evolution. Let $\mathcal{X}$ represent the complete state space containing all possible satellite orbital states. The surveillance problem focuses on a search set $\mathcal{S}(t_0) \subset \mathcal{X}$ that evolves over time as satellites orbit the Earth. Given the dynamical system:

$$\dot{x} = f(x) \tag{6.8}$$

Objects within the search set evolve according to the flow function:

$$x(t_1) = \Phi(t_1; x(t_0), t_0) \tag{6.9}$$

where Φ denotes the flow function which represents the orbital propagation operator that evolves states according to the dynamics of $f(x)$. Consequently, the search set itself evolves as:

$$S(t) = \Phi(t; S(t_0), t_0) \tag{6.10}$$

This formulation captures the surveillance challenge: as time progresses, the search region typically expands, requiring increasingly extensive observation campaigns to maintain adequate coverage. For a sensor with measurement function $h : \mathcal{X} \to \mathcal{H}$, the search set projects into the measurement space as (see Figure 6.1):

$$S_{\mathcal{H}} = h(S) = \{x_{\mathcal{H}} : x_{\mathcal{H}} = h(x), x \in S\} \tag{6.11}$$

where $\mathcal{H}$ is the measurement subspace accessible to the sensor. So $S_{\mathcal{H}}$ is the measurement space resulting from the measurement function, and $x_{\mathcal{H}}$ is the component that can be measured by a particular observer which exists within the subspace $S_{\mathcal{H}}$.

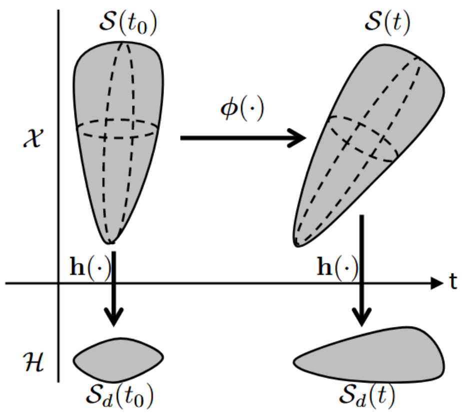

Figure 6.1: Evolution of measurement space $S_{\mathcal{H}}$. Image from: [34].

The optimisation objective maximises the weighted sum of viewing directions over an observation window. This can be expressed as [11, 27]:

$$\mathcal{J} = \max \sum_{f=1}^{m_g} \left(\sum_{i=1}^{n} \mu(\hat{x}_i) \cdot p(\hat{x}_i) \cdot d(h, \hat{x}_i) \right) \tag{6.12}$$

where m_g is the total number of viewing directions in an observation window, n is the number of objects to be observed, $\mu(\hat{x}_i)$ quantifies the object-specific observational value (typically based on uncertainty criteria or information gain), $p(\hat{x}_i)$ is the detection probability for object i derived from the probability distribution, and $d(h, \hat{x}_i)$ is the probability that object i falls within the sensor's search set h. Using this function viewing directions can be selected that maximise detection rates. This shows that the propagation of the measurement space $S_{\mathcal{H}}$ evolves differently to its state space S counterpart. When designing a surveillance strategy for initial detection or for follow-up the evolution of the measurement space is what has to be taken into account.

The search set h is determined by the FoV and sensor constraints (see Section 5.1). A more detailed representation of the search set in the form of ARs is described in Section 6.4.

6.3. Search Region Analysis

Looking back at the search regions $S(t)$, an analysis of the region is necessary to accurately survey this space. Murphy and Holzinger [34] mention the area A_h of the search region to be a useful factor in the analysis of $S(t)$. The size of the search region directly affects the feasibility of tracking a set of objects. In realistic scenarios, velocity uncertainties cause the search set to expand spatially over time. Each observation reduces the remaining search area by constraining possible object locations. A successful search strategy requires the observation-space reduction rate to exceed the rate of spatial expansion. Given the constraints of dealing with high dimensional sets (6 orbital elements) a problem arises in the measurement of this area. The area becomes a function of the search set which in turn is a function of time itself:

$$A_h(S(t)) = |S|_{\mathcal{H}} \tag{6.13}$$

A search set is best analysed by projecting it into a specific observer's measurement space. This allows the search space to be evaluated according to that observer's constraints and reference frame. The time evolution of these regions is determined by the velocity vector field and higher-order derivatives, with the divergence of these fields at the region boundary controlling the behaviour. This boundary analysis enables analytical solutions for how the search region area changes over time, which is needed for developing follow-up observation strategies.

Consider the projection mapping $h : \mathbb{R}^6 \to \mathbb{R}^4$ that transforms orbital state vectors into the measurement space coordinates of right ascension, declination and their time derivatives. The search region boundary $\partial S(t)$ in state space projects to a corresponding boundary $\partial S_{\mathcal{H}}(t)$ in measurement space:

$$\partial S_{\mathcal{H}}(t) = h(\partial S(t)) \tag{6.14}$$

The divergence of this projected velocity field along the boundary determines the rate of area change. Figure 6.2 illustrates the projection geometry of search regions, showing how high-dimensional state uncertainty regions project into the two-dimensional measurement space. The divergence of this projected velocity field along the boundary determines the rate of area change. Regions with positive divergence expand rapidly, requiring increased observation frequency to maintain coverage, while regions with negative divergence expand slowly, allowing for a lower observation frequency.

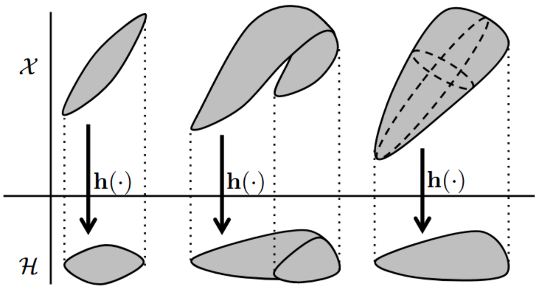

Figure 6.2: Projection mapping from state space to measurement space. Image from: [34].

This challenge of managing expanding search spaces makes surveillance for catalogue generation particularly difficult, especially for LEO objects. When designing a follow-up strategy, the evolution of the search space and its area relative to the observer must be taken into account. This analysis forms the basis of this thesis. In this work, the search region is characterised through admissible regions.

6.4. Admissible Region

Multiple observations of the same object over a short time interval enable extraction of angular rates through numerical differentiation, yielding the attributable $\mathcal{A}$ [13]. The attributable is a four-dimensional vector combining position and velocity information in the angular measurement space:

$$\mathcal{A} = [\alpha, \delta, \dot{\alpha}, \dot{\delta}] \tag{6.15}$$

For any attributable vector, a corresponding range (ρ) and range-rate ($\dot{\rho}$) value can be used to complete the state. However, for optical observations these values are not measured. Care must be taken in choosing these values as not all possible states correspond to objects that actually exist or are of interest. In the case of this thesis, follow-up observations are desired. Therefore, the selection of range and range-rate combinations must, as accurately as possible, represent the values that best describe the state of the detected Earth-orbiting object.

Following this line of thought, Tommei, Milani, and Rossi [48] introduced the AR. The AR replaces traditional search regions with a strategy that describes possible range and range-rate combinations that fit with a given attributable. Following Milani et al. [30], several requirements are established to generate this region. The AR expresses the limited knowledge regarding the unobserved variables ρ and $\dot{\rho}$, and defines a solution space that is representative of all physically possible states [13].

The AR is defined by physical constraints C that restrict the observed object's state space. The primary constraint requires negative geocentric two-body energy per unit mass, ensuring the object remains in Earth orbit [48]:

$$C_1 = \{(\rho, \dot{\rho}) : \varepsilon_E(\rho, \dot{\rho}) < 0\} \tag{6.16}$$

where [4]:

$$\varepsilon_E(\rho, \dot{\rho}) = \frac{1}{2}||\dot{r}||^2 - \frac{\mu_E}{||r||} \tag{6.17}$$

with $\mu_E = Gm_E$, m_E being the Earth's mass, and r the geocentric position of the object. Additionally, the distance of the object from the observer must be within specified bounds:

$$C_2 = \{(\rho, \dot{\rho}) : \rho_{\text{MIN}} < \rho < \rho_{\text{MAX}}\} \tag{6.18}$$

The specific values of ρ_{MIN} and ρ_{MAX} depend on the orbital regime of interest. Following Tommei, Milani, and Rossi [48], the basic AR is formally defined as:

$$C = C_1 \cap C_2 \tag{6.19}$$

The AR plotted in range-range rate (ρ, $\dot{\rho}$) space may have a complex structure. Tommei, Milani, and Rossi [48] show that the energy constraint C_1 produces either one or two disconnected regions. This behaviour results from analysing a sixth-degree polynomial:

$$V(\rho) := Q^2(\rho)S(\rho) \leq 4\mu_E^2 \tag{6.20}$$

where $S(\rho) = \rho^2 + w_5\rho + w_0$ and $Q(\rho) = w_2\rho^2 + w_3\rho + \gamma$, with the coefficients depending on the observer's geocentric position and velocity, as well as the attributable angles and their time derivatives.

The AR topology varies based on how the range limits ρ_{min} and ρ_{max} intersect with the zero-energy boundary. When the maximum range constraint exceeds all points on the $\epsilon_E = 0$ curve, a single continuous region emerges in (ρ, $\dot{\rho}$) space (Figure 6.3). However, if ρ_{max} lies between two sections of the zero-energy boundary, the AR splits into two distinct regions, each corresponding to different orbital energy regimes (Figure 6.4).

For applications involving SSA and follow-up observations, Fujimoto and Scheeres [13] extends the AR concept with additional physical constraints:

$$C = \bigcap_{i=1}^{4} C_i \tag{6.21}$$

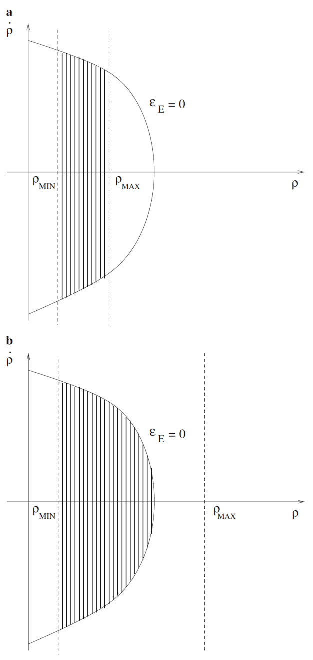

Figure 6.3: AR for an object from optical data (one connected component): $\varepsilon_E = 0$ is the curve of zero geocentric energy, ρ_{MIN} and ρ_{MAX} are the lower and the upper limit for the distance of the object from the observer. Image from [48].

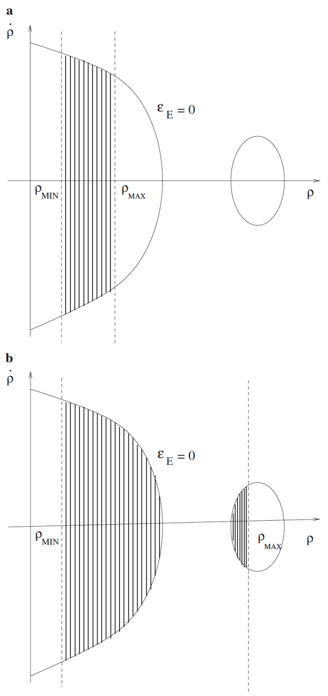

Figure 6.4: AR for an object from optical data (two connected components): $\varepsilon_E = 0$ is the curve of zero geocentric energy, ρ_{MIN} and ρ_{MAX} are the lower and the upper limit for the distance of the object from the observer. Image from [48].

where:

$$C_1 = \{(\rho, \dot{\rho}) : \varepsilon \le 0\} \tag{6.22}$$

$$C_2 = \{(\rho, \dot{\rho}) : 0 \le \rho \le 14 r_E\} \tag{6.23}$$

$$C_3 = \{(\rho, \dot{\rho}) : 1.03 r_E \le r_p\} \tag{6.24}$$

$$C_4 = \{(\rho, \dot{\rho}) : r_a \le 25 r_E\} \tag{6.25}$$

here, ε is the specific geocentric energy, r_p is the perigee radius, and r_a is the apogee radius of the observed object. The C_2 constraint restricts the AR to objects within a sensible range (very few Earth satellites would be at a range of $> 14r_E$). The perigee constraint C_3 ensures the object does not intersect Earth's atmosphere, while the apogee constraint C_4 filters out extreme trans-lunar orbits.

6.4.1. Constrained Admissible Region

Beyond the fundamental energy and range boundaries, the AR can be narrowed by applying known limits on orbital elements. Roscoe et al. [38] develop the CAR approach, which uses fixed values of semi-major axis a and eccentricity e to trace curves through $(\rho, \dot{\rho})$ space. The CAR differs from the basic AR through the application of Keplerian element constraints, which are then translated to the $(\rho, \dot{\rho})$ space.

The CAR formulation combines two physical constraints: the two-body energy relationship and angular momentum conservation. For a specified semi-major axis a, the energy constraint becomes:

$$E = -\frac{\mu}{2a} \tag{6.26}$$

The position and velocity vectors can be expressed using observable parameters $(\alpha, \dot{\alpha}, \delta, \dot{\delta})$ and unobservable parameters $(\rho, \dot{\rho})$. Substituting these into the energy and angular momentum equations produces a system of nonlinear constraint equations. For given values of a and e, solving this system yields corresponding $(\rho, \dot{\rho})$ pairs that satisfy both constraints. These solutions define curves of constant orbital elements within the AR [38]. An example CAR is shown in Figure 6.5.

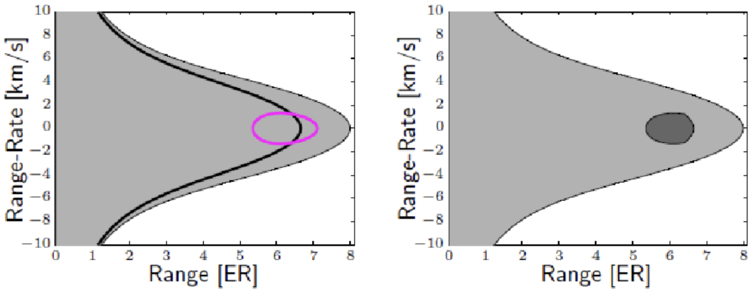

Figure 6.5: Intersection of a given semi-major axis and eccentricity constraint on a GEO AR (Left), and the remaining CAR (right). Image from [23].

The CAR assumes a uniform probability distribution across its bounded region, treating each point as equally likely. However, this approximation has limitations. Some state solutions within the CAR are more physically probable than others based on measurement uncertainties and typical orbital parameter distributions. This motivates a probabilistic extension that weighs different regions of the solution space according to their likelihood.

6.4.2. Probabilistic Admissible Region

The CAR generates deterministic curves in $(\rho, \dot{\rho})$ space for fixed orbital parameters. The PAR builds on this foundation by accounting for uncertainty in both observations and orbital parameters. PAR algorithms aim to derive a better representation of the CAR solution space by incorporating measurement uncertainties and orbital parameter statistics [31, 38].

When analysing objects using angles-only observations, the starting point is the probability density function (pdf) for the measured angles, which is written as $p(\alpha, \delta)$. The observations themselves consist of the object's right ascension and declination, (α, δ). These measurements are used together with a priori information about the object's orbit, specifically its semi-major axis a, eccentricity e, inclination i, and right ascension of the ascending node Ω. This combined data allows for the initial setup of the PAR [31].

The distribution for these orbit parameters is denoted $p(a, e, i, \Omega)$. For simplicity in this initial modelling, it is assumed that these orbit parameters are independent of each other, and also independent of the angle measurements $p(\alpha, \delta)$. This means the complete joint probability distribution covering all six variables can be written by multiplying their individual pdfs together:

$$p(a, e, i, \Omega, \alpha, \delta) = p(a)p(e)p(i)p(\Omega)p(\alpha, \delta) \tag{6.27}$$

The next step involves using constraint equations that link these variables. These equations allow for transforming the joint distribution $p(a, e, i, \Omega, \alpha, \delta)$ to find the desired probability distribution for the object's range and range-rate or even the pdf for the complete state [38].

However, it is impossible to find a simple, direct mathematical formula for this transformation of the uncertainty. This remains true even when the angle measurement errors themselves follow a simple Gaussian distribution. This is because the constraint equations are nonlinear. This nonlinearity prevents the final uncertainty for $(\rho, \dot{\rho})$ from being a simple Gaussian distribution [20].

Therefore, Monte Carlo methods are employed to obtain a particle representation of the uncertainty in $(\rho, \dot{\rho})$ [38]. A visual representation of this can be found in Figure 6.6.

The Monte Carlo procedure can be summarised as follows:

1. Sample from the measurement pdf $p(\alpha, \delta)$ and the orbital parameter pdfs $p(a)$, $p(e)$, $p(i)$, and $p(\Omega)$

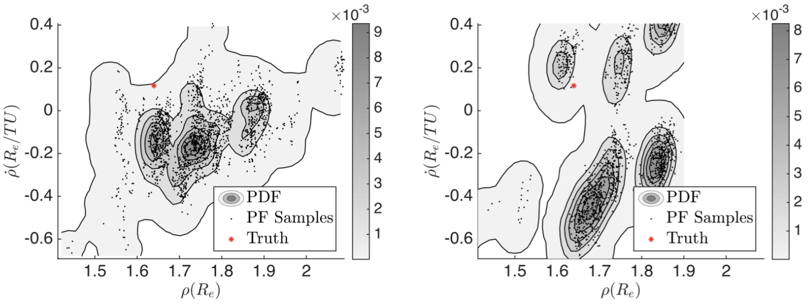

(c) PF$_1$ (d) PF$_2$

Figure 6.6: Two examples of a PAR sampled using (various) PDFs. Image from [55].

2. For each sample $(\alpha, \delta, a, e, i, \Omega)$, solve the nonlinear constraint equations to obtain corresponding values of $(\dot{\alpha}, \dot{\delta}, \rho, \dot{\rho})$
3. The collection of these solutions forms a particle representation of the PAR

While the measurement uncertainty $p(\alpha, \delta)$ is often assumed to be Gaussian, the distributions of orbital parameters $p(a, e, i, \Omega)$ must be specified to complete the PAR formulation. In this work, the orbital parameter distributions are defined through the physical constraints of the CAR (which then produces a uniform distribution) rather than through independent probabilistic models. The uncertainty distribution in $(\rho, \dot{\rho})$ space that results from the nonlinear mapping of these constraints is non-Gaussian and cannot be represented analytically [20]. To enable practical computation and sampling, a GMM is fitted to represent this uncertainty distribution. Following the approach described in Section 6.1, the GMM parameters are estimated using the Expectation-Maximisation algorithm, providing a representation of the PAR that enables Monte Carlo sampling and propagation of the uncertainty distribution.

6.5. Chapter Summary

This chapter established the mathematical framework for orbital state characterisation and the adaptive surveillance methodology. It began by introducing GMMs as a method for modelling orbital populations and generating synthetic datasets from TLE catalogues. The surveillance problem was then defined, describing the dynamic evolution of the uncertainty search set $S(t)$ in state space and its projection $S_{\mathcal{H}}$ into the sensor's measurement space. The chapter's focus was the derivation of AR techniques. The formulation progressed from the AR, which bounds the unobserved range (ρ) and range-rate ($\dot{\rho}$) based on physical energy and range constraints, to the CAR, which refines the solution space by applying known constraints on orbital elements like semi-major axis (a) and eccentricity (e). Finally, the PAR was introduced. The PAR extends the CAR by incorporating measurement and parameter uncertainties, transforming the deterministic CAR boundary into a pdf over the $(\rho, \dot{\rho})$ plane, sampled via Monte Carlo methods. This framework, makes the adaptive follow-up strategy of the "PAR Pipeline" detailed in Chapter 7, possible.

7

Methodology and Software Implementation

This chapter describes the software pipeline developed for evaluating and comparing space surveillance strategies for LEO catalogue generation. The implementation consists of two distinct approaches: a *baseline pipeline* employing three fixed-pattern scanning strategies, and an adaptive *PAR pipeline* that leverages initial detection data to guide subsequent observations. The chapter is organised following the six major steps of the pipeline workflow. A simple overview of the full pipeline can be found in Figure 7.1. All the algorithms that are referred to in the subsequent text can be found in Section 7.8.

7.1. Software Architecture and Implementation

The propagator used in this work is SGP4 (Simplified General Perturbations 4) [50]. This was selected as its design for use with TLEs was critical. SGP4 is an analytical orbit propagation model that takes TLE sets as input, which contain mean orbital elements and a ballistic drag coefficient. The model uses simplified perturbation theory to analytically account for Earth's gravitational harmonics (primarily J2, J3, J4 effects) and atmospheric drag without requiring full numerical integration. To propagate a satellite to a specific time, SGP4 applies analytical equations to update the orbital elements based on the elapsed time and perturbation effects, then computes the satellite's position and velocity vectors.

The surveillance pipeline integrates multiple software components. SPOOK serves as the core simulation engine for optical detection analysis. SPOOK (Special Perturbations Orbit determination and Orbit analysis toolKit) is a sensor simulator developed by Airbus Defence and Space [37] for space surveillance applications. Operating in sensor simulator mode, SPOOK models the complete observation chain from telescope pointing through detection and tracklet generation. The simulator accounts for telescope optical characteristics (aperture, field of view, quantum efficiency), environmental conditions (background brightness, atmospheric effects), and orbital dynamics using SGP4. Regarding object geometry, in this work, SPOOK modelled each object as a perfect sphere with a diameter of 1 metre, and an albedo of 0.1.

SPOOK expects three primary input categories: telescope configuration specifying sensor properties and observer location, satellite catalogue data via TLEs defining target population orbital characteristics, and pointing schedules defining telescope attitude over time. The simulation enforces geometric observability constraints including line-of-sight availability, target solar illumination, sun depression angle, and minimum target elevation. Detection modelling incorporates sensor performance characteristics including read noise, dark current, quantum efficiency, and SNR thresholds.

At each time step, SPOOK propagates all satellites using SGP4, evaluates observability constraints, applies the telescope pointing schedule, simulates the detection process based on sensor performance models, and generates measurements for detected objects.

Simulation outputs include detection statistics (unique satellites detected, observation counts per object), tracking data in TDM (Tracking Data Message) format [1] containing angular measurements suitable for further processing, and coverage analysis quantifying revisit times and detection opportunities. The pipeline executes SPOOK as a subprocess, automatically configuring simulation timing to match observation window parameters and managing execution with timeout monitoring. For each strategy evaluation, the system updates temporal and planning parameters, executes the simulation, and collects output products for subsequent analysis.

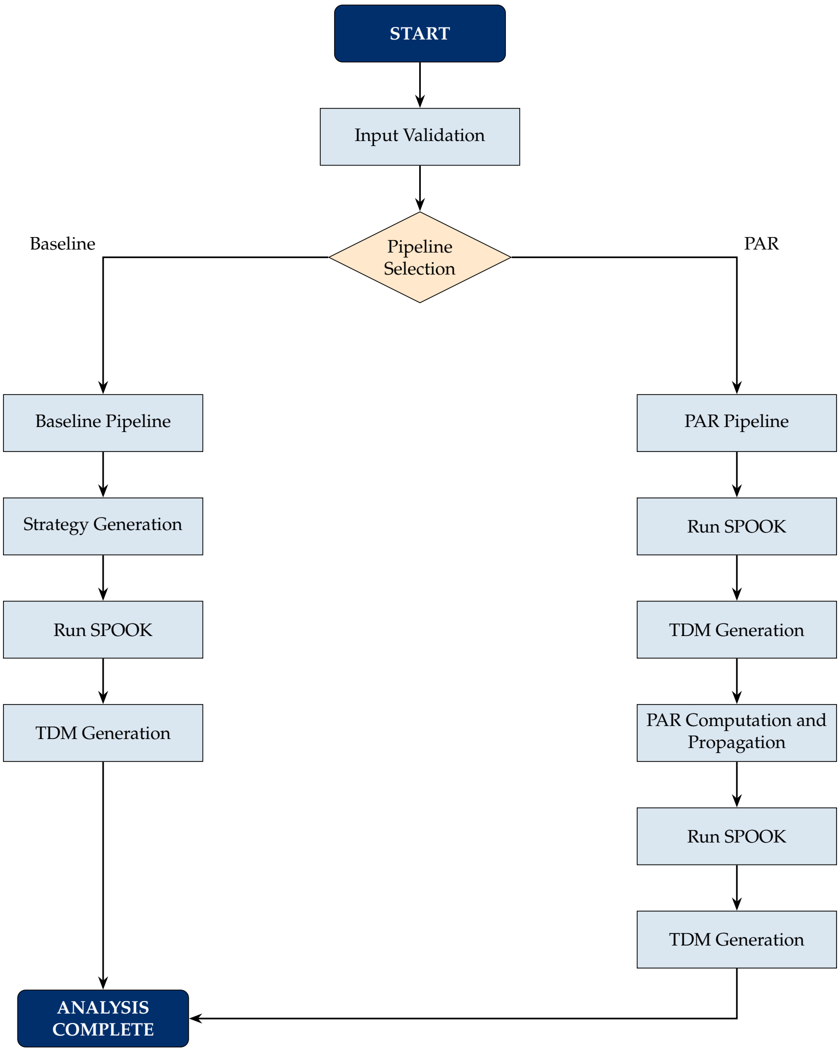

Figure 7.1: Simplified pipeline overview.

7.2. Step 1: Pipeline Initialisation and Input Validation

The pipeline begins with initialisation and validation processes that establish the foundation for both baseline and PAR execution paths. This step implements checks on all inputs and determines which pipeline path to execute based on user configuration. See Figure 7.2.

The system expects three primary input categories:

1. **TLE Files:** TLE sets from Celestrak, Space-Track, or local (synthetic) files
2. **Telescope Configuration:** Observer location, sensor specifications, operational constraints
3. **Surveillance Parameters:** Orbital regime constraints, strategy selection, timing parameters

For the PAR pipeline operations, the CAR requires validated orbital bounds. As described in Subsection 6.4.1, these constraints must satisfy physical requirements: $r_E < a_{min} < a_{max}$ and $0 \leq e_{min} < e_{max} < 1$. Based on configuration flags, the system routes to either baseline or PAR pipeline. Both pipelines share

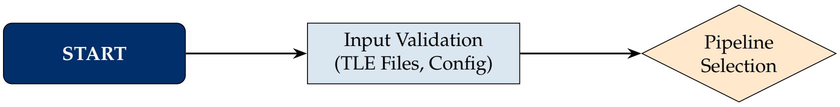

Figure 7.2: Step 1 input validation workflow. The system performs hierarchical validation checks on TLE structural format, orbital element physical bounds, telescope configuration parameters, and temporal consistency. Invalid inputs cause the pipeline to terminate.

common TLE processing and propagation infrastructure, which is initialised during this step regardless of path selection.

7.3. Step 2: Baseline Pipeline - Sky Region Generation

The baseline pipeline's first step generates high-value sky regions by propagating satellites and analysing their spatial-temporal distribution. This step implements two operational modes: synthetic population generation via GMM, or direct propagation of the original set of TLEs. The system supports optional TLE updating from Celestrak repositories. See Figure 7.3. An optional night split mode divides the observation window into two independent periods. If enabled, it calculates:

$$t_{\text{mid}} = t_{\text{start}} + \frac{\Delta t_{\text{night}}}{2}$$

$$\text{Period}_1 = [\, t_{\text{start}},\, t_{\text{mid}} \,]$$

$$\text{Period}_2 = [\, t_{\text{mid}},\, t_{\text{start}} + \Delta t_{\text{night}} \,]$$

Each period executes this step independently, enabling comparison of early-night versus late-night detection efficiency. When direct TLE is enabled, the pipeline propagates the original satellite population without statistical modelling. This mode preserves exact orbital characteristics from TLEs and eliminates GMM fitting. This mode is used for validation and initial code testing (and ART testing). When this is not the case, the system employs GMM (see Section 6.1) to characterise the orbital distribution and generate synthetic populations. See Algorithm 1. The implementation of GMM fitting was done using the *SKLearn* Python package [40]. This package utilises the EM equations described in Section 6.1. The high-value sky regions identified here correspond to projections of the Search region $S_{\mathcal{H}}$ from Chapter 6 into observable RA-Dec coordinates. Regardless of mode selection, the system propagates all satellites using SGP4 implementation. The propagation accounts for perturbations described in Subsection 4.4.2.

For each propagated satellite position at each time step, the system evaluates observability criteria, according to Algorithm 2. Observable positions are aggregated spatially to identify regions with high satellite density. The sky is discretised into a grid according to Algorithm 3. The histogram uses 48×36 bins and SciPy filter methods with kernel size 3. This output serves as input for Step 3.

7.4. Step 3: Baseline Pipeline - Strategy Generation and Execution

Step 3 generates three distinct surveillance strategies in parallel, executes SPOOK simulations (see Section 7.1) for each, and compares their detection performance. All strategies operate on the same sky region database from Step 2, allowing direct comparison. The three baseline scanning patterns are configured with the parameters specified in Table 7.1. These parameters define the geometric characteristics of each scanning strategy. The overlap factor for the grid ensures 10% overlap between adjacent fields to prevent gaps in coverage due to positional uncertainties.

The grid configuration produces a checkerboard pattern covering 0.5 hours in right ascension and 5° in declination per pointing. The declination stripe employs a single 10°-wide strip at constant right ascension. The RA stripe uses a single 1.0-hour-wide strip at constant declination. These configurations remained constant across all simulations for each strategy, enabling direct performance comparison.

Three strategies are generated simultaneously (see Chapter 5):

- `grid`: systematic grid scanning

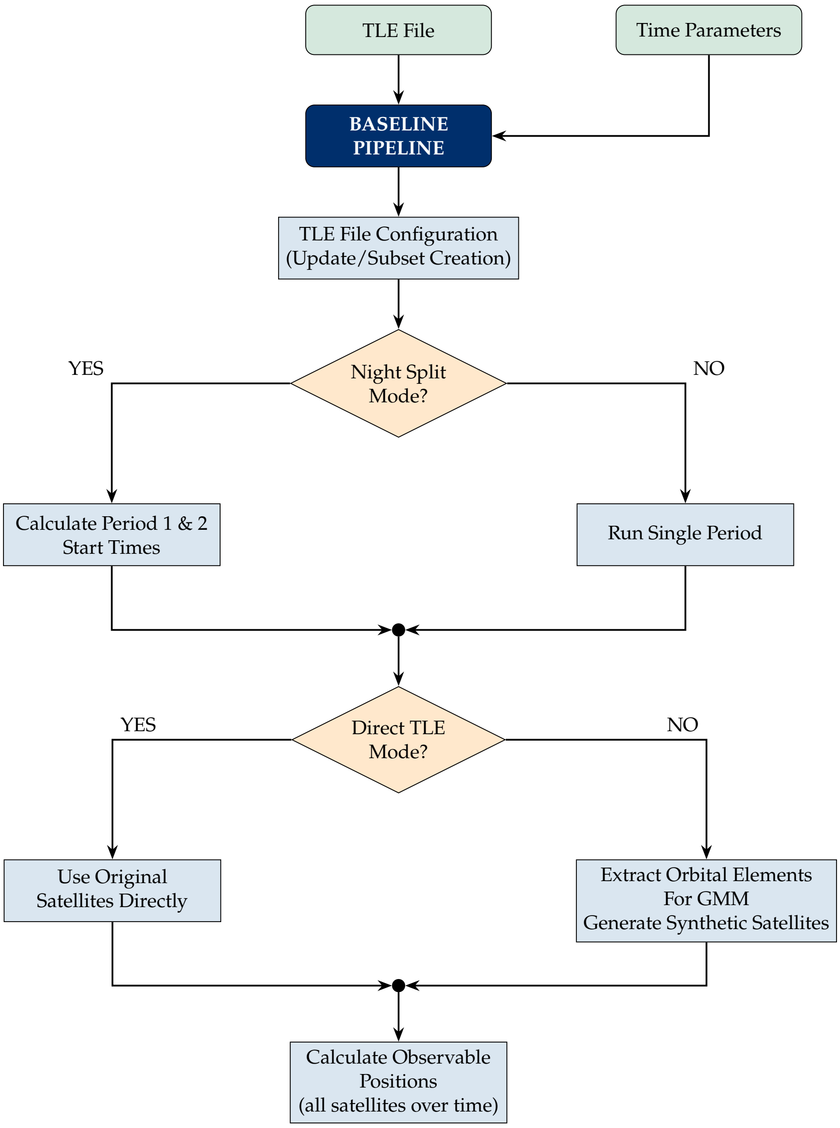

Figure 7.3: Step 2 orbital propagation workflow. TLEs or synthetic orbital elements are propagated throughout the observation window. Each state is transformed to topocentric coordinates and evaluated against observability constraints. Observable positions are aggregated to form the regions of high interest (sky regions).

Table 7.1: Baseline Scanning Pattern Configuration Parameters

Scanning Pattern	Parameter	Value
Grid	RA Width	0.5 hours
	Dec Width	5.0°
	Overlap Factor	0.1
Declination Stripe	Stripe Width	10.0°
	Number of Stripes	1
RA Stripe	Stripe Width	1.0 hours
	Number of Stripes	1

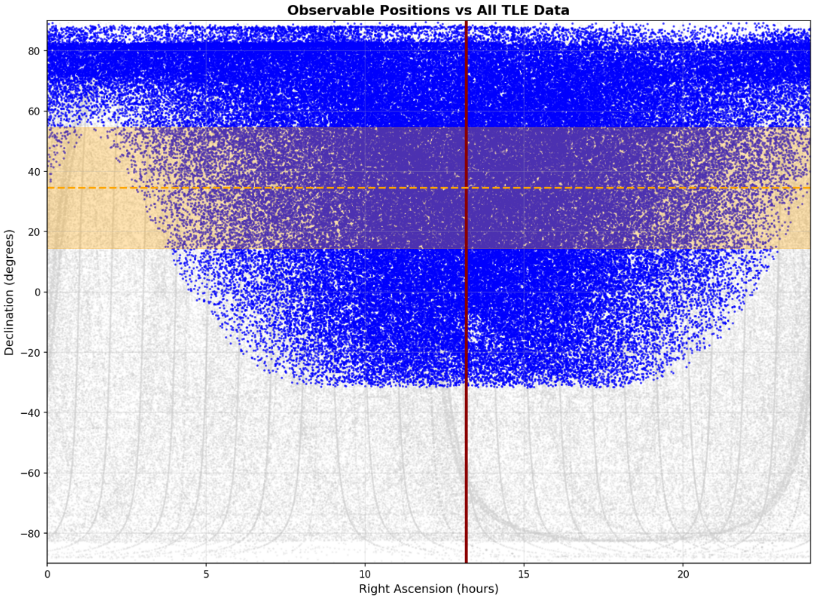

Figure 7.4: Example output for a single declination stripe: grey points are TLE positions, blue points are observable Monte Carlo samples, and the yellow dashed stripe shows the high-value declination. The red line is the high-value right ascension. The yellow highlighted region represents the declination stripe width (the telescope would slew along those values at the fixed right ascension). The input data consisted of all LEO TLEs from SpaceTrack.

- `declination_stripe`: scanning along declinations at fixed right ascension
- `ra_stripe`: scanning along right ascensions at fixed declination

Each strategy loads the high-value regions from Step 2 and generates strategy-specific pointing positions:

- The grid strategy generates pointings covering each region using a uniform spacing with overlap, see Algorithm 4.
- The declination stripe strategy generates pointings along constant right ascension paths with multiple positions per stripe according to Algorithm 5.
- The RA stripe strategy generates pointings along constant declination paths, see Algorithm 6.

Each pointing undergoes observability evaluation, and accessible targets are assigned dwell times, dwell-time is defined as the amount of time the telescope points at a specific pointing. This can be seen in Algorithm 7. The complete pointing schedule is exported to a `.radec` file, see Algorithm 8. The 45-second inter-dwell gap simulates telescope slewing and settling. Each strategy's `.radec` file is executed through SPOOK simulation, producing outputs for Step 6 analysis. An example declination stripe simulation output is shown in Figure 7.4.

The strategies described in Steps 2-3 represent the baseline approach, where telescope pointings are determined by predicted satellite distributions without feedback from actual detections. In contrast, the PAR pipeline introduced in Steps 4-5 implements an adaptive strategy that uses initial detection information to guide follow-up observations, simulating catalogue generation operations.

7.5. Step 4: PAR Pipeline - Direct Satellite Tracking (Phase 1)

The PAR pipeline diverges from the baseline approach by implementing a two-phase strategy designed to simulate a realistic detection and follow-up scenario. In an operational setting, the workflow would proceed as follows: an initial detection of a previously untracked object is made, the CAR/PAR is formulated based on this detection, and multiple follow-up observation are then scheduled to re-detect the object. To replicate this scenario in this test environment, Phase 1 tracks catalogued satellites solely for the purpose of generating synthetic initial detections, which Phase 2 then uses to guide follow-up observations as if these were real uncatalogued targets. Phase 1 operates differently from the baseline

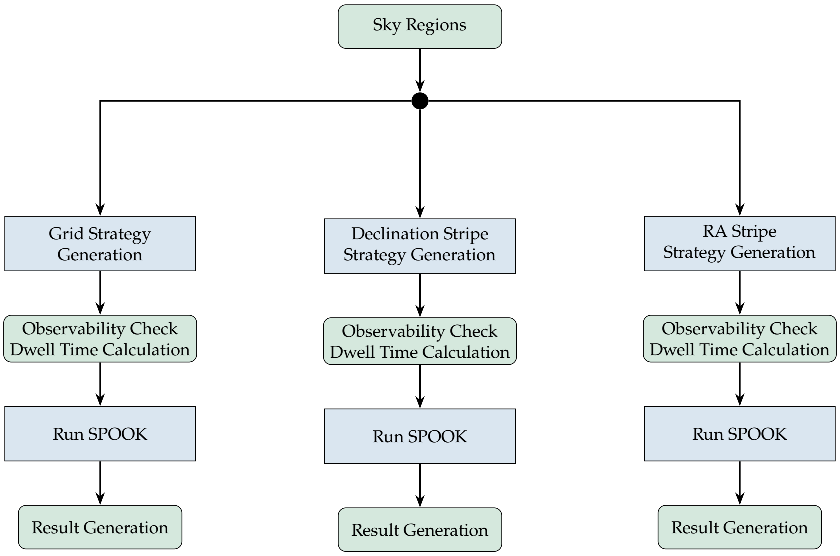

Figure 7.5: Step 3 parallel strategy generation. With observability checks including dwell time calculation as input for SPOOK for result generation.

pipeline's statistical sky region approach. Rather than identifying high-density regions, it prioritises acquiring individual tracklets from known satellites to produce the initial detection data required for subsequent CAR/PAR construction (see Figure 7.6). In practice, these initial detections would come from survey observations of unknown objects (using e.g. one of the used baseline strategies). Phase 1 loads satellites from the input TLE file and generates a satellite tracking strategy. For each satellite, the system identifies observability windows using the same observability constraints as in Step 2. However, instead of aggregating positions into sky regions, Phase 1 selects one optimal observation window per satellite to simulate a single initial detection event. The algorithm for Phase 1 can be seen in Algorithm 9. The pointing schedule is exported to a `.radec` file using the same format as Step 3, with entries generated for each second of the dwell time and 45-second inter-observation gaps for telescope slewing. The schedule is then executed through SPOOK simulation. SPOOK generates TDM files containing the optical tracklets for each detected satellite (see Section 7.1 for more details). These TDM files serve as the foundation for Phase 2.

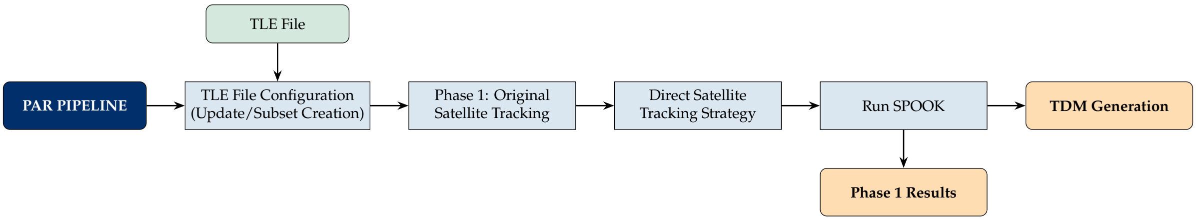

Figure 7.6: PAR Phase 1 direct satellite tracking strategy. TLE input as in previous steps, followed by pointing generation tracking observable satellite positions directly.

7.6. Step 5: PAR Pipeline - Real-Time Observations (Phase 2)

Phase 2 implements the PAR pipeline's adaptive surveillance strategy by processing Phase 1 TDM files to construct PARs and schedule follow-up observations. See Figure 7.7.

The system begins by grouping Phase 1 TDM files by satellite, extracting NORAD catalogue IDs and satellite names from each file. For each satellite group, the latest observation epoch across all TDM files determines the reference time. A processing delay is added to schedule follow-ups with a sufficient temporal gap, in order to provide meaningful secondary observations according to Algorithm 10. Figure 7.8 illustrates the AR constructed from a Phase 1 tracklet, showing the bounded region in range-range-rate space satisfying energy, orbital element, and observability constraints. This AR is used

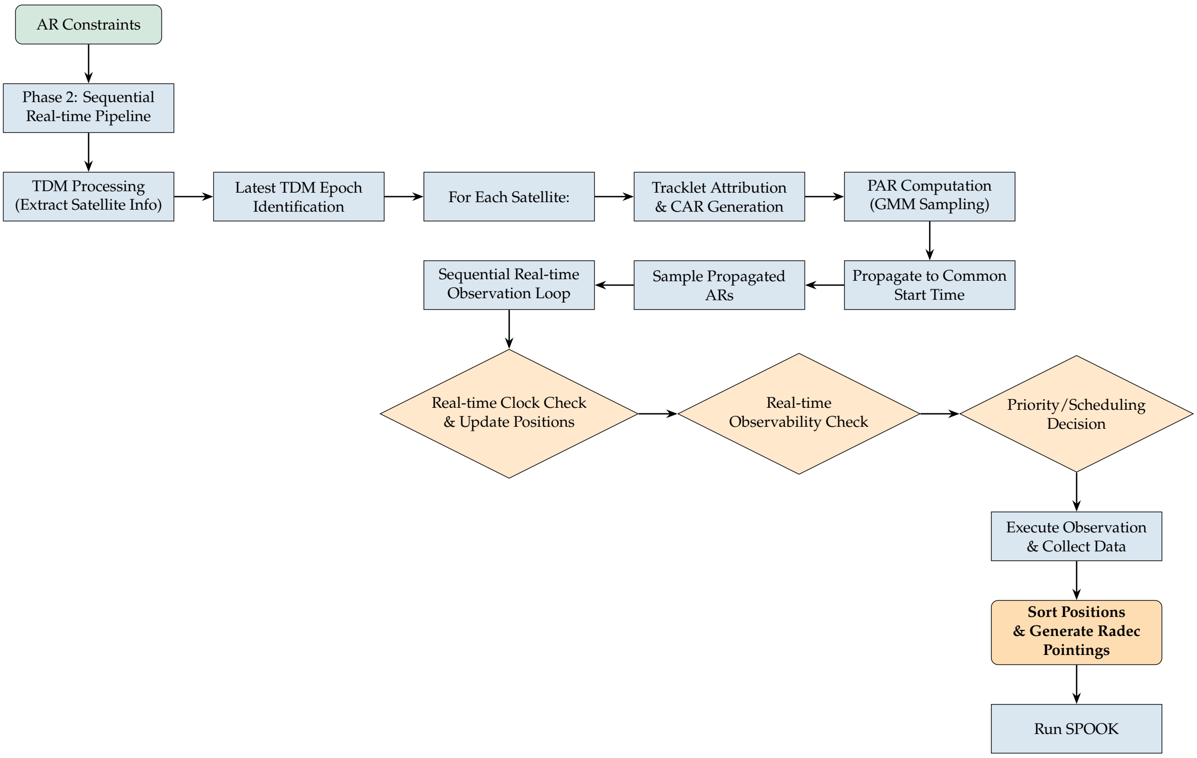

Figure 7.7: Phase 2 sequential observation workflow. TDM files from Phase 1 are processed to extract attributables, construct CARs, compute PARs via GMM sampling, propagate to a common start time, and dynamically schedule observations based on real-time accessibility.

to generate the PAR using GMM. From the fitted GMM samples are drawn which are propagated to the reference time + temporal gap. Once this is done for all phase 1-generated TDMs, samples are drawn uniformly per propagated PAR. These few samples represent the satellites likely state at a certain point in time. These states are propagated throughout the observation window.

The observation window extends from the start time to either the planned duration or a cutoff time (default 06:00 local time), whichever occurs first. This is to simulate a single observation night (in principle multiple nights could be simulated too). The scheduler operates in real-time, propagating all PAR samples forward and evaluating accessibility at each decision epoch. See Algorithm 11. The scheduler prioritises samples by elevation (favouring higher elevations for better detection), then by sky position to maintain systematic coverage. Each selected sample is observed once, and the system advances by the dwell time plus a 5-second slew duration. This 5-second slew is less than the 45-seconds applied earlier, the reasoning behind this is the close proximity of the pointings in Phase 2 compared to Phase 1. The loop continues until the cutoff time or all samples are observed. For Phase 2, dwell time depends on the angular rate at which the satellite traverses the telescope's FoV, ensuring the target remains observable throughout the exposure, see Algorithm 12. The pointing schedule is exported and converted to the `.radec` format for SPOOK execution, following the same process as Phase 1.

This produces a certain observation pattern. An example is shown in Figure 7.9. When multiple samples become accessible in the same region simultaneously, the scheduler observes them before moving elsewhere. The tight grouping of early observations in this example (0–15) around RA 0–5h occurs because those sampled were all accessible at the same time. Later observations spread out as samples moved or different regions became accessible. Each satellite contributes up to $N_{samples}$-observations, fewer if samples never satisfy observability constraints during the window.

Phase 2 SPOOK execution generates detection statistics and TDMs, enabling quantitative assessment of the adaptive PAR strategy versus baseline catalogue tracking.

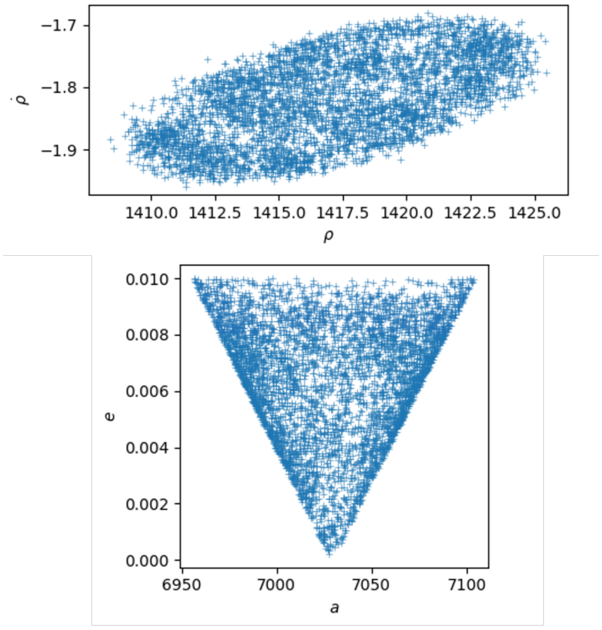

Figure 7.8: Example AR constructed from Phase 1 TDM shown in two parameter spaces. Top: range (ρ) versus range-rate ($\dot{\rho}$) space showing the AR bounded by physical constraints. Bottom: semi-major axis (a) versus eccentricity (e) space showing the triangular constraint region satisfying LEO orbital bounds.

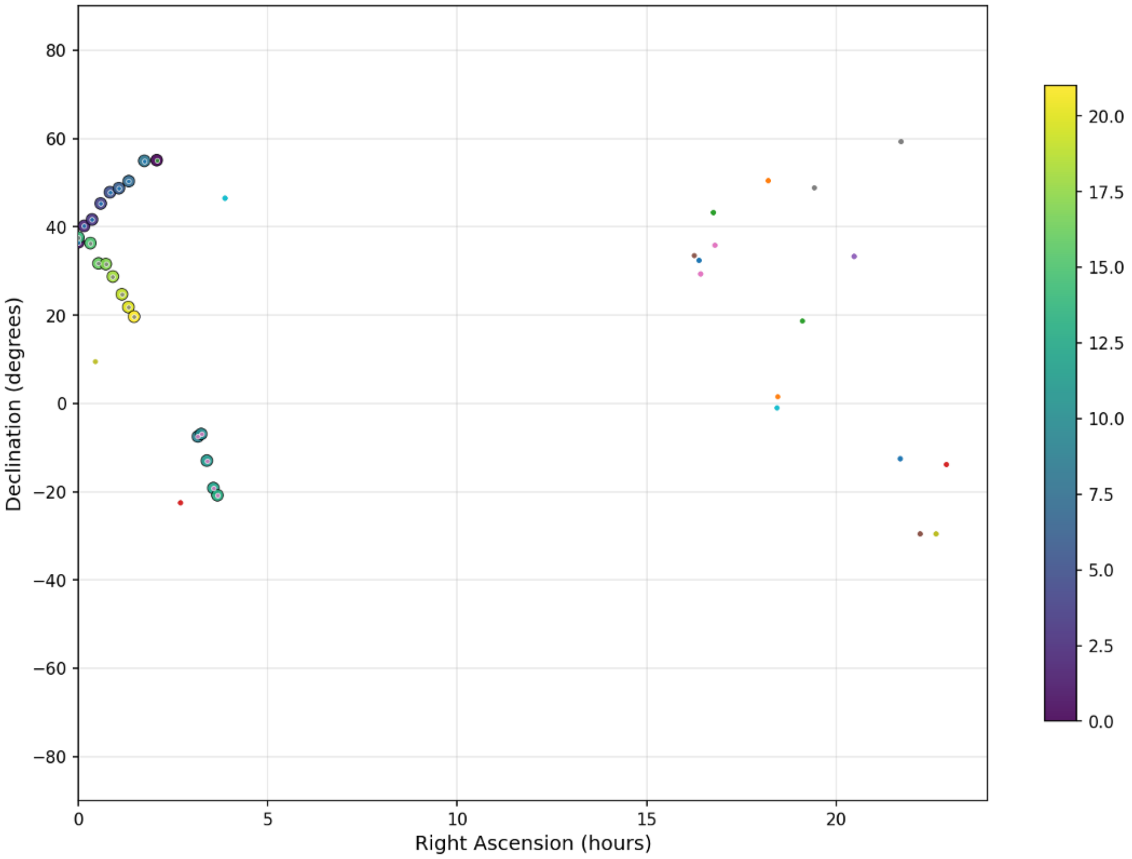

Figure 7.9: Phase 2 observation sequence. Small points: PAR samples (3 per satellite in this example) at observation start time. Large circles: pointings coloured by sequence (0–22).

7.7. Step 6: Results Analysis and Strategy Comparison

The final step runs SPOOK, generates results, and possibly generates pointings for ART telescope observations. See Figure 7.10.

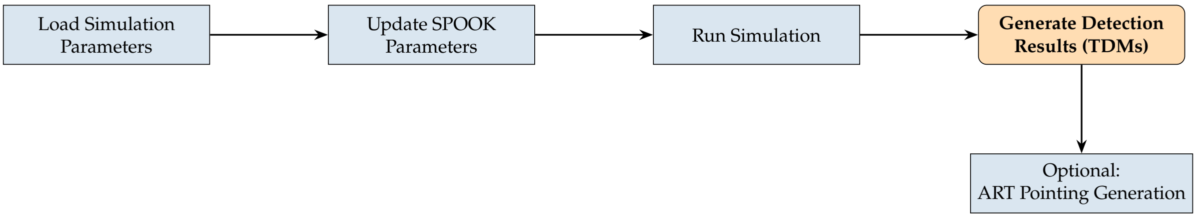

Figure 7.10: Step 6 SPOOK execution and results processing workflow. Simulation parameters are loaded, SPOOK parameters updated, simulation executed, and detection results (TDMs) generated. Optional ART pointing generation converts results to telescope-ready observation plans.

Figure 7.11 illustrates the analysis framework comparing telescope pointings, actual detections, and TLE truth trajectories across both PAR phases. Detection statistics are extracted from SPOOK outputs, including total detections, crossings and unique detections/crossings. The system computes detection efficiency (ratio of detected to accessible satellites), coverage efficiency (productive pointings per total pointings), and statistical distributions of observations per satellite. Having established SPOOK's prediction accuracy and the validity of the simulation framework, the following chapter presents the comparative performance results that address the research questions formulated in Chapter 3.

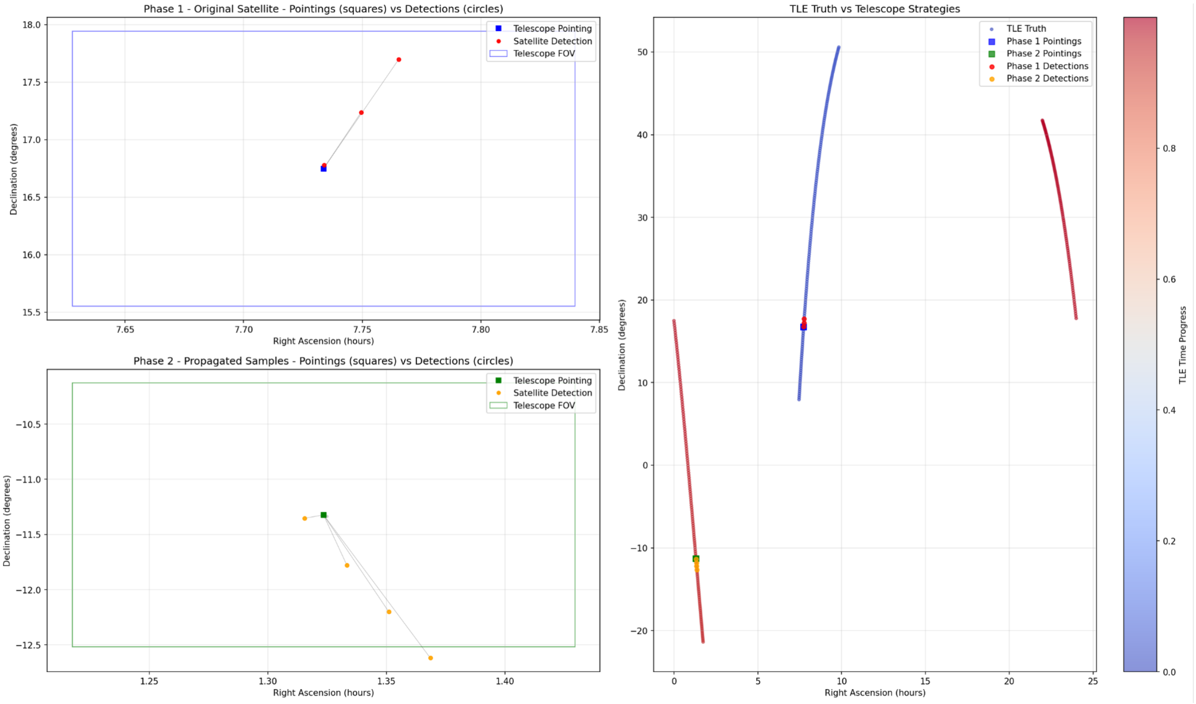

Figure 7.11: Example TDM analysis comparing telescope pointings versus detections versus TLE truth. Left panels show Phase 1 (top) and Phase 2 (bottom) pointings (squares) and successful detections (circles) with telescope field of view overlays. Right panel displays the full orbital trajectory from TLE truth (red line) with Phase 1 pointings (blue squares), Phase 2 pointings (green squares), and corresponding detections (filled circles). NOTE: the FoV outline is for visualisation purposes, and not rotated which is what SPOOK actually simulates.

7.8. Algorithms

Algorithm 1 GMM-Based Sky Region Generation

```
Require: TLEs, number of $K$ components, number of $N_{synthetic}$ synthetic satellites
Ensure: Synthetic satellite population
Extract orbital elements $(a, e, i, \Omega, \omega)$ from TLEs
Preprocess angular variables to handle wraparound at $0°/360°$
Fit GMM using EM algorithm    ▷ See Equation 6.1 - 6.2, and Equation 6.4 - 6.7
for $n = 1$ to $N_{\text{synthetic}}$ do
    Select component $k$ with probability $P(k = j) = \pi_j$
    Sample orbital elements $\mathbf{x} \sim \mathcal{N}(\boldsymbol{\mu}_k, \boldsymbol{\Sigma}_k)$
    Sample true anomaly $\theta \sim \mathcal{U}(0, 2\pi)$
    if orbital elements violate physical constraints then
        Reject sample and resample
    end if
end for
return Synthetic satellite population
```

Algorithm 2 Observability Check

```
Require: Satellite state $\mathbf{x}(t)$, observer parameters, minimum sun, elevation and moon separation angles
Ensure: Boolean: True if observable, False otherwise
Compute sun altitude $h_\odot$ at observer
if $h_\odot > h_{\odot,\text{min}}$ then    ▷ Sun too high: not in twilight
    return False
end if
Transform $\mathbf{x}(t)$ to topocentric coordinates
Compute topocentric elevation $El$
if $El < El_{\text{min}}$ then    ▷ Below horizon or minimum elevation
    return False
end if
Compute moon angular separation $\Delta\theta_{\text{moon}}$
if $\Delta\theta_{\text{moon}} < \Delta\theta_{\text{moon,min}}$ then    ▷ Too close to moon
    return False
end if
return True    ▷ All constraints satisfied
```

Algorithm 3 Sky Region Identification from Observable Positions

```
Require: Observable objects $\{(\text{RA}_i, \text{Dec}_i, \text{El}_i, \text{satellite}_i, t_i)\}$, histogram bin counts, proximity thresholds,
    minimum objects $N_{\text{min}}$, $n_{\text{stripes}}$
Ensure: High-value sky regions
Build 2D histogram of RA vs Dec
Apply local maximum filter to identify peaks
for each peak do
    Count nearby objects within proximity thresholds
    if count $\geq N_{\text{min}}$ then
        Compute info score: density × mean elevation
        Append region to high-value list
    end if
end for
Sort regions by info score (descending)
return top $n_{\text{stripes}}$ regions
```

Algorithm 4 Grid Generation

```
Require: High-value regions, FoV dimensions, overlap factor $f_{\text{overlap}}$
Ensure: Grid pointing list
Compute effective spacing:
    $\Delta\alpha = w_{\text{FoV},\alpha} \cdot (1 - f_{\text{overlap}})$
    $\Delta\delta = w_{\text{FoV},\delta} \cdot (1 - f_{\text{overlap}})$
Initialise empty pointing list $\mathcal{P}$
for each region $R$ in high-value regions do
    Determine grid bounds: $[\alpha_{\min}, \alpha_{\max}], [\delta_{\min}, \delta_{\max}]$
    Compute number of RA and Dec bins using effective spacing
    for each $(\alpha_i, \delta_j)$ in RA × Dec bins do
        Add $(\alpha_i, \delta_j)$ to $\mathcal{P}$
    end for
end for
return $\mathcal{P}$
```

Algorithm 5 Declination Stripe Generation

```
Require: High-value regions, stripe width, Telescope config
Ensure: Stripe pointing list
for each high-value region $R$ do
    Determine declination centre $\delta_c$ and RA centre $\alpha_c$
    Compute number of positions along declination using FoV and overlap from telescope config
    for each declination position $\delta_i$ do
        Add pointing $(\alpha_c, \delta_i)$ to list
    end for
end for
return Stripe pointing list
```

Algorithm 6 RA Stripe Generation

```
Require: High-value regions, stripe width (hours), Telescope config
Ensure: Stripe pointing list
for each high-value region $R$ do
    Determine RA centre $\alpha_c$ and Dec centre $\delta_c$
    Compute number of positions along RA using FoV and overlap from telescope config
    for each RA position $\alpha_i$ do
        Add pointing $(\alpha_i, \delta_c)$ to list
    end for
end for
return Stripe pointing list
```

Algorithm 7 Static Dwell Time Calculation

```
Require: Exposure time $t_{\text{exp}}$, number of exposures $N_{\text{exp}}$, readout time $t_{\text{read}}$
Ensure: Total dwell time $t_{\text{dwell}}$
$t_{\text{dwell}} = t_{\text{exp}} \cdot N_{\text{exp}} + t_{\text{read}} \cdot (N_{\text{exp}} - 1)$
Apply bounds: $t_{\text{dwell}} = \max(15\,\text{s}, \min(t_{\text{dwell}}, 300\,\text{s}))$
return $t_{\text{dwell}}$
```

Algorithm 8 Generate .radec File

```
Require: Accessible pointing list with dwell times
Ensure: Time-stamped .radec file
$t_{\text{current}} \leftarrow t_{\text{start}}$
for each target $(\alpha, \delta, t_{\text{dwell}})$ do
    for $t$ from $t_{\text{current}}$ to $t_{\text{current}} + t_{\text{dwell}}$ in 1s steps do
        Write entry
    end for
    $t_{\text{current}} \leftarrow t_{\text{current}} + t_{\text{dwell}} + t_{\text{slew}}$        ▷ $t_{\text{slew}}$ = 45s for baseline
end for
```

Algorithm 9 Phase 1 Satellite Tracking Strategy

```
Require: TLE file, observation window parameters, telescope configuration
Ensure: Satellite tracking schedule with dwell times
Load satellites from TLE file using SGP4
Initialise empty pointing schedule $\mathcal{S}$
$t_{\text{current}} \leftarrow t_{\text{start}}$
for each satellite in TLE file do
    Propagate satellite using SGP4 over observation window
    Find observable windows using constraints from Section 7.3
    if observable windows exist then
        Select best window: highest elevation, earliest time
        Extract coordinates $(\alpha, \delta, t_{\text{obs}}, El)$
        Calculate dwell time using Algorithm 7
        Create pointing: $(\alpha, \delta, t_{\text{obs}}, t_{\text{dwell}}, \text{sat\_id})$
        Add pointing to $\mathcal{S}$
        $t_{\text{current}} \leftarrow t_{\text{current}} + t_{\text{dwell}} + 45\,\text{s}$
    end if
end for
Sort $\mathcal{S}$ by observation time
return $\mathcal{S}$
```

Algorithm 10 Phase 2 TDM Processing and PAR Generation

```
Require: Phase 1 TDM, orbital constraints, processing delay $\Delta t_{\text{proc}}$, $N_{samples}$ number of PAR samples
Ensure: PAR sample clouds for all satellites
Group TDM files by satellite (NORAD ID)
Identify latest epoch: $t_{\text{latest}}$ = max(all TDM epochs)
Compute start time: $t_{\text{start}} = t_{\text{latest}} + \Delta t_{\text{proc}}$
for each satellite group do
    Read TDM and compute attributable
    Create CAR with constraints: $a_{\text{min}}, a_{\text{max}}, e_{\text{min}}, e_{\text{max}}$ (see Subsection 6.4.1)
    Generate PAR at TDM epoch using GMM (see Section 6.1):
      Sample $N_{\text{GMM}}$ = 10,000 samples from fitted GMM
      Retain samples within CAR boundaries
    Propagate PAR from TDM epoch to $t_{\text{start}}$ using J2
    Sample PAR uniformly: draw $N_{\text{samples}}$ states
    Store state
end for
return All PAR sample states
```

Algorithm 11 Sequential Real-Time Observation Scheduler

```
Require: PAR sample states, $t_{\text{start}}$, $t_{\text{cutoff}}$, telescope configuration
Ensure: Pointing schedule
$t_{\text{current}} \leftarrow t_{\text{start}}$
Initialise unobserved samples $\mathcal{U}$ = all PAR samples
Initialise schedule $\mathcal{S} = \emptyset$
while $t_{\text{current}} < t_{\text{cutoff}}$ and $\mathcal{U} \neq \emptyset$ do
    Propagate samples in $\mathcal{U}$ to $t_{\text{current}}$
    Transform to topocentric coordinates
    Evaluate accessibility for each sample (constraints from Section 7.3)
    Filter accessible samples: $\mathcal{A} = \{s \in \mathcal{U} : s \text{ is accessible}\}$
    if $\mathcal{A} = \emptyset$ then
        $t_{\text{current}} \leftarrow t_{\text{current}} + 60\,\text{s}$        ▷ No targets, advance
        continue
    end if
    Sort $\mathcal{A}$: elevation (descending), then RA, then Dec
    Extract $(\alpha, \delta, El)$ from $\mathcal{A}$
    Calculate dwell time using Algorithm 12
    Create pointing: $(\alpha, \delta, t_{\text{current}}, t_{\text{dwell}}, \text{sat\_id})$
    Add pointing to $\mathcal{S}$
    Remove pointing from $\mathcal{U}$        ▷ Mark as observed
    $t_{\text{current}} \leftarrow t_{\text{current}} + t_{\text{dwell}} + t_{\text{slew,PAR}}$        ▷ $t_{\text{slew,PAR}} = 5\text{s}$
end while
return $\mathcal{S}$
```

Algorithm 12 Angular Rate-Based Dwell Time Calculation

```
Require: Satellite state (position, velocity), FoV dimensions $w_{\text{FoV},\alpha}$, $w_{\text{FoV},\delta}$
Ensure: Dwell time $t_{\text{dwell}}$
Transform satellite state to topocentric frame
Compute angular rates from velocity vector:
    $\dot{\alpha}$ = RA rate (rad/s)
    $\dot{\delta}$ = Dec rate (rad/s)
Compute traversal times:
    $t_\alpha = w_{\text{FoV},\alpha} / |\dot{\alpha}|$
    $t_\delta = w_{\text{FoV},\delta} / |\dot{\delta}|$
$t_{\text{dwell}} = \min(t_\alpha, t_\delta)$
return $t_{\text{dwell}}$
```

8

Verification and Validation

This chapter validates the PAR pipeline's observation planning algorithms and SPOOK's optical performance model through comparison against real ART observations during September 2025. The validation campaign considered 73 unique satellites (54 LEO, 19 MEO) from sun-synchronous and GPS/Galileo orbits. The PAR pipeline generated an observation plan based on simulated visibility and geometry constraints, and TLEs as an input, as explained in Chapter 7. The observation plan tasked both SPOOK and ART. ART executed 142 observations during the campaign period, while SPOOK executed 110 observations. The validation establishes the reliability of the simulation framework used to generate the results presented in Chapter 9. An illustration of the entire validation workflow can be found in Figure 8.1.

The validation employs a three-tier approach. First, SGP4-propagated positions, using TLEs as input for the observation plans, are compared against ART observations to filter detections from non-target objects that might have passed through the FoV, and to identify which TLEs are accurate enough for subsequent analysis. Second, validated ART detections of target satellites are cross-referenced with SPOOK observations to quantify pipeline accuracy. Third, TDM-to-TDM (generated both by SPOOK and ART) comparison is done at exact measurement epochs for successfully matched pairs. The angular separation threshold of 200 arcseconds defines the correlation criterion throughout this validation. This threshold corresponds to expected SGP4 accuracy for same-day orbital elements, typically representing 0.5-1 km position errors at LEO altitudes [51, 24].

8.1. SGP4-ART Validation

The first validation step filters target-object detections from non-target objects that might have crossed ART's FoV and establishes which ART observations have sufficiently accurate TLEs to use as baseline for subsequent pipeline comparison. For each of the 142 ART observations, identified by NORAD ID in the observation metadata (assigned during telescope tasking), the corresponding TLE from the 73-satellite target catalogue is propagated to the observation epoch using SGP4. The predicted position (sky coordinate) is compared to the actual ART detection position. If the angular separation is within 200 arcseconds, the TLE is considered accurate enough for subsequent validation steps and the detection is confirmed as a targeted satellite rather than a non-targeted object. This filtering is necessary because some TLEs degrade rapidly due to outdated epochs, unmodelled manoeuvres, or orbital perturbations beyond SGP4's analytical capability, and because ART detects non-target satellites passing through its field of view during scheduled observations.

Applying SGP4 propagation with the 200 arcsecond threshold to all 142 ART observations yields 71 validated target detections, representing 50% of the observation sample. This validation rate establishes the set of target satellites successfully observed during the campaign. The 71 observations that failed SGP4 validation represent predominantly detections of satellites outside the 73 non-targeted satellite, as well as observations where TLEs were outdated at the observation epoch or satellites with orbital perturbations exceeding SGP4 model accuracy, or false detections.

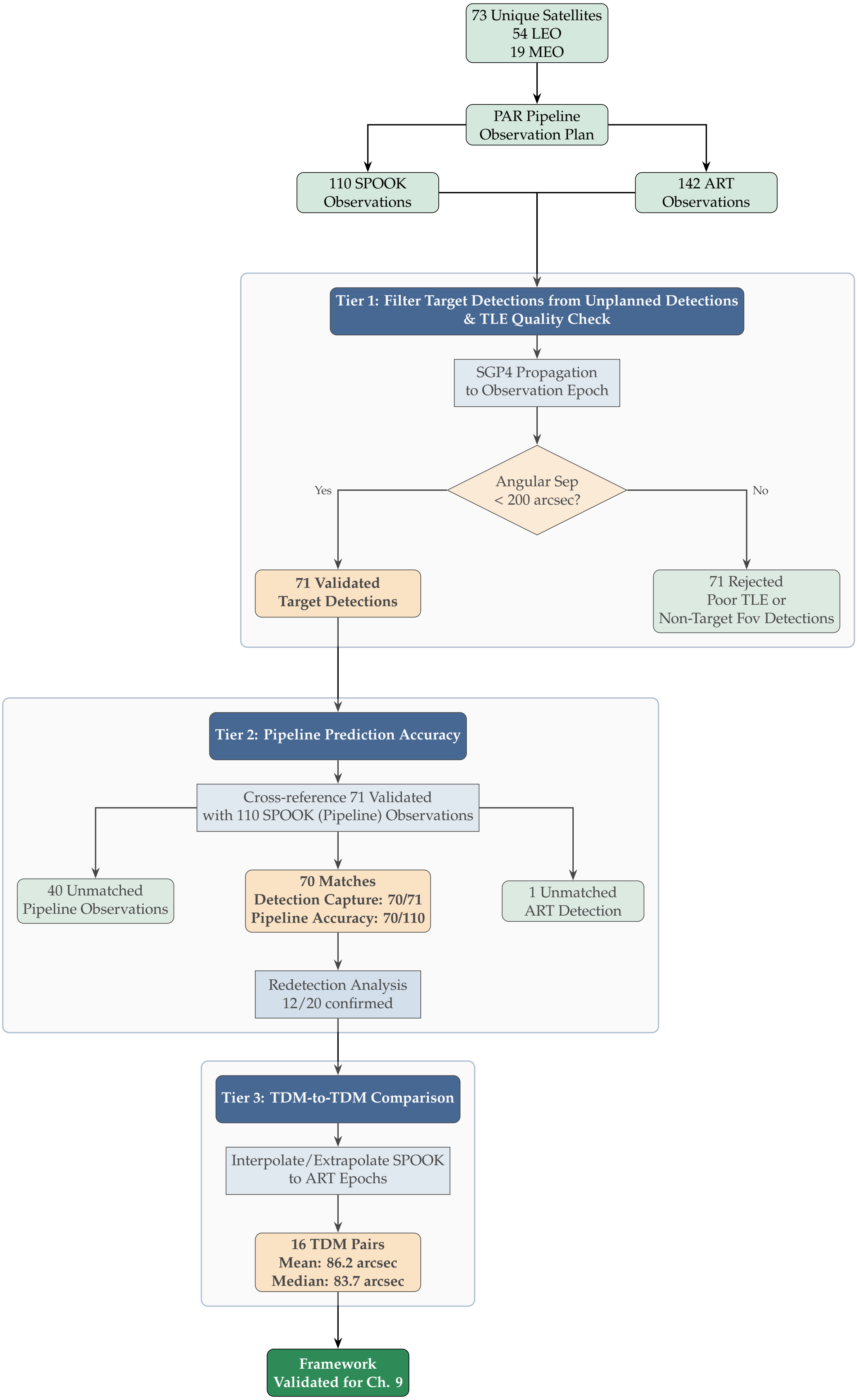

Figure 8.1: Three-tier validation framework.

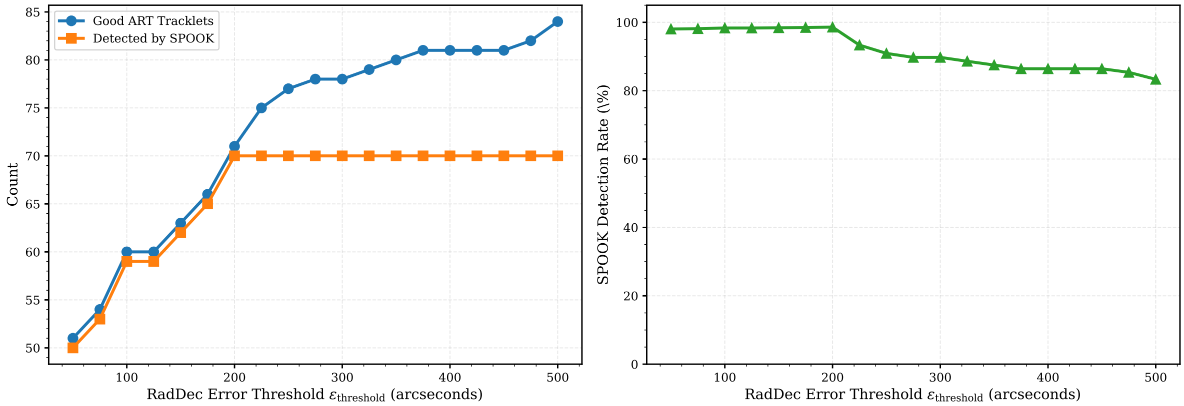

Figure 8.2: Validation of angular threshold. Left plot shows drop-off of any new pipeline-TLE correlations after the 200 arcsecond point in absolute numbers. Right plot shows the same in percentages.

8.2. Pipeline Accuracy

The second validation step quantifies the PAR pipeline's accuracy by comparing its 110 observations generated by SPOOK against the 71 validated ART detections established in the previous section. A match is defined as a SPOOK observation and validated ART detection for the same NORAD ID. The NORAD ID comes from the input TLEs and is used in the naming of the task scheduled both for SPOOK and ART, allowing for comparisons.

Cross-referencing the 71 validated ART detections against SPOOK observations yields 70 matches. From the ART perspective, the pipeline correctly predicted 70 of 71 observations successfully observed by ART. This 98.6% detection capture rate demonstrates that when ART observes a target satellite with good TLE quality, the pipeline almost always predicted that observation. From the pipeline perspective, 70 of 110 observations were confirmed by ART observations, representing 63.6% accuracy. The pipeline accuracy quantifies how often SPOOK (and therefore the pipeline) observations prove correct when compared against actual telescope observations.

The 40 unmatched observations represent satellites below ART's detection capability, observations during cloud cover or unfavourable atmospheric conditions, or observations at low elevation angles with excessive atmospheric refraction.

The 1 validated ART detection without corresponding SPOOK observation represents a target satellite that was included in the generated observation plan, successfully observed by ART with validated SGP4 propagation, but not observed by SPOOK despite being generated in the pipeline's observation plan. This shows a mismatch between SPOOK and reality. Possible explanations include algorithm gaps where visibility constraints caused an incorrect rejection of these passes or temporal boundary effects where observation at accessibility window edges were filtered by temporal constraints.

Figure 8.2 validates the angular separation threshold. The left plot displays the cumulative number of ART/TLE correlations as the angular threshold increases, as well as a line that represents if that correlated TLE was detected by SPOOK. The plateau after 200 arcseconds indicates that increasing the threshold beyond this point produces no additional valid correlations, confirming that 200 arcseconds captures all legitimate matches. The right plot presents the same data in percentage form. The starting gap between ART and SPOOK observations is the 1 ART detection that has no SPOOK counterpart.

Breaking down the 70 successful correlations by orbital regime yields 43 LEO matches and 27 MEO matches. The predominantly LEO validation sample reflects the observing campaign's focus on low Earth orbit targets. The MEO correlation was done for testing and comparison purposes before moving on to LEO.

Figure 8.3 presents the error statistics for the ART detections compared to SGP4. The top left plot shows the error distributions for both RA and Dec centre near zero, indicating no pointing bias in either coordinate. The roughly Gaussian error distribution suggests random propagation uncertainties dominate over systematic errors. Mean angular separation across all matches is 40.53 arcseconds and standard deviation 61.18 arcseconds. This mean error lies well within expected SGP4 performance for same-day TLE propagation, where 1-3 km position errors translate to approximately 150-250 arcseconds at typical LEO altitudes [24]. The top right plot shows that the direction of the RA and Dec errors is uncorrelated, as indicated by the symmetric scatter across all quadrants. However, the magnitude of both errors shows a linear relationship. The bottom left plot displays practically no (or very weak) correlation between propagation time and position error, indicating TLE quality hardly impacts prediction accuracy within the same-day propagation timeframe of this dataset. This indicates that the 71 unmatched ART observations are due to non-target objects passing through the FoV during exposures. The bottom right plot shows the same data as the bottom left plot with error bars representing standard deviation across multiple measurements within each tracklet, demonstrating measurement consistency for most satellites (note the logarithmic axis).

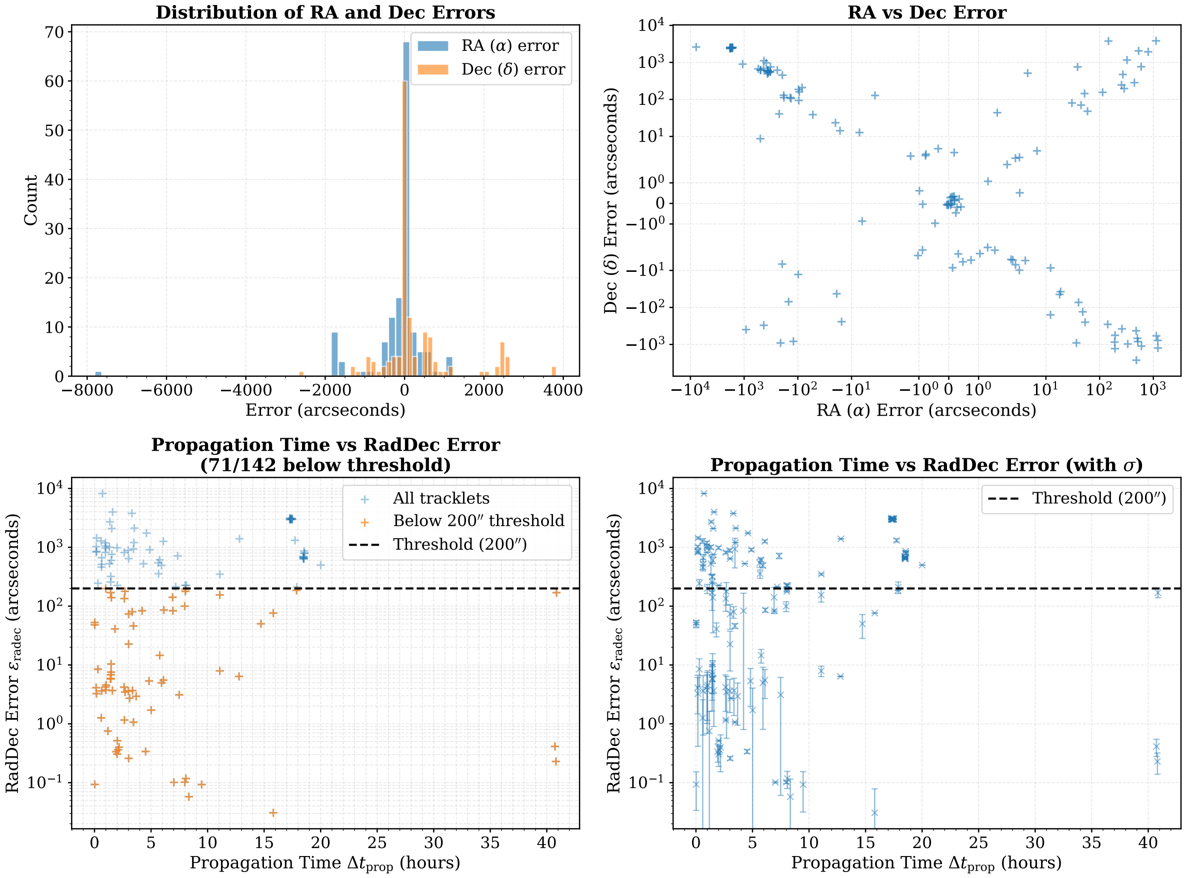

Figure 8.3: Error analysis ART-SGP4. Top left plot shows distribution of RA and Dec errors with near-zero mean and near-symmetric spread. The top right plot shows that the direction of the RA and Dec errors is uncorrelated, as indicated by the symmetric scatter across all quadrants. However, the magnitude of both errors shows a linear relationship. Bottom left plot displays very weak correlation between propagation time and position error, indicating TLE age effects are minimal. Bottom right plot shows the same data as the bottom left plot with error bars representing standard deviation across multiple measurements within each tracklet.

8.2.1. Redetection Validation

Analysis of the 70 validated correlations reveals same-night redetection capability. Among the matched satellites, SPOOK made Phase 1 and Phase 2 observations for 20 satellites: 12 LEO cases and 8 MEO cases. Of these observations, ART observed 12 redetections (4 LEO, 8 MEO). Comparing these yields a redetection validation rate of 60.0% (12 of 20 pipeline-predicted redetections confirmed by ART). This rate is comparable to the overall 63.6% pipeline accuracy, which would be expected if redetections do not alter the accuracy of the SPOOK detections. Nevertheless, regime analysis shows that while MEO has a 100% redetection rate, LEO has a much lower rate (33.33%). The lower rate for LEO is likely the increased difficulty in reacquiring fast-moving LEO objects for Phase 2 observations, which have shorter time windows and are not as precise as Phase 1 observations (Phase 1 uses direct SGP4 pointing while Phase 2 relies on admissible regions).

The mean temporal offset between the correlated Phase 1 and Phase 2 observations was 101.1 minutes for LEO, and 21.3 minutes for MEO (MEO's longer visibility windows allow Phase 2 observations within the same pass, while LEO's shorter windows require waiting for subsequent passes), demonstrating a sufficient gap between observations for tracklet correlation. The 60.0% redetection validation rate demonstrates the PAR pipeline's two-phase approach functions as designed when implemented on real hardware. Table 8.1 shows a summary of the validation statistics.

Table 8.1: Summary statistics for pipeline-ART validation

Metric	MEO	LEO	Total	Unit
Dataset				
Pipeline observations	31	79	110	
ART observations	54	88	142	
Validated ART target detections	27	44	71	
Matched correlations	27	43	70	
Pipeline redetections	8	12	20	
ART observed redetections	8	4	12	
Success Rates				
Detection capture rate	100.0	97.73	98.6	%
Pipeline accuracy	87.10	54.4	63.6	%
Redetection validation rate	100.0	33.33	60.0	%
Angular Accuracy				
Min separation	0.03	0.26	0.03	arcsec
Mean separation	49.97	34.60	40.53	arcsec
Median separation	0.41	5.35	5.17	arcsec
Max separation	195.02	199.02	199.02	arcsec
Standard deviation	64.26	58.40	61.18	arcsec

8.3. TDM-to-TDM Comparison

As supplementary validation, TDM-to-TDM (see Appendix B) comparison examines positional accuracy at observation epoch by interpolating (or extrapolating if there is no time overlap) predicted positions to match ART measurement times. For each matched pair, observation epochs are extracted from ART TDM files (typically 5-10 measurements per tracklet), SPOOK predicted positions are interpolated to these exact epochs, and angular separation is computed using spherical trigonometry. Aggregating statistics across all measurement pairs yields 487 total comparison points with mean angular separation 86.2 arcseconds, median 83.7 arcseconds, and a maximum separation of 197.8 arcseconds.

Of the 70 matched correlations, only 16 produced usable TDM-to-TDM comparisons. The reduced sample size results from SPOOK's photometric model limitations. When SPOOK generates TDMs, no light-time corrections are applied. Moreover, SPOOK simulates all objects as perfect 1-metre diameter spheres with albedo 0.1. For satellites with complex geometries, large solar panels, or unusual aspect ratios, this simplified model produces brightness predictions that differ significantly from reality. If the predicted magnitude falls outside ART's detection range or the geometric model produces poor position estimates, the TDM cannot be reliably matched. The 16 successful TDM-to-TDM comparisons provide valuable positional accuracy validation.

To illustrate the range of validation performance, three representative cases are described. NORAD 27663 (MEO, Table B.2) achieves an angular accuracy of 34.3 arcseconds. This precision demonstrates SPOOK's capability for accurate predictions in stable orbital regimes. NORAD 36036 (LEO, Table B.3) shows similar performance with 33.2 arcsecond angular error, consistent with expected TLE accuracy for same-day orbital elements. NORAD 40011 (LEO, Table B.15) shows angular error near the upper validation threshold at 197.8 arcseconds, yet remains within the correlation criterion. Despite representing near-maximum observed error, this case validates SPOOK's prediction accuracy, with larger discrepancy likely reflecting differential TLE quality or atmospheric drag effects.

Physical characteristics extracted from ART and SPOOK TDMs provide additional validation dimensions. SNR varies significantly between targets, with some achieving SNR exceeding 140 while others exhibit SNRs near 7 (see Appendix B). While these values are well within observation limits (≥2), photometric validation shows magnitude prediction irregularities across the observations. Some targets demonstrate photometric consistency within 0.1-0.5 magnitudes, while others exhibit multi-magnitude discrepancies. Satellite brightness depends on geometry, surface materials, attitude dynamics, and solar illumination phase angle. Tumbling satellites, complex spacecraft geometries, and specular reflections from solar panels produce highly variable brightness, none of which are accounted for in the photometric model in SPOOK. NORAD 59588 is a noticeable case that includes solar sails where magnitude prediction errors exceed 5 magnitudes. These photometric limitations do not impact positional validation but indicate areas for future model refinement.

A summary of some of the above mentioned data can be found in Table 8.2. Lastly, in Appendix C, some examples of ART images can be seen.

Table 8.2: Summary statistics for pipeline-ART TDM-to-TDM comparison

Metric	Value	Unit
Temporal Overlap		
Mean	16.88	seconds
Median	3.00	seconds
Standard deviation	52.23	seconds
Range	1.00 – 219.00	seconds
Magnitude Difference		
Mean	1.59	–
Median	1.15	–
Standard deviation	1.19	–
Range	0.13 – 4.22	–

8.4. Summary

The validation establishes the PAR pipeline's observation planning methodology through comparison with ART observations. The detection capture rate indicates that when ART successfully observes a target satellite with accurate TLEs, SPOOK made the same observation in 98.6% of cases. The pipeline accuracy indicates that 63.6% of pipeline observations were confirmed by actual ART observations.

The validation results establish the credibility of the PAR pipeline and SPOOK simulation framework for the strategy analysis presented in Chapter 9. The 63.6% pipeline accuracy and strong positional accuracy (mean 40.53 arcseconds, within SGP4 expected performance) demonstrate that the pipeline produces realistic predictions of telescope observations. The 60.0% redetection validation rate further confirms that the PAR pipeline's two-phase strategy functions as intended when implemented on a real telescope.

9

Results

This chapter presents results from surveillance evaluations conducted using the PAR simulation framework across LEO and MEO satellite populations. SPOOK served as the optical performance model for all simulations. The evaluation addresses the research questions formulated in Chapter 3 through controlled experiments comparing surveillance strategies. The primary analysis focuses on LEO sun-synchronous orbit satellites from Space-Track (1,562 satellites), with comparative MEO validation presented in Section 9.4.

The chapter is structured to address each research question sequentially. Section 9.1 examines the performance of different scanning patterns in detecting LEO satellites (Sub-Question 1). Section 9.2 compares the redetection capabilities of PAR-based and baseline surveillance approaches (Sub-Question 2). Section 9.3 analyses the sensitivity of PAR performance to parameter variations (Sub-Question 3). Finally, Section 9.5 combines these findings to address the main research question regarding optimal surveillance strategies for LEO catalogue generation.

9.1. Scanning Pattern Performance

Three scanning patterns were evaluated to determine their effectiveness in detecting LEO satellites: declination stripe scanning, right ascension stripe scanning, and grid scanning. Each strategy was tested across 22 observation simulations representing different observation dates and times. The temporal variation results in different satellite positions and visibility windows while maintaining constant telescope parameters. The evaluation simulated observations of 1,562 SSO satellites per simulation, with exposure times varied between 0.2 and 3.0 seconds and observation durations of 10 hours.

The telescope operates from 38.2°N, 6.6°W at 570m elevation with a $3.18° \times 2.39°$ field of view and minimum elevation angle of 20°. Observations were restricted to nautical twilight conditions (Sun elevation $\leq -9°$) to ensure satellites remained illuminated while the sky background was sufficiently dark for detection. The declination stripe pattern scans a 20° wide band across fixed declination ranges. The grid pattern samples 2 hours of right ascension by 5° declination cells. The RA stripe orientation spans 4 hours of right ascension. Strategy configurations are detailed in Table 7.1. The centre of the stripes and grid was determined using the GMM approach described in Chapter 7. Using 1,562 TLEs, and propagating them over a 10-hour window, a synthetic population was made. The highest density region was then selected for the centre point of the baseline strategies. Using the night-split mode (dividing observation windows into two independent periods, see Chapter 7), redetections were attempted. Different high-density regions were identified for the 2 different portions of the night. The goal is to get as many objects as possible to pass through the stripe or grid at the beginning of the night and to get those same objects to pass through the FoV again towards the end of the night.

9.1.1. Detection Performance

Table 9.1 presents the detection performance for each scanning pattern. Declination stripe and grid scanning achieved equivalent detection rates of 0.0116%, corresponding to 0.18 satellites detected per

10-hour observation session. RA stripe scanning produced zero detections across all 22 simulations. These detection rates are effectively zero for practical surveillance purposes, with less than one satellite detected per 10-hour observation session on average.

Table 9.1: Scanning Pattern Detection Performance

Strategy	Simulations	Detection Rate (%)	Unique Detections
Grid	22	0.0116 ± 0.0253	0.18 ± 0.39
Declination Stripe	22	0.0116 ± 0.0253	0.18 ± 0.39
RA Stripe	22	0.0000 ± 0.0000	0.00 ± 0.00

The equivalent performance of declination stripe and grid scanning reflects similar effective sky coverage patterns under the simulated conditions. Both approaches achieve similar intersection probabilities with SSO satellite trajectories from the telescope's mid-latitude location. The absence of detections from RA stripe scanning indicates that the 4-hour wide RA stripe orientation misaligns with the predominantly north-south ground track motion of SSO satellites as viewed from 38°N latitude. However, the performance of all three baseline strategies indicates that detections are rare.

9.1.2. Redetection Capability

Baseline scanning methods achieved zero redetections. All eight satellites detected across the 22 simulations were observed exactly once. This demonstrates a limitation of fixed-pattern surveillance: without incorporating prior detection information, redetection within the same observing session is highly unlikely. The detection rate calculation is averaged across all 22 independent simulations, each representing a separate 10-hour observation session. The night-split mode did not mitigate this shortcoming, this indicates that baseline methods cannot effectively enable follow-up observations required for IOD. However, given the practically 0% detection rate across all baseline strategies, it is unlikely to achieve a redetection. Therefore, concluding that effective follow-ups are not possible using baseline strategies comes from the fact that general detection rate are extremely low for LEO objects. Important to note is that many objects in LEO have short and fairly irregular observation windows (w.r.t. the location of the simulated telescope). As a result, simply splitting the night into two 5 hour windows severely limits the possibility for redetection. Indeed, a better way would be to estimate the specific position of each satellite and calculate their observation windows.

9.2. Redetection Rate Comparison

The PAR pipeline operates in two distinct phases designed to enable multi-epoch observations for IOD. Phase 1 uses SGP4 propagation using TLEs to identify when satellites are observable and generates observation schedules targeting these predicted passes. This approach aims to simulate a first observation for which a follow-up will be scheduled. Phase 2 evaluates whether satellites successfully detected in Phase 1 can be redetected during subsequent observation opportunities using PAR-derived pointings from the initial tracklet.

9.2.1. Phase 1: Initial Detection

Phase 1 tested 1,562 unique SSO satellites for initial detection for a total of 3,911 total simulations. These satellites represent the subset of the SSO catalogue selected across multiple evaluation simulations with varying parameter configurations. In total, 2,897 simulations achieved successful Phase 1 detections, representing 74.07% of all simulations. This discrepancy is in part due to TLE/SGP4 errors, but mostly because of observation window overlap, and lack of accessibility to the telescope, meaning not all objects could physically be observed during the observation window.

From the successful Phase 1 detections, 194 simulations had Phase 2 follow-ups. The limited Phase 2 sample size (compared to Phase 1) reflects the fact that many satellites lacked suitable second observation windows due to unfavourable geometric conditions.

9.2.2. Phase 2: Follow-up Redetection

Phase 2 evaluated the capability of the PAR pipeline to redetect satellites during subsequent observation opportunities. Of the 194 simulations in Phase 2, 46 achieved successful redetections, corresponding to a redetection rate of 23.71% (Table 9.2). At the satellite level, 15 of the 31 unique satellites (48.4%) achieved at least one successful redetection across their various observation nights.

Table 9.2: Redetection Rate Comparison

Method	Mean Rate (%)
PAR	23.71
Grid	0.00
Declination Stripe	0.00
RA Stripe	0.00

The redetection rate of 23.71% represents simulations for which predicted admissible regions successfully guided telescope pointings to achieve follow-up observations. This rate is significantly higher than the 0% redetection rate observed for all baseline scanning methods.

The 76.29% of configurations that did not achieve redetection reflect several limiting factors. The time span between the observation windows varies greatly between objects. One object might be accessible again within an hour of initial detection, while the other only at the end of the night ($\approx$ 8 hour difference at times). Furthermore, PAR prediction accuracy depends on the quality of the initial tracklet. Satellites with brief initial observations or unfavourable viewing geometry produce larger admissible regions, decreasing the likelihood that telescope pointings intersect the satellite's actual trajectory. The combination of the separation of observation windows, large admissible regions for some targets, J2 propagation limitations, and unfavourable viewing geometry accounts for the majority of unsuccessful redetections.

9.3. Parameter Sensitivity Analysis

Correlation analysis between parameter values and detection success across the satellites that achieved successful redetection (see Table 9.3) shows observation duration (the time allocated to each Phase 1 surveillance session, ranging from 0.01 to 10 hours) as the primary factor affecting success rate (r = 0.275). Longer observation sessions provide more Phase 1 detection opportunities, outweighing the reduction in time available for Phase 2 follow-up. PAR sample density (r = -0.142) and eccentricity constraints (r = -0.102) exhibit weak negative correlations. However, examination of the parameter distributions (Figure 9.1) reveals these correlations are driven by extreme bins with small sample sizes ($n < 50$) while well-sampled bins ($n > 1000$) show consistent performance around 70–72%. All other parameters show negligible correlation ($|r| < 0.05$). These patterns suggest PAR configuration parameters have minimal systematic impact on redetection success within the parameter ranges tested in this work, with observation duration as the dominant factor. One parameter not observed is the time separation between Phase 1 and Phase 2 observation windows, which depends on both satellite accessibility windows and the pipeline's accuracy in building admissible regions and propagating samples. Although not quantified in this work, this temporal separation may dominate redetection success, suggesting that satellites with narrowly separated observation windows could be better candidates for PAR-based follow-ups.

Table 9.3: PAR Parameter Sensitivity Analysis

Parameter	Correlation	Values Tested	Unit
Duration	0.275	0.01–10.0	[hrs]
PAR Samples	-0.142	3, 5, 10, 20, 50	
Eccentricity Max	-0.102	0.01, 0.05, 0.1, 0.15, 0.2	
Exposure Time	-0.028	0.1, 0.2, 0.5, 1, 2, 3, 5	[s]
Semi-major Axis Max	0.005	8000, 8500, 9000	[km]
Semi-major Axis Min	-0.001	6500, 7000, 7500	[km]

Figure 9.1 presents success rate distributions across parameter ranges for simulation attempts involving satellites that achieved at least one successful redetection. Success rate represents the percentage of attempts achieving redetection within this filtered subset. Bins are colour-coded: green (> 70%), yellow (40–70%), red (< 40%).

Within this subset of redetectable satellites, observation duration shows the clearest pattern, with success rates increasing from 26.1% for sessions under 1 hour to 74.8% for sessions exceeding 10 hours. Eccentricity constraints demonstrate that tighter limits (≤ 0.1) achieve 70–74% success rates compared to 43–48% for looser constraints (> 0.15). All other parameters show flat distributions with success rates near 71–72%, indicating minimal variation within the tested ranges for satellites that are fundamentally redetectable. This success rate distribution reflects the correlation coefficients presented in Table 9.3. However, the low success rates for extreme parameter values (14 PAR samples: 35.3%, n=34; eccentricity > 0.15: 43–48%, n=28–21) should be interpreted cautiously due to small sample sizes compared to larger bins (n=1200–1400). The negative correlations may reflect insufficient sampling of certain configurations rather than systematic effects.

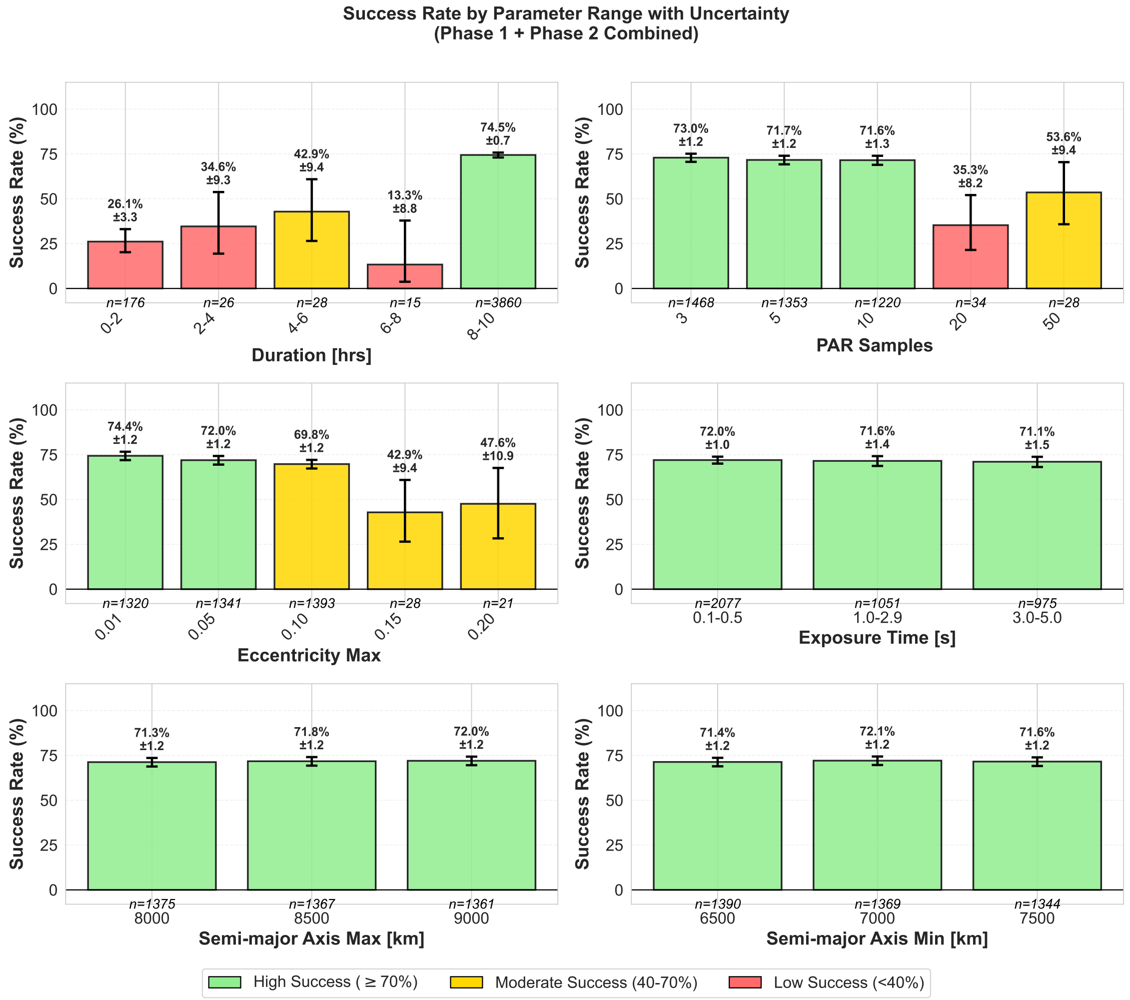

Figure 9.1: LEO success rate distributions for satellites achieving at least one successful redetection (filtered subset). Bins colour-coded: green (> 70%), yellow (40–70%), red (< 40%). Duration and eccentricity show clear patterns. Other parameters exhibit minimal variation.

9.4. MEO Catalogue Comparison

To evaluate the regime-dependence of surveillance approaches, the pipeline was tested on MEO satellites. While LEO surveillance represents the primary research focus, MEO results provide insight into how orbital regime affects detection and redetection performance.

9.4.1. MEO Detection Performance

Unlike LEO surveillance, baseline scanning methods achieve substantial detection rates for MEO targets. Declination stripe scanning achieved 17.95% detection rate, followed by grid scanning (11.17%) and RA stripe scanning (7.86%) across 9 simulations each (Table 9.4). These rates are orders of magnitude higher than the negligible detection rates observed for LEO baselines (0.0116%, Table 9.1).

Table 9.4: MEO Scanning Pattern Detection Performance

Strategy	Simulations	Detection Rate (%)	Unique Detections
Declination Stripe	9	17.95 ± 7.82	2.56 ± 1.13
Grid	9	11.17 ± 5.24	2.11 ± 1.27
RA Stripe	9	7.86 ± 8.46	1.44 ± 1.51

The improved baseline performance reflects differences between orbital regimes. MEO satellites exhibit slower angular motion, resulting in longer observation arcs and increased intersection probability with fixed scanning patterns. The telescope's 3.18° × 2.39° FoV captures MEO satellites for longer durations than for LEO, enabling detection with predetermined pointing strategies.

9.4.2. MEO Redetection Performance

MEO redetection rates demonstrate the regime-dependence of surveillance difficulty (Table 9.5). The PAR pipeline achieved 91.94% redetection rate, while baseline methods achieved 49–62% redetection rates. These rates contrast with LEO performance, where PAR achieved 23.71% and baselines achieved 0%.

Table 9.5: MEO Redetection Rate Comparison

Method	Mean Rate (%)
PAR	91.94
Declination Stripe	62.02
RA Stripe	58.46
Grid	49.08

The high success rates across all methods indicate that MEO redetection is easier than LEO redetection. Longer Phase 1 observation arcs produce more accurate initial orbit estimates, while slower satellite motion results in slower admissible region growth during propagation. The combination enables successful redetections even with baseline scanning patterns, which fail entirely for LEO targets. Moreover, large observation windows allow more redetections to occur over a larger period of the observation night, increasing rates.

PAR's advantage persists (91.94% vs 49–62% for baselines) but is less pronounced than in LEO, where PAR provided the only viable redetection capability. This demonstrates that PAR's value increases with surveillance difficulty.

9.4.3. MEO Parameter Sensitivity

MEO parameter correlations exhibit similar patterns to LEO (Table 9.6). Observation duration shows weak positive correlation ($r = 0.150$), while all other parameters show negligible effects ($|r| < 0.10$). The weaker duration correlation compared to LEO ($r = 0.275$) reflects the overall higher success rates: when most configurations succeed, parameter variations matter less.

Success rate distributions for MEO demonstrate consistently high performance (94–100%) across all parameter ranges, contrasting with LEO's wider variation (26–75%). This high success indicates that MEO surveillance is less sensitive to configuration choices.

9.5. Main Research Question: Strategy Effectiveness

The evaluation results address the main research question: *Which surveillance strategy most effectively contributes to LEO catalogue generation?* For LEO satellites, the PAR pipeline achieved a 23.71% redetection

Table 9.6: MEO Parameter Sensitivity Analysis

Parameter	Correlation	Values Tested
Duration	0.150	0.01–10.0 hrs
Semi-major Axis Min	-0.051	10,000, 12,000, 16,000 km
Eccentricity Max	-0.036	0.01–0.2
Semi-major Axis Max	-0.032	20,000, 25,000, 35,000 km
Exposure Time	-0.030	0.1–5.0 s
PAR Samples	-0.027	10, 20, 50

rate across 194 Phase 2 attempts, while all baseline scanning methods produced zero redetections. MEO comparison results demonstrate that surveillance difficulty is regime-dependent. MEO baselines achieved 49–62% redetection rates while PAR achieved 91.94%, indicating that traditional methods can work for MEO but fail for LEO.

Table 9.7 presents the LEO redetection rate comparison. The absence of redetections in LEO baseline scanning means these strategies contribute minimally to LEO catalogue generation, as follow-up observations necessary for IOD cannot be achieved.

Table 9.7: Redetection Rate Comparison: PAR vs Baseline Methods (LEO)

Method	Mean Redetection Rate (%)
PAR	23.71
Baseline	0.00

When successful, these redetections enable IOD as multiple observations separated by hours sufficiently constrain the unobserved range and range-rate parameters that cannot be determined from single-pass angular observations alone.

10

Conclusion and Future Work

10.1. Conclusion

This research evaluated surveillance strategies for LEO catalogue generation through SPOOK simulations and observational validation against ART telescope data from September 2025. The investigation compared three baseline scanning patterns (declination stripe, right ascension stripe, grid) against a two-phase admissible region pipeline across LEO and MEO orbital regimes. Baseline scanning methods achieved detection rates of 0.0116% for declination stripe and grid patterns. Right ascension stripe scanning produced no detections. These results indicate that these patterns do not effectively observe SSO objects at ART's latitude (see Appendix A). The equivalent performance of declination stripe and grid scanning suggests both patterns provide comparable coverage under the tested conditions. No baseline method achieved redetections within observation periods, all satellites detected were observed exactly once.

The PAR pipeline achieved a 23.71% redetection rate compared to 0% for all baseline methods. Of 194 satellites tested in Phase 2 follow-up observations, 46 were successfully redetected. This redetection capability provides the multiple observation epochs separated in time required for orbit determination beyond the precision achievable from single tracklets. Validation using MEO satellites revealed that surveillance difficulty is strongly regime-dependent. MEO baseline methods achieved 49–62% redetection rates compared to ($\approx$ 0%) for LEO baselines, while PAR achieved 91.94% for MEO versus 23.71% for LEO. The improved performance across all methods for MEO reflects differences in observability. Slower angular motion produces longer observation arcs and slower admissible region growth. This regime comparison demonstrates that PAR provides value across orbital regimes but is most critical where baseline methods fail entirely, specifically, for fast-moving LEO targets.

Parameter sensitivity analysis revealed that PAR performance is largely insensitive to configuration choices within operationally relevant used parameter ranges. Observation duration emerged as the primary factor, with longer sessions enabling more Phase 1 detections despite reducing Phase 2 follow-up time. Exposure time (0.1–5.0 seconds), semi-major axis constraints (6500–9000 km), and PAR sample density (3–50 samples) showed minimal systematic effects on success rates, with well-sampled parameter ranges consistently achieving 70–72% success rates among redetectable satellites. This parameter insensitivity demonstrates PAR robustness across configurations.

Validation against ART observations established pipeline accuracy through correlation of 70 detections of the 110 predictions (63.6% accuracy). Mean angular separation between SPOOK predictions and validated ART measurements was 40.53 arcseconds, consistent with expected SGP4 propagation accuracy for same-day TLE elements. Same-night redetection validation demonstrated 60.0% operational success rate, confirming PAR pipeline performance for Phase 1 detection and Phase 2 follow-up scenarios. The validation confirmed SPOOK's reliability as an optical performance model and the pipeline's working.

The results establish that surveillance strategy effectiveness depends on orbital regime. For LEO surveillance, where rapid motion and brief observation windows challenge fixed-pattern methods, PAR-based approaches provide considerably more redetections necessary for orbit determination. For MEO surveillance, both fixed-pattern and PAR approaches achieve high success rates, though PAR maintains superior performance. The computational requirements of AR calculation, propagation, and scheduling represent justified costs when redetection capability is critical.

10.2. Future Work

The results presented in this thesis establish the performance advantages of PAR-based surveillance over traditional scanning methods for LEO catalogue generation. However, several limitations in the experimental scope and methodology present opportunities for extension and refinement.

The evaluation campaign comprised 22 simulations per strategy, with validation data limited to September 2025 observations. This constraint restricts analysis to a single seasonal configuration and does not capture variations in satellite population distribution, atmospheric conditions, geometric observability, or night lengths at different times of year. Extension of the evaluation period to span multiple seasons would enable assessment of seasonal effects on detection performance and validation of strategy robustness under varying environmental conditions.

Future work should prioritise quantifying observation window separation between Phase 1 and Phase 2 (or equivalent). This factor may dominate redetection success beyond the configuration parameters evaluated in this work.

This work evaluated single-sensor performance. Extension to multi-sensor configurations would enable investigation of distributed networks at different locations, different sensor capabilities, and coordinated surveillance strategies to constrain ARs more rapidly than single-sensor approaches. This could potentially result in faster follow-ups, leading to a smaller AR.

The evaluation focused on sun-synchronous orbits with near-circular trajectories. Several orbital populations remain unexamined, including highly eccentric orbits, satellites transitioning between LEO and higher orbits, and the full inclination space from equatorial through polar orbits. Testing across this broader orbital parameter space would establish strategy performance beyond the near-polar inclination bias of the SSO population.

The current PAR implementation samples uniformly in range and range-rate space when tasking the telescope (when points are propagated continuously, checked for accessibility and scanned, after the initial time for Phase 2). This approach treats all points within the AR boundary as equally probable. Implementing sampling from a fitted probability density function (through implementation of a GMM fit) prior to propagation would concentrate samples in high-likelihood regions and potentially improve detection efficiency.

Several simplifications in the observation model present opportunities for increased fidelity. SPOOK models all satellites as 1-metre diameter perfect spheres. Incorporating shape models would improve brightness predictions and therefore detection predictions and validation. The PAR propagation model incorporates J2 perturbations but neglects atmospheric drag. Incorporating drag would require defining atmospheric density models and introducing ballistic coefficient as an additional constraint in the AR formulation, extending the constraint space to higher dimensions.

The parameter sensitivity analysis examined six variables within limited ranges. Several parameters merit expanded investigation, including extended eccentricity ranges to encompass highly eccentric orbits (when simulated), introduction of inclination constraints (if implemented in the AR) across the full orbital inclination spectrum, and extension of sampling density ranges to determine saturation behaviour.

Three baseline scanning patterns were evaluated. Additional strategies merit investigation, including adaptive grid spacing based on predicted satellite density, spiral scanning patterns for continuous coverage, and stare-and-chase strategies for maximum SNR are some examples. The current evaluation compares one prior knowledge based method vs 3 coverage based methods without examining other prior knowledge strategies. Including other strategies that are built for follow-up might show more insightful results.

The validation campaign compared SPOOK predictions against ART observations for known satellites.

Operational catalogue generation requires detecting and tracking initially unknown objects. Field testing should include detection campaigns without prior knowledge followed by PAR-based follow-up, same-night reacquisition attempts to determine maximum time gaps for successful PAR application, and assessment of whether PAR-guided observations provide sufficient information for accurate orbit determination.

This work relied exclusively on TLE sets with SGP4 propagation for orbital modelling. Incorporating alternative orbital representations could improve both simulation fidelity and validation accuracy. Extending the observation campaigns by simulating more nights as well as additional validation nights would strengthen the statistical significance of these findings.

A

ART Specifications

Table A.1: Airbus Robotic Telescope (ART) specifications.

Location	Extremadura, Spain	
(Lat., Long., Alt.)	(38.21607°, -6.62778°, 570 m)	
Tracking types	Surveillance, tracking	
Tasking methods	Scheduler	
Data format	FITS, CCSDS TDM	
Accuracy (1-σ)	< 0.5 arcsec MEO, < 5 arcesc LEO.	
Parameter	**ASA H8**	**ASA H400**
Aperture diameter [mm]	200	400
Focal length [mm] (f-ratio)	590 (2.95)	960 (2.4)
Camera	FLI ML11002	Moravian G5-150M
Detector type	CCD, Interline	CMOS, Back-illuminated
Shutter	Global	Rolling
Detector size [px]	4008×2672	14208×10656
Pixel size [μm]	9.00	3.76
Pixel scale [″/px]	3.15	0.80
Field of view [deg]	3.50×2.34	3.18×2.39
Filters	Clear, UBVRI and empty	Empty and BVRI
Sensor peak QE [%]	50	≈ 90
Typical readout time full frame	<10 s	< 1.5 s

Figure A.1: ART's two-telescope configuration on June 2023.

B

ART - SPOOK TDM Correlation

Table B.1: SPOOK-ART validation for LEO satellite NORAD 4327

Temporal Correlation

Time Window	SPOOK TDM	ART TDM	Δt
Pass 1	02:28:59 - 02:29:12	02:29:00 - 02:29:09	0.0 sec

Photometric Correlation

Source	Mag Range	Mean Mag	Difference
SPOOK	9.14 - 9.27	9.21	0.15
ART	8.88 - 9.21	9.06	

Angular Position Correlation

	Source	RA (deg)	Dec (deg)	Angular Separation
Pass 1	SPOOK	125.94	57.96	<85 arcsec
	ART	125.89	57.96	

Physical Characteristics (SPOOK Observations)

Parameter	Value Range	Consistency
Signal-to-Noise	34.52 - 36.38	Excellent detection quality

Table B.2: SPOOK-ART validation for MEO satellite NORAD 27663

Temporal Correlation

Time Window	SPOOK TDM	ART TDM	Δt
Pass 1	02:28:52 - 02:32:32	02:28:53 - 02:32:34	0.0 sec

Photometric Correlation

Source	Mag Range	Mean Mag	Difference
SPOOK	11.46 - 11.47	11.47	0.90
ART	12.23 - 12.56	12.37	

Angular Position Correlation

	Source	RA (deg)	Dec (deg)	Angular Separation
Pass 1	SPOOK	27.17	21.13	<34 arcsec
	ART	27.17	21.14	

Physical Characteristics (SPOOK Observations)

Parameter	Value Range	Consistency
Signal-to-Noise	45.31 - 45.48	Excellent detection quality

Table B.3: SPOOK-ART validation for LEO satellite NORAD 36036

Temporal Correlation

Time Window	SPOOK TDM	ART TDM	Δt
Pass 1	19:23:59 - 19:24:06	19:24:00 - 19:24:05	0.0 sec

Photometric Correlation

Source	Mag Range	Mean Mag	Difference
SPOOK	7.26 - 7.29	7.28	0.77
ART	6.39 - 6.58	6.51	

Angular Position Correlation

	Source	RA (deg)	Dec (deg)	Angular Separation
Pass 1	SPOOK	140.85	70.12	<33 arcsec
	ART	140.88	70.12	

Physical Characteristics (SPOOK Observations)

Parameter	Value Range	Consistency
Signal-to-Noise	74.49 - 74.82	Excellent detection quality

Table B.4: SPOOK-ART validation for LEO satellite NORAD 36122

Temporal Correlation

Time Window	**SPOOK TDM**	**ART TDM**	Δt
Pass 1	04:25:05 - 04:25:20	04:25:15 - 04:25:21	0.0 sec

Photometric Correlation

Source	**Mag Range**	**Mean Mag**	**Difference**
SPOOK	11.20 - 11.32	11.26	1.19
ART	9.43 - 10.56	10.07	

Angular Position Correlation

	Source	**RA (deg)**	**Dec (deg)**	**Angular Separation**
Pass 1	SPOOK	286.95	68.79	<22 arcsec
	ART	286.96	68.78	

Physical Characteristics (SPOOK Observations)

Parameter	**Value Range**	**Consistency**
Signal-to-Noise	12.99 - 13.60	Good detection quality

Table B.5: SPOOK-ART validation for LEO satellite NORAD 37214 (Passes 1-2)

Temporal Correlation

Time Window	**SPOOK TDM**	**ART TDM**	Δt
Pass 1	19:18:00 - 19:18:03	19:18:00 - 19:18:04	0.0 sec
Pass 2	20:58:16 - 20:58:19	20:58:14 - 20:58:20	0.0 sec

Photometric Correlation

	Source	**Mag Range**	**Mean Mag**	**Difference**
Pass 1	SPOOK	5.61 - 5.62	5.62	1.11
	ART	4.38 - 4.65	4.51	
Pass 2	SPOOK	6.89 - 6.89	6.89	0.13
	ART	6.09 - 7.24	6.76	

Angular Position Correlation

	Source	**RA (deg)**	**Dec (deg)**	**Angular Separation**
Pass 1	SPOOK	350.07	6.48	<157 arcsec
	ART	350.09	6.52	
Pass 2	SPOOK	271.03	-13.66	<31 arcsec
	ART	271.03	-13.67	

Physical Characteristics (SPOOK Observations)

	Parameter	**Value Range**	**Consistency**
Pass 1	Signal-to-Noise	141.57 - 142.13	Excellent detection quality
Pass 2	Signal-to-Noise	79.50 - 79.57	Excellent detection quality

Table B.6: SPOOK-ART validation for LEO satellite NORAD 37214

Temporal Correlation

Time Window	SPOOK TDM	ART TDM	Δt
Pass 1	20:04:29 - 20:04:31	20:04:30 - 20:04:32	0.0 sec

Photometric Correlation

Source	Mag Range	Mean Mag	Difference
SPOOK	4.89 - 4.91	4.90	1.59
ART	3.28 - 3.33	3.30	

Angular Position Correlation

	Source	RA (deg)	Dec (deg)	Angular Separation
Pass 1	SPOOK	316.43	53.07	<84 arcsec
	ART	316.43	53.04	

Physical Characteristics (SPOOK Observations)

Parameter	Value Range	Consistency
Signal-to-Noise	138.38 - 139.28	Excellent detection quality

Table B.7: SPOOK-ART validation for LEO satellite NORAD 37730

Temporal Correlation

Time Window	SPOOK TDM	ART TDM	Δt
Pass 1	03:38:00 - 03:38:03	03:38:00 - 03:38:06	0.0 sec

Photometric Correlation

Source	Mag Range	Mean Mag	Difference
SPOOK	9.87 - 9.91	9.89	2.51
ART	7.28 - 7.46	7.38	

Angular Position Correlation

	Source	RA (deg)	Dec (deg)	Angular Separation
Pass 1	SPOOK	133.80	31.90	<143 arcsec
	ART	133.83	31.93	

Physical Characteristics (SPOOK Observations)

Parameter	Value Range	Consistency
Signal-to-Noise	17.23 - 17.45	Good detection quality

Table B.8: SPOOK-ART validation for LEO satellite NORAD 29268

Temporal Correlation

Time Window	**SPOOK TDM**	**ART TDM**	Δt
Pass 1	19:07:30 - 19:07:35	19:07:30 - 19:07:33	0.0 sec

Photometric Correlation

Source	**Mag Range**	**Mean Mag**	**Difference**
SPOOK	5.45 - 5.52	5.48	1.11
ART	6.57 - 6.63	6.60	

Angular Position Correlation

	Source	**RA (deg)**	**Dec (deg)**	**Angular Separation**
Pass 1	SPOOK	353.18	70.01	<88 arcsec
	ART	353.17	69.99	

Physical Characteristics (SPOOK Observations)

Parameter	**Value Range**	**Consistency**
Signal-to-Noise	120.33 - 122.80	Excellent detection quality

Table B.9: SPOOK-ART validation for LEO satellite NORAD 39030

Temporal Correlation

Time Window	**SPOOK TDM**	**ART TDM**	Δt
Pass 1	19:27:00 - 19:27:03	19:27:00 - 19:27:04	0.0 sec

Photometric Correlation

Source	**Mag Range**	**Mean Mag**	**Difference**
SPOOK	6.52 - 6.54	6.53	2.72
ART	3.60 - 3.97	3.81	

Angular Position Correlation

	Source	**RA (deg)**	**Dec (deg)**	**Angular Separation**
Pass 1	SPOOK	6.19	27.16	<56 arcsec
	ART	6.18	27.15	

Physical Characteristics (SPOOK Observations)

Parameter	**Value Range**	**Consistency**
Signal-to-Noise	74.71 - 75.22	Excellent detection quality

Table B.10: SPOOK-ART validation for LEO satellite NORAD 43440

Temporal Correlation

Time Window	SPOOK TDM	ART TDM	Δt
Pass 1	19:32:59 - 19:33:01	19:33:00 - 19:33:02	0.0 sec

Photometric Correlation

Source	Mag Range	Mean Mag	Difference
SPOOK	7.82 - 7.85	7.83	0.55
ART	8.38 - 8.40	8.39	

Angular Position Correlation

	Source	RA (deg)	Dec (deg)	Angular Separation
Pass 1	SPOOK	301.18	-13.90	<161 arcsec
	ART	301.18	-13.94	

Physical Characteristics (SPOOK Observations)

Parameter	Value Range	Consistency
Signal-to-Noise	39.62 - 39.91	Excellent detection quality

Table B.11: SPOOK-ART validation for LEO satellite NORAD 43797

Temporal Correlation

Time Window	SPOOK TDM	ART TDM	Δt
Pass 1	19:43:29 - 19:43:31	19:43:30 - 19:43:33	0.0 sec

Photometric Correlation

Source	Mag Range	Mean Mag	Difference
SPOOK	7.78 - 7.80	7.79	0.72
ART	8.50 - 8.53	8.51	

Angular Position Correlation

	Source	RA (deg)	Dec (deg)	Angular Separation
Pass 1	SPOOK	298.82	-16.71	<90 arcsec
	ART	298.85	-16.71	

Physical Characteristics (SPOOK Observations)

Parameter	Value Range	Consistency
Signal-to-Noise	40.42 - 40.72	Excellent detection quality

Table B.12: SPOOK-ART validation for LEO satellite NORAD 43642

Temporal Correlation

Time Window	SPOOK TDM	ART TDM	Δt
Pass 1	19:46:37 - 19:48:01	19:46:30 - 19:46:44	0.0 sec

Photometric Correlation

Source	Mag Range	Mean Mag	Difference
SPOOK	8.25 - 8.65	8.50	4.22
ART	4.16 - 4.48	4.29	

Angular Position Correlation

	Source	RA (deg)	Dec (deg)	Angular Separation
Pass 1	SPOOK	291.55	-13.59	<64 arcsec
	ART	291.53	-13.59	

Physical Characteristics (SPOOK Observations)

Parameter	Value Range	Consistency
Signal-to-Noise	26.65 - 30.20	Good detection quality

Table B.13: SPOOK-ART validation for LEO satellite NORAD 28649

Temporal Correlation

Time Window	SPOOK TDM	ART TDM	Δt
Pass 1	19:50:59 - 19:51:03	19:51:00 - 19:51:04	0.0 sec

Photometric Correlation

Source	Mag Range	Mean Mag	Difference
SPOOK	5.80 - 5.84	5.82	1.23
ART	4.56 - 4.63	4.59	

Angular Position Correlation

	Source	RA (deg)	Dec (deg)	Angular Separation
Pass 1	SPOOK	287.99	-21.25	<53 arcsec
	ART	287.98	-21.24	

Physical Characteristics (SPOOK Observations)

Parameter	Value Range	Consistency
Signal-to-Noise	119.17 - 120.09	Excellent detection quality

Table B.14: SPOOK-ART validation for LEO satellite NORAD 33434

Temporal Correlation

Time Window	SPOOK TDM	ART TDM	Δt
Pass 1	19:52:30 - 19:52:33	19:52:30 - 19:52:35	0.0 sec

Photometric Correlation

Source	Mag Range	Mean Mag	Difference
SPOOK	11.52 - 11.54	11.53	3.69
ART	7.69 - 7.95	7.84	

Angular Position Correlation

	Source	RA (deg)	Dec (deg)	Angular Separation
Pass 1	SPOOK	242.37	15.26	<79 arcsec
	ART	242.37	15.23	

Physical Characteristics (SPOOK Observations)

Parameter	Value Range	Consistency
Signal-to-Noise	7.29 - 7.38	Fair detection quality

Table B.15: SPOOK-ART validation for LEO satellite NORAD 40011

Temporal Correlation

Time Window	SPOOK TDM	ART TDM	Δt
Pass 1	19:56:59 - 19:57:01	19:57:00 - 19:57:02	0.0 sec

Photometric Correlation

Source	Mag Range	Mean Mag	Difference
SPOOK	11.10 - 11.10	11.10	2.79
ART	8.20 - 8.42	8.31	

Angular Position Correlation

	Source	RA (deg)	Dec (deg)	Angular Separation
Pass 1	SPOOK	234.30	17.03	<198 arcsec
	ART	234.32	16.98	

Physical Characteristics (SPOOK Observations)

Parameter	Value Range	Consistency
Signal-to-Noise	8.46 - 8.46	Fair detection quality

C

ART Images

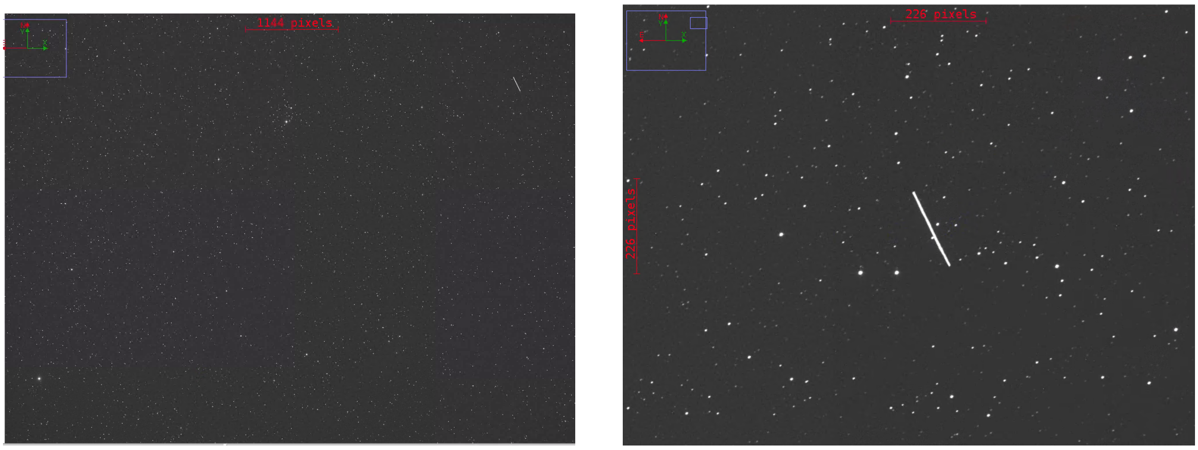

(a) Initial detection

(b) Initial detection (zoomed)

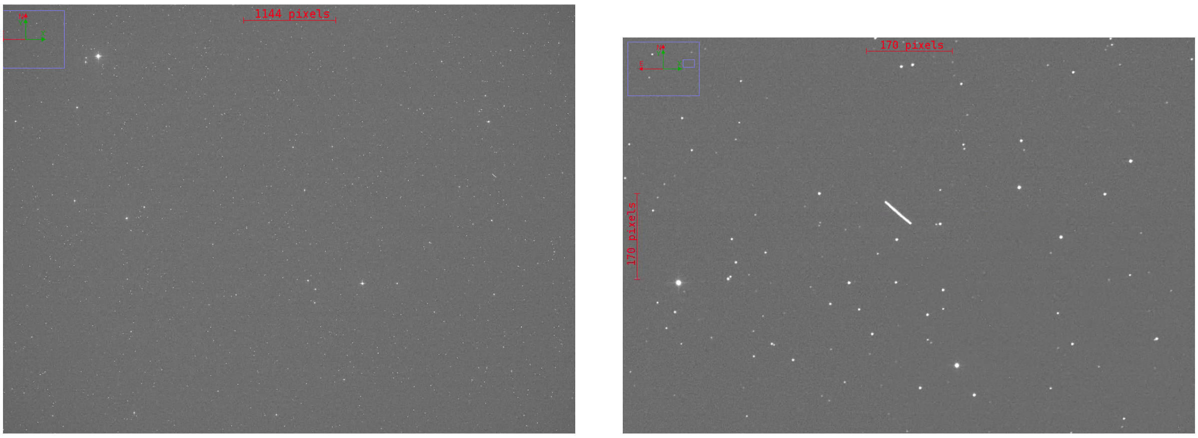

(c) Follow-up observation

(d) Follow-up observation (zoomed)

Figure C.1: ART observations from 16 September MEO validation night showing initial detection and follow-up pass with zoomed views

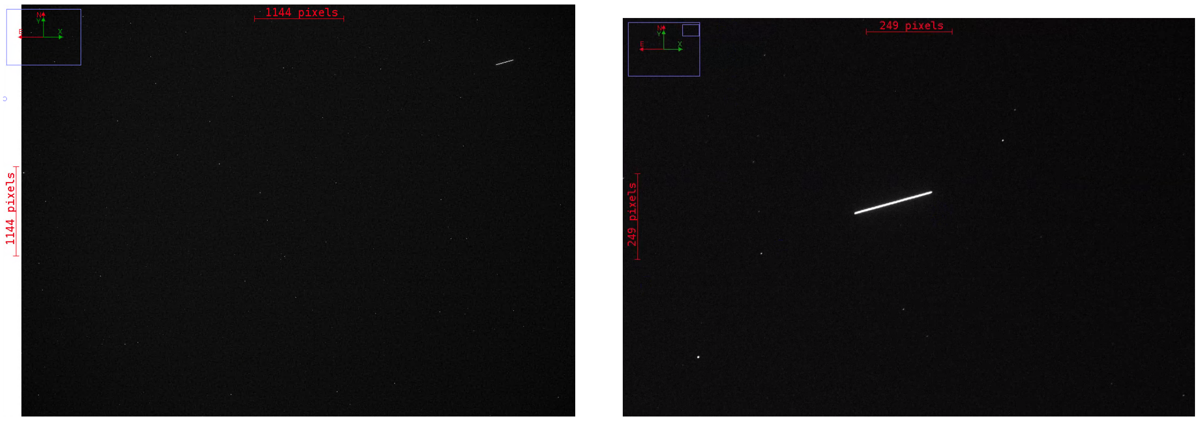

(a) ART observation from 29 September (full image)

(b) ART observation from 29 September

Figure C.2: ART observations from 29 September LEO validation night (zoomed)

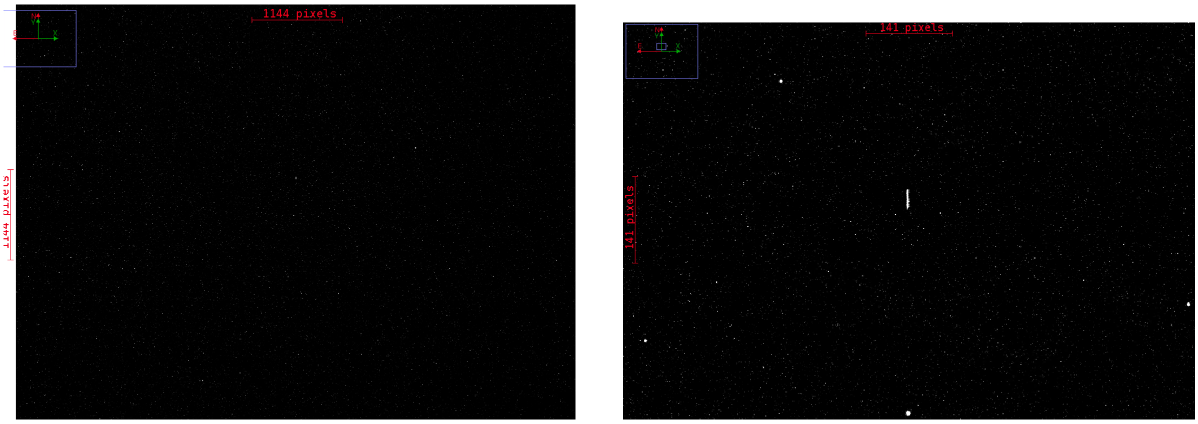

(a) ART observation from 5 September

(b) ART observation from 5 September (zoomed)

Figure C.3: ART observations from 5 September LEO validation night

Bibliography

[1] David S Berry, Tomas J Martin-Mur, and Neil A Mottinger. "CCSDS Tracking Data Message Early Implementation Experiences". In: *Ground Systems Architecture Workshop*. 2009.

[2] Oscar Contreras Carrasco. "Gaussian Mixture Model Explained". In: (Sept. 2024). Accessed: 2025-07-08.

[3] Emilian-Ionuţ Croitoru and Gheorghe Oancea. "Satellite tracking using norad two-line element set format". In: *Scientific Research and Education in the Air Force-AFASES* 1 (2016), pp. 423–431.

[4] Howard D Curtis. *Orbital mechanics for engineering students*. Butterworth-Heinemann, 2019.

[5] Kyle J DeMars, Moriba K Jah, and Paul W Schumacher. "Initial orbit determination using short-arc angle and angle rate data". In: *IEEE Transactions on Aerospace and Electronic Systems* 48.3 (2012), pp. 2628–2637.

[6] Kyle J. DeMars and Moriba K. Jah. "Probabilistic Initial Orbit Determination Using Gaussian Mixture Models". In: *Journal of Guidance, Control, and Dynamics* 36.5 (2013). _eprint: https://doi.org/10.2514/1.59844, pp. 1324–1335. DOI: `10.2514/1.59844`. URL: `https://doi.org/10.2514/1.59844`.

[7] Joachim Ender et al. "Radar techniques for space situational awareness". en. In: ().

[8] T. Flohrer, H. Krag, and H. Klinkrad. "Improving ESA's Collision Risk Estimates by an Assessment of the TLE Orbit Errors of the US SSN Catalogue". In: *Proceedings of the 5th European Conference on Space Debris*. ESA Communications, 2008.

[9] Tim Flohrer. *Optical survey strategies and their application to space surveillance*. de. Geodätisch-geophysikalische Arbeiten in der Schweiz Siebenundachtzigster Band. Zürich: Schweizerische Geodätische Kommission, 2012. ISBN: 978-3-908440-34-5.

[10] Tim Flohrer, Thomas Schildknecht, and Reto Musci. "Proposed strategies for optical observations in a future European Space Surveillance network". In: *Advances in Space Research* 41.7 (2008), pp. 1010–1021.

[11] Carolin Frueh. *Sensor tasking for multi-sensor space object surveillance*. 2017, pp. 18–21.

[12] Carolin Frueh, Hauke Fiedler, and Johannes Herzog. "Heuristic and optimized sensor tasking observation strategies with exemplification for geosynchronous objects". In: *Journal of Guidance, Control, and Dynamics* 41.5 (2018), pp. 1036–1048.

[13] Kohei Fujimoto and Daniel J Scheeres. "Applications of the admissible region to space-based observations". In: *Advances in Space Research* 52.4 (2013), pp. 696–704.

[14] Kohei Fujimoto et al. "ASSOCIATION OF SHORT-ARC OPTICAL TRACKS VIA THE DIRECT BAYESIAN ADMISSIBLE REGION: THEORY AND APPLICATION". en. In: ().

[15] Johannes Herzog. "Cataloguing of objects on high and intermediate altitude orbits". PhD thesis. Universität Bern, 2013.

[16] Johannes Herzog, Thomas Schildknecht, and Carolin Früh. "Build-up and maintanance of a catalogue of GEO obejcts with ZimSMART". In: (2010).

[17] Tyler A Hobson et al. "Catalogue Creation for Space Situational Awareness with Optical Sensors". en. In: (2016).

[18] Marcus J. Holzinger et al. "Uncorrelated-Track Classification, Characterization, and Prioritization Using Admissible Regions and Bayesian Inference". en. In: *Journal of Guidance, Control, and Dynamics* 39.11 (Nov. 2016), pp. 2469–2484. ISSN: 0731-5090, 1533-3884. DOI: `10.2514/1.G001014`. URL: `https://arc.aiaa.org/doi/10.2514/1.G001014` (visited on 05/05/2025).

[19] Steve B Howell. *Handbook of CCD astronomy*. Vol. 2. Cambridge University Press, 2000.

[20] Islam I Hussein et al. "Probabilistic Admissible Region for Short-Arc Angles-Only Observations". en. In: ().

[21] Islam I. Hussein et al. "Probabilistic Admissible Region for Multihypothesis Filter Initialization". en. In: *Journal of Guidance, Control, and Dynamics* 41.3 (Mar. 2018), pp. 710–724. ISSN: 0731-5090, 1533-3884. DOI: `10.2514/1.G002788`. URL: `https://arc.aiaa.org/doi/10.2514/1.G002788` (visited on 05/12/2025).

[22] John A Kennewell and Ba-Ngu Vo. "An Overview of Space Situational Awareness". In: *Proceedings of the 16th Internaitonal Confer-*

ence on Information Fusion. Istanbul, Turkey: IEEE, July 2013. ISBN: 978-605-86311-1-3.

[23] Tom Kelecy, Michael Shoemaker, and Moriba Jah. "Application of the constrained admissible region multiple hypothesis filter to initial orbit determination of a break-up". In: *6th European Conference on Space Debris*. Vol. 723. 2013, p. 65.

[24] T. S. Kelso. "Validation of SGP4 and IS-GPS-200D Against GPS Precision Ephemerides". In: *Proceedings of the 17th AAS/AIAA Space Flight Mechanics Conference*. American Astronautical Society. Sedona, Arizona, 2007.

[25] Jiasheng Li, Zhen Yang, and Yazhong Luo. "Too-Short-Arc Association and Clustering Method for Space-Based Optical Observations". In: *Journal of Guidance, Control, and Dynamics* 48.1 (2025), pp. 84–97. DOI: `10.2514/1.G008069`. eprint: `https://doi.org/10.2514/1.G008069`. URL: `https://doi.org/10.2514/1.G008069`.

[26] JC Liou et al. "Stability of the future LEO environment–an IADC comparison study". In: *Proceedings of the 6th European Conference on Space Debris*. Vol. 723. ESA. 2013.

[27] Bryan D Little and Carolin Frueh. "SSA sensor tasking: comparison of machine learning with classical optimization methods". In: *Proceedings of the Advanced Maui Optical and Space Surveillance Technologies Conference*. 2018, pp. 1–17.

[28] Samuel Manresa Ortiz. "Feasibility study of space debris detection by small optical telescopes". B.S. thesis. Universitat Politècnica de Catalunya, 2022.

[29] Jared M Maruskin, Daniel J Scheeres, and Kyle T Alfriend. "Correlation of optical observations of objects in earth orbit". In: *Journal of Guidance, Control, and Dynamics* 32.1 (2009), pp. 194–209.

[30] Andrea Milani et al. "Orbit determination with very short arcs. I admissible regions". en. In: *Celestial Mechanics and Dynamical Astronomy* 90.1-2 (Sept. 2004), pp. 57–85. ISSN: 0923-2958, 1572-9478. DOI: `10.1007/s10569-004-6593-5`. URL: `http://link.springer.com/10.1007/s10569-004-6593-5` (visited on 05/12/2025).

[31] Utkarsh Mishra et al. "Geometric Solution to Probabilistic Admissible Region (PAR)". In: *The Journal of the Astronautical Sciences* 71.2 (2024), p. 18.

[32] Oliver Montenbruck and Eberhard Gill. *Satellite Orbits: Models, Methods, and Applications*. Berlin Heidelberg: Springer-Verlag, 2000.

[33] Daniel Mulligan and Michelle Stephens. "Bullseye: a leakproof search strategy for space domain awareness". en. In: (2022).

[34] Timothy S Murphy and Marcus J Holzinger. "Generalized minimum-time follow-up approaches applied to tasking electro-optical sensor tasking". In: *Advanced Maui Optical and Space Surveillance (AMOS) Technologies Conference*. 2017, p. 54.

[35] ESA Space Debris Office. *ESA's Annual Space Environment Report*. LOG GEN-DB-LOG-00288-OPS-SD. Version 9.0. Document Type: LOG, Status: Final. European Space Agency (ESA), Mar. 2025. URL: `URL%20to%20the%20document%20if%20available`.

[36] Guido Pedone, Jens Utzmann, and Roger Forstner. "Survey on New Strategies and State of the Art for Space Debris Catalogue Generation for Optical Sensor Networks". en. In: (2021).

[37] Guido Pedone et al. "SPOOK: A tool for space objects catalogue creation and maintenance supporting space safety and sustainability". In: *Acta Astronautica* 188 (2021), pp. 89–98.

[38] C Roscoe et al. "The probabilistic admissible region with additional constraints". In: *Advanced Maui Optical and Space Surveillance Technologies Conference*. 2015, p. 91.

[39] Thomas Schildknecht. "Optical surveys for space debris". In: *The Astronomy and Astrophysics Review* 14.1 (Jan. 2007), pp. 41–111. ISSN: 1432-0754. DOI: `10.1007/s00159-006-0003-9`. URL: `https://doi.org/10.1007/s00159-006-0003-9`.

[40] *scikit-learn: machine learning in Python &x2014; scikit-learn 1.7.2 documentation — scikit-learn.org*. `https://scikit-learn.org/stable/`. [Accessed 28-10-2025].

[41] Secure World Foundation. *Space Situational Awareness*. Fact Sheet FS24/1. Contact: Ian Christensen, ichristensen@swfound.org. Broomfield, CO, USA: Secure World Foundation, July 2024. URL: `https://ppl-ai-file-upload.s3.amazonaws.com/web/direct-files/attachments/54402885/31c2e57b-583b-41ca-9927-e91a3a727da8/fs24-01_space-situational-awareness.pdf`.

[42] Srinivas Janardhana Setty. "Orbit and Uncertainty Propagation for Space Object Catalogue Maintenance". en. In: ().

[43] Jan Siminski, Hauke Fiedler, and Thomas Schildknecht. "Track association performance of the best hypotheses search method". In: (2013).

[44] Jan A Siminski et al. "Best hypotheses search on iso-energy-grid for initial orbit determina-

tion and track association". In: *Advances in the Astronautical Sciences* 148 (2013), pp. 605–617.

[45] *Space Situational or Domain Awareness? Know the Difference! — marcusholzinger.com*. `https://www.marcusholzinger.com/space-situational-or-domain-awareness-know-the-difference/`. [Accessed 27-10-2025].

[46] Marvin Suhr. *Segmentierung von Bildern in Vorder- und Hintergrund mithilfe von Gaussian Mixture Models*. Fachseminar "Machine Learning". Wintersemester 15/16. Hochschule RheinMain, 2016.

[47] Byron D. Tapley, Bob E. Schutz, and George H. Born. "Statistical Orbit Determination Theory". In: *Advances in Astronautical Sciences* 115 (2004), pp. 365–392.

[48] Giacomo Tommei, Andrea Milani, and Alessandro Rossi. "Orbit determination of space debris: admissible regions". In: *Celestial Mechanics and Dynamical Astronomy* 97 (2007), pp. 289–304.

[49] University of Sheffield. *PHY241 Observation Astronomy*. URL: `https://slittlefair.staff.shef.ac.uk/teaching/phy241/lectures/l01/`.

[50] David Vallado and Paul Crawford. "SGP4 orbit determination". In: *AIAA/AAS Astrodynamics specialist conference and exhibit*. 2008, p. 6770.

[51] David A Vallado and Paul J Cefola. "Two-line element sets–practice and use". In: *63rd International Astronautical Congress, Naples, Italy*. 2012, pp. 1–14.

[52] David A. Vallado. *Fundamentals of Astrodynamics and Applications*. 4th ed. Hawthorne, CA: Microcosm Press, 2013.

[53] George Veis. "Optical tracking of artificial satellites". In: *Space science reviews* 2.2 (1963), pp. 250–296.

[54] Brian Weeden and Victoria Samson. *Global counterspace capabilities: An open source assessment*. Secure World Foundation Washington, DC, 2018.

[55] Johnny L Worthy III and Marcus J Holzinger. "Dempster-Shafer theory applied to admissible regions". In: (2017).

[56] Chenbao Xue et al. "Review of sensor tasking methods in Space Situational Awareness". en. In: *Progress in Aerospace Sciences* 147 (May 2024), p. 101017. ISSN: 03760421. DOI: `10.1016/j.paerosci.2024.101017`. URL: `https://linkinghub.elsevier.com/retrieve/pii/S0376042124000435` (visited on 01/23/2025).

[57] Norbert Zehentner. "Kinematic orbit positioning applying the raw observation approach to observe time variable gravity". PhD thesis. Jan. 2017. DOI: `10.13140/RG.2.2.33916.33927`.